

Setup and application of a combined Brillouin-Raman system

Dissertation
zur Erlangung des akademischen Grades
Doctor rerum naturalium
(Dr. rer. nat.)

vorgelegt
dem Bereich Mathematik und Naturwissenschaften
der Technischen Universität Dresden

von
Jan Rix
geboren am 25.12.1994 in Lüneburg

Eingereicht am 08. September 2022
Verteidigt am 19. Dezember 2022

Die Dissertation wurde in der Zeit von Oktober 2019 bis September 2022 im
Institut für Angewandte Physik (IAP) der Technischen Universität Dresden
angefertigt.

1. Gutachter: Prof. Dr. rer. nat. Edmund Koch
2. Gutachter: Prof. Dr. rer. nat. Martin Hofmann

Diese Dissertation wurde unter wissenschaftlicher Betreuung von Herrn Prof. Dr. Edmund Koch, Leiter der Arbeitsgruppe Klinisches Sensoring und Monitoring an der Klinik und Poliklinik für Anästhesiologie und Intensivtherapie der Medizinischen Fakultät Carl Gustav Carus an der Technischen Universität Dresden, angefertigt.

“Ich meine: neben vernünftiger Politik ist Lernen in unserer Welt die eigentlich glaubhafte Alternative zur Gewalt.”

Willy Brandt anlässlich der Verleihung des Friedensnobelpreises 1971

“As I see it, next to reasonable politics, learning is in our world the true credible alternative to force.”

Willy Brandt on the occasion of the award of the Nobel Peace Prize 1971

Abstract

Vibrational spectroscopy is an established technique in materials science as well as in biomedical research for the investigation of sample-specific properties. It exploits the interaction of light (photons) with vibrational quanta (phonons) to obtain material-characteristic information. Raman spectroscopy is sensitive to optical phonons and has been used extensively since the invention of lasers. In contrast, Brillouin spectroscopy investigates acoustic phonons. However, for a long time it was only used sporadically in materials science as it was very time-consuming due to the sequential spectrum acquisition. Only recently, the use of a *virtually imaged phased array* (VIPA) as dispersive element in the Brillouin spectrometer has drastically reduced the measurement time, thus facilitating its application in biomedical research.

In this dissertation, a combined Brillouin-Raman system was built, which allows simultaneous and co-localized acquisition of Brillouin and Raman spectra. Compared to other systems, this setup benefits from the use of two VIPAs with different free spectral ranges, which leads to a decoupling of the spectral axes and thus to more sensitive measurements. It further allows for an unambiguous determination of Brillouin shifts. Moreover, the near-infrared excitation at 780 nm and the continuous calibration of the Brillouin spectrum characterize this system.

In a first application, ferroelectric domain walls in periodically poled lithium niobate were studied with this combined system. It was found that, in addition to the Raman contrast known from literature (intensity variation at 635 cm^{-1}), the Brillouin spectrum also shows a difference between the domain wall and a bulk domain (decrease of the Brillouin shift). It could be shown that existing theories for the Raman contrast can also be applied to explain the Brillouin contrast. Combined

Brillouin-Raman measurements demonstrated that both contrasts can be used for imaging purposes.

In a second application, the system was used to characterize the tumor biology of glioblastoma cells. The combination of the two spectroscopic methods allowed the biochemical properties to be correlated with the biomechanical properties. Thus, it could be determined that the nucleus has the highest stiffness within an adherent cell. A comparison between adherent cells and cells grown as spheroid revealed that the latter exhibit significantly higher stiffness, which should be taken into account when choosing a suitable tumor model. In addition, clinically relevant *IDH1* mutation was used to show that the genotype of a cell also affects biomechanics. Combined measurements indicated that proteins as well as in an indirect way also lipids significantly influence biomechanical properties.

These two applications illustrate the advantages of combining the two spectroscopic techniques. Their non-invasive, non-destructive and preparation-free operation provides the basis for further investigations also in other fields of application.

Kurzfassung

Die Schwingungsspektroskopie ist ein etabliertes Verfahren in der Materialwissenschaft sowie in der biomedizinischen Forschung zur Untersuchung von probenspezifischen Eigenschaften. Sie nutzt die Wechselwirkung von Licht (Photonen) mit Schwingungsquanten (Phononen) aus, um materialspezifische Informationen zu erlangen. Die Ramanspektroskopie ist sensitiv gegenüber optischen Phononen und findet seit der Erfindung des Lasers rege Verwendung. Im Gegensatz dazu untersucht die Brillouinspektroskopie die akustischen Phononen. Sie kam lange Zeit jedoch nur vereinzelt in der Materialwissenschaft zum Einsatz, da sie auf Grund der sequentiellen Spektrenaufnahme sehr zeitaufwendig war. Erst kürzlich konnte durch die Verwendung von einem *virtually imaged phased array* (VIPA) als dispersives Element im Brillouinspektrometer die Messzeit drastisch verkürzt werden, wodurch auch ein Einsatz in der biomedizinischen Forschung möglich ist. Im Rahmen dieser Dissertation wurde ein kombiniertes Brillouin-Raman-System aufgebaut, welches eine zeitgleiche und ko-lokalisierte Aufnahme von Brillouin- und Ramanspektren ermöglicht. Im Vergleich zu anderen Systemen, profitiert dieser Aufbau von der Verwendung zweier VIPAs mit unterschiedlichen freien Spektralbereichen was zu einer Entkopplung der spektralen Achsen und damit zu sensitiveren Messungen führt. Außerdem ermöglicht dies eine eindeutige Bestimmung von Brillouin-Verschiebungen. Darüber hinaus zeichnen die nahinfrarote Anregung bei 780 nm und die kontinuierliche Kalibrierung des Brillouinspektrums dieses System aus.

In einer ersten Anwendung wurden mit diesem kombinierten System ferroelektrische Domänenwände in periodisch gepoltem Lithiumniobat untersucht. Dabei stellte sich heraus, dass neben dem aus der Literatur bekannten Raman-Kontrast

(Intensitätsvariation bei 635 cm^{-1}) auch das Brillouinspektrum einen Unterschied zwischen der Domänenwand und einer flächigen Domäne aufweist (Verringerung der Brillouin-Verschiebung). Es konnte gezeigt werden, dass bestehende Theorien für den Raman-Kontrast auch verwendet werden können, um den Brillouin-Kontrast zu erklären. Kombinierte Brillouin-Raman Messungen verdeutlichten, dass beide Kontraste zu Bildgebungszwecken genutzt werden können.

In einer zweiten Anwendung, wurde das System dazu genutzt, die Tumorbiologie von Glioblastomzellen zu charakterisieren. Die Kombination der beiden spektroskopischen Methoden erlaubte es, die biochemischen mit den biomechanischen Eigenschaften zu korrelieren. So konnte ermittelt werden, dass der Zellkern die höchste Steifigkeit innerhalb einer adhärenen Zelle aufweist. Ein Vergleich zwischen adhärenent und als Sphäroid gewachsenen Zellen offenbarte, dass letztere eine signifikant höhere Steifigkeit aufweisen, was bei der Wahl eines geeigneten Tumormodells berücksichtigt werden sollte. Darüber hinaus konnte anhand der klinisch bedeutsamen *IDH1*-mutation gezeigt werden, dass sich auch der Genotyp einer Zelle auf die Biomechanik auswirkt. Kombinierte Messungen an Sphäroiden wiesen darauf hin, dass sowohl Proteine sowie indirekt auch Lipide maßgeblich die biomechanischen Eigenschaften beeinflussen.

Die beiden Anwendungen verdeutlichen, welche Vorteile eine Kombination dieser beiden spektroskopischen Verfahren mit sich bringt. Ihre nicht-invasive, zerstörungs- und präparationsfreie Arbeitsweise bietet dabei die Grundlage für weitere Untersuchungen auch in anderen Anwendungsfelder.

Contents

1	Introduction	1
2	Theoretical background	5
2.1	Inelastic light scattering	5
2.1.1	Raman spectroscopy	12
2.1.2	Brillouin spectroscopy	13
2.2	Requirements for the experimental setup	17
2.3	Multiple-beam interference	18
3	History and state of the art	23
3.1	Technical development of Raman and Brillouin spectroscopy	23
3.2	Combined Brillouin-Raman systems	28
4	Setup of the combined Brillouin-Raman system	31
4.1	Laser	31
4.2	Frequency locking	34
4.3	Bragg grating	37
4.4	Fabry-Pérot interferometer	39
4.5	Microscope	43
4.6	Reference beam path	44
4.7	Raman spectrometer	45
4.8	Rubidium absorption cells	46
4.9	Brillouin spectrometer	47
4.10	Brillouin shift axis calibration	51
4.11	Lorentzian fitting procedure	53

5 Applications	55
5.1 Domain walls in lithium niobate	55
5.1.1 Introduction	55
5.1.2 State of the science	56
5.1.3 Results	62
5.1.4 Discussion	73
5.1.5 Outlook	75
5.2 Tumor biology of glioblastoma cells	80
5.2.1 Introduction	80
5.2.2 State of the science	82
5.2.3 Results	84
5.2.4 Discussion	101
5.2.5 Outlook	103
6 Overall discussion and outlook	105
Bibliography	111
Appendix	135
A. Derivation of the dispersion relation for a monatomic linear chain . . .	135
B. Derivation of the Brillouin shift based on the Doppler effect	136
C. Derivation of the path length difference in a VIPA	137
List of Publications	141

Acknowledgments

I would like to take this opportunity to thank all the people who have supported me over the past years and made this work possible.

First of all, my greatest gratitude goes to Prof. Edmund Koch, who supervised me during my PhD thesis in an outstanding manner. On one hand, he gave me a goal-oriented guideline, which enabled me to complete the thesis within three years. On the other hand, there was enough free space for me to create my own ideas and broaden my horizon. I give him a lot of credit for always having an open ear for me and my issues. Besides his professional competence, I would like to emphasize his selfless personality and his impressive attitude towards life.

Moreover, I would like to thank Prof. Martin Hofmann for being the second reviewer. With his great expertise in optics and photonic instrumentation, he is ideally suited for this role.

Special thanks go to PD Roberta Galli, who was substantially involved in the development of the combined Brillouin-Raman system. As she did the first design of the experimental setup, it is her credit that the system is working so well. Besides her technical know-how, it is her calm and patient way that fascinates me and made working with her very pleasant.

A big thank goes to PD Ortrud Uckermann, who was my reliable contact for biological questions. Furthermore, she built the fruitful bridge to the Department of Neurosurgery, especially to Prof. Matthias Kirsch and Prof. Gabriele Schackert, who were responsible for the initiation of the project and the funding of the system by the National Center for Tumor Diseases.

Contents

Furthermore, I would like to thank all my colleagues from the KSM team. I believe that their plenty little helps in everyday life as well as the discussions over lunch built a substantial contribution to the success of this work. I very much enjoyed the cooperative atmosphere in the group and remember with pleasure our leisure activities.

During my PhD time, I got a lot of support and scientific input by several cooperation partners, wherefore I am very thankful. Namely, Dr. Anett Jannasch and Cindy Welzel from the Heart Center Dresden, Prof. Lukas Eng and Dr. Michael Rüsing from the Physics Department, and Dr. Robert Herber from the Department of Ophthalmology were reliable research partners.

From the financial side, I would like to thank the Free State of Saxony for granting me the Saxon scholarship. Without this funding, the present work would not exist. At this point, I would like to express my special thanks to Jonas Golde, who extraordinarily helped me during the application process.

Finally, my deepest thanks go to my friends and my family, who always support me with their unlimited help.

List of Figures

2.1	Scattering processes	6
2.2	Monatomic linear chain	8
2.3	Dispersion relation of phonons	9
2.4	Diatomic linear chain	9
2.5	Classification of phonons	11
2.6	Derivation of the Brillouin frequency shift	14
2.7	Scheme of the scattering signals	16
2.8	Visualization of the Airy formula	21
2.9	Scheme of a VIPA	22
3.1	Multi-pass tandem-Fabry-Pérot-based Brillouin spectrometer	24
3.2	Two-stage VIPA spectrometer	25
3.3	Time-domain Brillouin spectrometer	27
4.1	Experimental setup	32
4.2	Jablonski diagram of rubidium	34
4.3	Absorption bands of rubidium	35
4.4	Doppler-free saturation spectroscopy	36
4.5	Bragg grating	37
4.6	LabVIEW software	41
4.7	Microscope scheme	43
4.8	Interference pattern of the VIPA-spectrometer	47
4.9	Spectral axis separation	49
4.10	Exemplary Lorentzian fitting	54

List of Figures

5.1	Crystal structure of LiNbO_3	57
5.2	Momentum conservation condition	60
5.3	Types of domain walls	61
5.4	Effect of MgO-doping on the Raman spectrum of LiNbO_3	62
5.5	Sketch of the periodically-poled crystal	63
5.6	Sketch of the first-order interference pattern	66
5.7	z-cut spectra	67
5.8	x-cut spectra	68
5.9	y-cut spectra	69
5.10	Line scan 1	70
5.11	Line scan 2	71
5.12	Area scan	72
5.13	Speed of sound calculation	78
5.14	Kaplan-Meier plot for GBMs	80
5.15	Combined measurement of an adherent U87-MG cell	85
5.16	Mean spectra of the Raman clusters	86
5.17	Correlation of the Brillouin shift with the clusters	87
5.18	Brillouin intensity and linewidth map	88
5.19	High-resolution Raman map of an adherent U87-MG cell	90
5.20	Exemplary Brillouin maps of a U87-MG spheroid	91
5.21	Cumulative histograms of the adherent cell and spheroids maps	92
5.22	Comparison between adherent cell and spheroid biomechanics	93
5.23	Combined line scans on U87-MG spheroids	95
5.24	Lipid content in spheroid sections	96
5.25	Brillouin and CARS measurements on primary cell lines	98
5.26	Combined measurements on IDH1 wild-type and mutated spheroids	100
C.1	Geometrical relationships in a VIPA	138

List of Tables

5.1	Raman selection rules	58
5.2	Primary cell lines	97

Abbreviations

FPI	Fabry-Pérot interferometer
VIPA	virtually imaged phased array
FSR	free spectral range
FWHM	full width at half maximum
CCD	charged coupled device
ASE	amplified spontaneous emission
CoSy	compact saturation spectroscopy
PID	proportional-integral-derivative
TTL	transistor-transistor logic
LiNbO₃	lithium niobate
GBM	glioblastoma
IDH1	<i>isocitrate dehydrogenase 1</i>
AFM	atomic force microscopy
CARS	coherent anti-Stokes Raman scattering

1 Introduction

The determination of material properties is a concern we are familiar with from everyday life. This becomes clear, for example, when going to the doctor and they use x-rays to check whether our bones or teeth are intact. Beyond that, x-rays are also used for the characterization of non-biological materials, such as in x-ray diffraction, x-ray reflectometry and x-ray fluorescence. The linking element between these applications is the utilization of the physical properties of x-rays. Beyond that, there are many other fundamental physical principles that are used for both biomedical issues and material characterization, such as nuclear magnetic resonance and ultrasound propagation.

The vibration of atoms in matter is another such key principle. Because oscillations are directly related to the structure and composition of a material, they bear a plenty of information, for example, about mechanical and chemical properties. A precise characterization of such quantities is vital in many research areas as it enables, for instance, a tuning of material parameters into a desired direction or the development of new therapeutic approaches after understanding elementary functionalities.

Optical spectroscopy, such as Raman and Brillouin spectroscopy, is a technique that is sensitive to these vibrations. Since the invention of lasers in the 1960s, Raman spectroscopy is commonly used for characterizing molecular vibrations and chemical bonds. In contrast, Brillouin spectroscopy can be used to investigate vibrations associated with the sound propagation yielding information about viscoelastic properties. Only recently, the technical advancement of spectrometers made it possible to perform Brillouin measurements in an efficient manner and thus allowing widespread application in biomedical research as well as material science [1].

1 Introduction

Compared to other structural characterization methods, Brillouin and Raman spectroscopy have advantages such as being all-optical, contact- and label-free as well as non-destructive. Moreover, by using a microscope design, spatial resolutions at μm -scale can be achieved. Another advantage is that no time-consuming sample conditioning and preparation is necessary. Therefore, both spectroscopic methods decisively complement the spectrum of methods.

The aim of the research presented in this thesis is to combine both spectroscopic methods to obtain information going beyond using either method alone. The combination is possible due to the fact that both techniques are based on inelastic scattering of light and thus can straightforwardly be united in one experimental setup.

In this work, first, the theoretical fundament of inelastic light scattering on phonons is covered in chapter 2 in order to identify the requirements for the experimental setup. Additionally, the concept of multiple-beam interference will be introduced, which is relevant for two key optical components in the setup. Chapter 3 discusses the current state of combined Brillouin and Raman systems in the literature. This is used to delineate the features of the experimental setup used in this work, which is described in chapter 4. Two applications of the system in current research are presented in chapter 5.

On one hand, combined Brillouin and Raman investigations are used to characterize domain walls in ferroelectric LiNbO_3 , which is a promising material for future optoelectronic and optomechanical applications. Present theories about the physics of domain walls, which are mainly based on former Raman measurements, are reviewed in the context of novel Brillouin findings. A special focus is set on an intrinsic topological effect generating an extra-quasi-momentum, which occurs at extended planar defects like domain walls.

On the other hand, the interplay of biochemistry and biomechanics is investigated in the field of oncology. Tumor diseases are coming along with changes in the metabolism, which allow oncological processes like proliferation, infiltration and metastasis. In order to prevent tumor spreading and enabling effective therapeutic treatment, a deep understanding of functional relations in tumor biology is needed. A first step in this direction is done by a precise characterization of tumor cell properties.

A final discussion on the feasibility of combined Brillouin and Raman spectroscopy in the biomedical and the material science applications is given in chapter 6 as well as an outlook with future perspectives.

2 Theoretical background

In this chapter, the physical fundamentals of Brillouin and Raman spectroscopy are described. As both techniques are based on the interaction of photons with phonons, first, the phenomenon of inelastic light scattering on vibrations is introduced. Afterwards, the requirements for the experimental setup are derived from these theoretical considerations. Moreover, the principle of multiple-beam interference will be covered, because it is exploited by two important components of the system.

2.1 Inelastic light scattering

In 1922 and 1928, respectively, Léon Brillouin and Chandrasekhara Venkata Raman discovered that after interaction with matter, there is a small fraction of light that has a slightly shifted wavelength [2,3]. It turned out that the interaction of photons (light quanta) with phonons (vibrational quanta) is the reason for this observation. Thus, their finding forms the basis for optical methods like Brillouin and Raman spectroscopy, which can be used to obtain information about the vibrations in a sample and associated material properties.

Considering the quantum mechanical situation of a scattering event of an incident photon with energy $E_i = \hbar\omega_i$ with a phonon with energy $E_p = \hbar\Omega$, where $\hbar = \frac{h}{2\pi}$ denotes the reduced Planck constant and $\omega = 2\pi\nu$ the angular frequency, there are three cases that can occur:

2 Theoretical background

- Rayleigh scattering: The incident photon is elastically scattered. Consequently, due to the conservation of energy, the angular frequencies of the incident and the scattered photon are the same, i.e. $\omega_i = \omega_s$.
- Stokes scattering: The incident photon is inelastically scattered, whereby a phonon is generated. The scattered photon then has a lower energy $E_s = \hbar(\omega_i - \Omega)$.
- anti-Stokes scattering: The incident photon is inelastically scattered, whereby it annihilates a phonon and receives its energy. The scattered photon then has a higher energy $E_s = \hbar(\omega_i + \Omega)$.

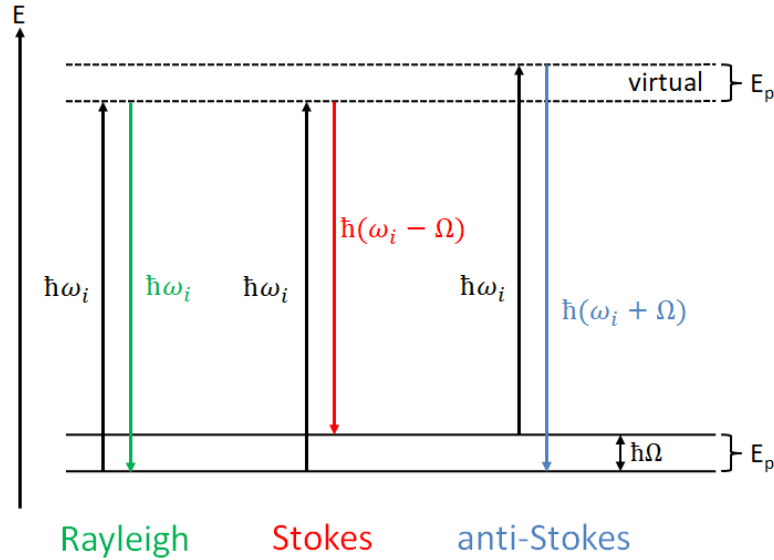


Figure 2.1: Besides the elastic Rayleigh scattering at which the frequency of the scattered photon is the same like that of the incident one, there is inelastic scattering, whereby either the energy of a phonon is emitted by a photon (Stokes scattering) or the energy of a phonon is received by a photon (anti-Stokes scattering). Scheme is adapted from [4].

It should be mentioned that the elastic Rayleigh scattering process is orders of magnitude ($> 10^6$) more likely than the two inelastic scattering processes [4, 5]. However, only the latter contain information about the sample, as only in these processes the scattered photon undergoes a frequency shift $|\omega_i - \omega_s| = \Omega$. Figure 2.1

2.1 Inelastic light scattering

shows the scattering processes in an energy level scheme, whereby the dashed lines emphasize that the excited energy levels are in general virtual states possessing an arbitrary energy [4]. Hence, scattering processes are always possible, independently of the chosen excitation wavelength. In the special case where the upper energy level coincides with a real state, much stronger resonant scattering is possible, which is exploited in *resonance Raman spectroscopy*.

Furthermore, Figure 2.1 shows that both the Stokes and the anti-Stokes scattering process yield the same information. The frequency of the scattered photon with respect to that of the incident photon is in both cases shifted by the same amount, i.e. the phonon frequency Ω . Once it is shifted to lower frequencies (Stokes) and once to higher frequencies (anti-Stokes). Therefore, both processes can be used for determining the phonon frequency. Thus, the phonon frequency, as the quantity that gives information about the sample properties, is given as (photon) frequency shift in Brillouin and Raman spectra.

Up to this point, all discussed principles are the same for Brillouin and Raman scattering, since both rely on the interaction of photons with phonons. In the following, the differences between these scattering processes will be discussed, which originate from the different types of phonons interacting with the photons.

For this purpose, a deeper insight into the nature of vibrations is necessary. In general, vibrations describe the periodic motion of something. Here, this is the periodic motion of atoms within matter. Although an object is macroscopically at rest, the atoms inside are not rigid but permanently in motion. However, these movements are small and on average cancel each other out.

In the following, a linear chain of infinity point masses (cf. Fig. 2.2) will be used as a simplified model for understanding vibrations in a material. The point masses are representing atoms held together by springs, which are simulating chemical bonds. In a first case, all point masses shall have the same mass m and all springs shall have the same spring constant D . When the one-dimensional chain is at rest, the distance between the point masses amounts to a .

2 Theoretical background

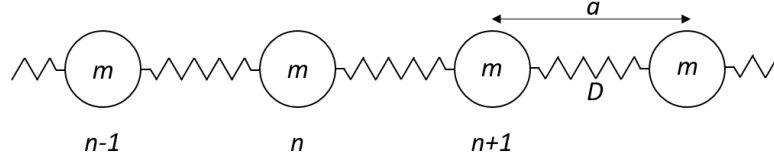


Figure 2.2: A linear chain of infinity point masses can be used as a simplified model to study vibrations in a material. In this model, each point mass symbolizes an atom being connected to a left and a right neighbor via springs, which represent chemical bonds.

After an external stimulation, the point masses are performing oscillations periodically around their rest positions. It shall be assumed that these displacements Δu are small and thus the deformation of the springs can be described by Hook's law, i.e. the restoring force is $f_r = -D \cdot \Delta u$.

Assuming that the restoring forces are small and thus only interactions between neighboring point masses have to be considered, the following ordinary differential equation can be derived for the motion of the n -th point mass characterized by its position u :

$$m\ddot{u}_n = -D(u_n - u_{n-1}) + D(u_{n+1} - u_n) = D(u_{n-1} + u_{n+1} - 2u_n) \quad (2.1)$$

It can be solved by the following ansatz:

$$u_n = u_n(\omega, k, t) = u_0 e^{i(kna - \omega t)} \quad (2.2)$$

where u_0 is the initial position of the point mass, t the time variable, and ω and k the (angular) frequency and the wavevector of the vibration, respectively. Inserting equation 2.2 in 2.1 allows to determine a functional relationship between ω and k , the so-called dispersion relation. In the case of a monatomic chain it is given by following equation (a detailed derivation is given in appendix A):

$$\omega(k) = 2\sqrt{\frac{D}{m}} \left| \sin\left(\frac{ka}{2}\right) \right| \quad (2.3)$$

This dispersion relation is sketched in Figure 2.3a for k -values between $-\frac{\pi}{a}$ and $\frac{\pi}{a}$. It is noteworthy that close to $k = 0$ the slope of the curve, which determines the group velocity $v_G = \frac{d\omega}{dk} \approx \sqrt{\frac{Da^2}{m}}$, is almost constant.

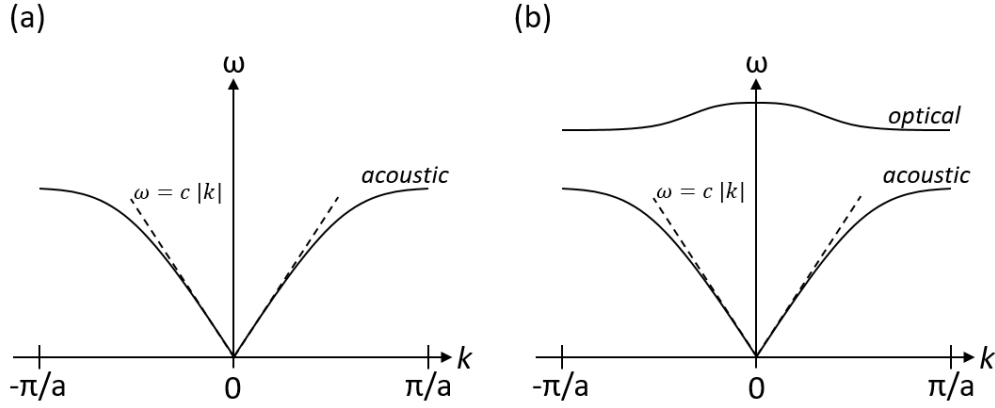


Figure 2.3: Sketch of the dispersion relation of (a) a linear monatomic chain and (b) a linear diatomic chain showing that besides the acoustic phonon branch, the optical phonon branch is only present in the latter one.

A different picture arises, when considering a diatomic chain in the next case (cf. Fig. 2.4). Here, point masses with masses m and M are arranged in an alternating manner. Due to the different masses the periodicity of the chain a has doubled. Again, ordinary differential equations can be used to describe the motion of the point masses. Because of the two different masses, also two differential equations are needed. One describing the position u of the n -th point mass of the first type, and one describing the position v of the adjacent point mass of the other type:

$$M\ddot{u}_n = -D(2u_n - v_n - v_{n-1}) \quad (2.4)$$

$$m\ddot{v}_n = -D(2v_n - u_n - u_{n+1}) \quad (2.5)$$

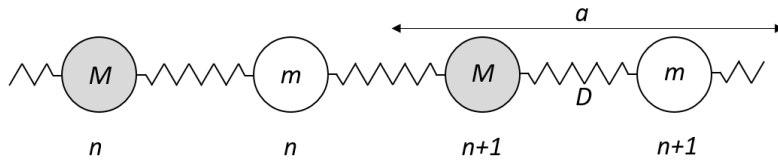


Figure 2.4: A diatomic chain of alternating point masses results in two different solutions for the dispersion relation, i.e. the acoustic and the optical phonon branch.

2 Theoretical background

This coupled ordinary differential equation system can be solved by a similar ansatz to equation 2.2, only modifying the location of the n -th point masses:

$$u_n = u_n(\omega, k, t) = u_0 e^{i(k(n-\frac{1}{4})a - \omega t)} \quad (2.6)$$

$$v_n = v_n(\omega, k, t) = v_0 e^{i(k(n+\frac{1}{4})a - \omega t)} \quad (2.7)$$

Inserting equations 2.6 and 2.7 in the coupled differential equations results in two solutions for the dispersion relation (detailed derivation can be found in [6]):

$$\omega_{\pm}^2 = D \cdot \left(\frac{1}{m} + \frac{1}{M} \right) \pm D \cdot \sqrt{\left(\frac{1}{m} + \frac{1}{M} \right)^2 - \frac{4}{m \cdot M} \cdot \sin^2 \left(\frac{ka}{2} \right)} \quad (2.8)$$

A sketch of the two solutions is shown in Figure 2.3b. The ω_- solution is similar to that obtained for the monatomic chain, i.e. close to $k = 0$, there is a linear dispersion relation, whereas close to $\pm \frac{\pi}{a}$, ω reaches a maximum value. The ω_+ solution, however, is totally different. At $k = 0$ it does not start at $\omega = 0$, but already amounts to $\sqrt{2D \left(\frac{1}{m} + \frac{1}{M} \right)}$. The group velocity (slope) at this k -value, however, is zero, meaning that the wave is not propagating. At $|k| > 0$ the curve slightly decreases to a minimal value at $\pm \frac{\pi}{a}$, which, however, is still higher than the maximum value of the ω_- solution.

These two curves are named *acoustic* (ω_-) and *optical* (ω_+) branch. The naming refers to the properties of the underlying vibrations: acoustic vibrational modes are propagating waves that show a linear dispersion relation at $k \approx 0$, which is known from sound propagation, wherefore they are called *acoustic*. On the other hand, optical vibrational modes can be excited by absorbing infrared light, wherefore they are called *optical*.

The different characteristics of acoustic and optical phonon modes have an impact on the displacement of adjacent point masses, too (cf. Fig. 2.5). They are oscillating almost in phase in the case of acoustic modes, whereas they are oscillating in opposite directions, i.e. out of phase, in the case of optical phonons. This directly explains their different group velocities: If adjacent point masses are moving almost in phase, then a travelling wave with velocity v_G is created. In contrast, if adjacent point masses are moving out of phase, the wave is not propagating, thus a standing wave.

All in all, the diatomic linear chain model predicts two different types of vibrational modes. When generalizing this model by going from one to three dimensions, the characteristic of these two phonon types stays the same. Only the number of acoustic and optical phonon modes increases with the degrees of freedom.

Another point associated with the generalization to three dimensions is that atoms now not only have two neighbors, but have neighbors (and thus mechanical interactions) in all three spatial dimensions. This results in the fact that not only longitudinal but also transverse phonon modes are allowed. Hence, phonons can be classified by the displacement direction of two neighboring atoms to each other (acoustic versus optical) and by their displacement with regard to the propagation direction of the wave (longitudinal versus transversal) as sketched in Figure 2.5.

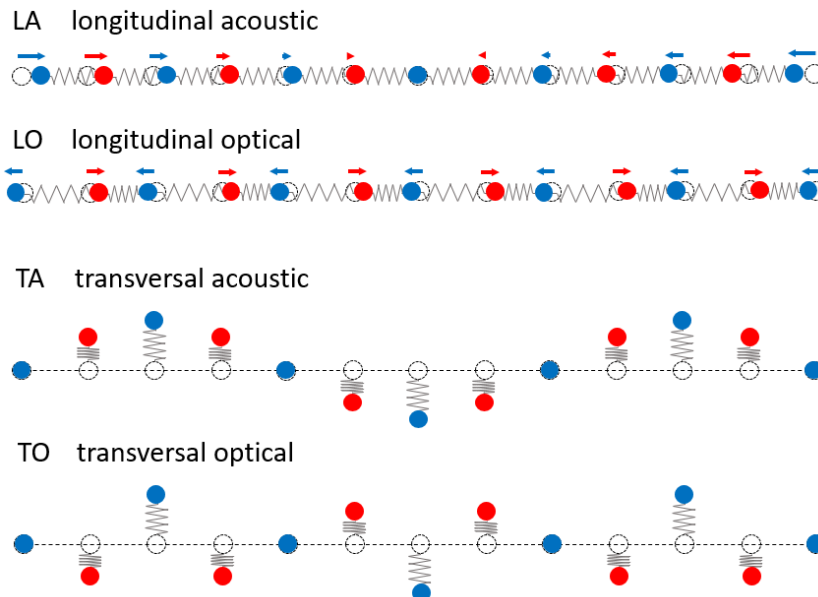


Figure 2.5: Phonons can be classified by the direction of the atom displacement with respect to the wave propagation direction (longitudinal versus transversal) and by the displacement of two adjacent atoms (acoustic versus optical). Scheme is adapted from [6].

Returning now to the question of what the difference is between Brillouin and Raman scattering. It is the type of phonon interacting with the photon. In case of Brillouin scattering the phonons are acoustic ones, whereas they are optical ones

2 Theoretical background

for Raman scattering. This difference, which might be marginal at first glance, has great consequences on the experimental setup, which will be discussed in section 2.2. Before that, the characteristics of both spectroscopic methods will be covered separately.

2.1.1 Raman spectroscopy

Raman spectroscopy, which is the inelastic scattering of light by optical phonons, is a well-established tool for gaining insights into the chemical bonds of a material and thus its composition. In general, there are $3N - 6$ optical phonon modes, where N is the number of atoms in a molecule [7]. The remaining six modes are associated with rotational and translational degrees of freedom. When considering biological samples consisting of macro-molecules like carbohydrates, lipids or proteins, the number of atoms and thus the number of Raman modes is very large. Hence, the Raman spectra consist of plenty of Raman bands, which are building a characteristic *fingerprint* of the sample.

A different picture emerges when investigating crystalline matter. Here, the high symmetry of the crystal lattice allows us to restrict ourselves to one unit cell, because the whole crystal is made up of such unit cells. The number of optical phonon modes in a crystal amounts to $3N - 3$, where N is the number of atoms in a unit cell [8]. Generally, this number is much less than the number of atoms in a macro-molecule. Thus, Raman spectra of crystalline matter show only a few distinctive Raman bands.

In general, the full number of optical phonon modes is not observable in a Raman spectrum. For example, it might happen that the intensity of a Raman band is so small that it gets lost in the noise. Or two Raman bands appear at the same spectral position, which therefore cannot be distinguished from each other anymore. Apart from these instrumental limitations, there are so-called selection rules, which originate from the vibrations themselves: Only those optical phonons are Raman active, where the polarizability changes its value during the vibration [8].

In contrast to this, the related infrared spectroscopy is only sensitive to optical phonons, where the dipole moment changes during vibration. Hence, both methods

complement each other. As in both techniques the vibrational frequency is most commonly given in terms of a wavenumber (shift) in cm^{-1} , the spectra are easy to compare. The wavenumber $\tilde{\nu}$ can be calculated as follows:

$$\tilde{\nu} = \frac{1}{\lambda} = \frac{\nu}{c} \quad (2.9)$$

where λ is the wavelength and c the speed of light.

A feature of Raman spectroscopy is that the spectrum is almost independent of the excitation wavelength. This can directly be derived from the dispersion relation, when considering the momentum conservation during the photon-phonon interaction: Photons have a small momentum $\hbar k$ that is close to zero. Thus, interactions with phonons are only possible close to $k = 0$. At these wavenumbers, the optical branch of the dispersion curve is almost constant, wherefore the phonon frequency is independent of the excitation wavelength. Therefore, Raman spectra recorded from different systems are generally comparable if no resonance effects occur at an absorption band. However, the scattering cross-section is wavelength dependent ($\sim \frac{1}{\lambda^4}$), wherefore the band intensity can vary considerably. Furthermore, wavelength-dependent fluorescence can lead to differences in the spectra.

For Raman scattering, typical phonon wavenumbers are between $100 - 4000 \text{ cm}^{-1}$. This corresponds to a wavelength shift of $5 - 200 \text{ nm}$ for an 780 nm excitation.

2.1.2 Brillouin spectroscopy

Brillouin spectroscopy, which utilizes the inelastic scattering of light on acoustic phonons, is an established technique in material science for determining mechanical properties. However, it is still in its infancy in biomedical research. One reason for this is the small frequency of the acoustic phonons (about a thousand times smaller than optical phonons), which can again be seen in the phonon dispersion relation: Around $k = 0$, the frequencies of the acoustic branch are close to zero. As a consequence, the instrumental effort to detect the acoustic phonons is much greater. In former times, this came along with unacceptable long measuring times for biomedical applications.

Another feature can be deduced from the dispersion curve: In contrast to the

2 Theoretical background

optical branch, the frequency of the acoustic branch is at small wavenumbers not independent of the excitation wavelength, but shows a linear dependence. Hence, Brillouin spectra acquired with different systems are not readily comparable and thus should always be reported with the utilized excitation wavelength in order to allow a conversion of the measured frequency shifts.

Another point of fundamental difference between the two spectroscopic methods is that there are only three acoustic phonon modes in each material. Therefore, a Brillouin spectrum has in general much less information content. Therefore, it cannot be used to unambiguously identify compounds in a material like Raman spectroscopy is able to. But on the other hand, the simplicity of the spectrum allows a clear determination of band parameters like the peak center position, the maximum intensity and the full width at half maximum.

Moreover, the number of observable acoustic phonon modes is dependent on the scattering geometry. For isotropic materials, only longitudinal phonon modes are observable in back-scattering configuration, whereas a 90° -scattering-geometry is also sensitive to transverse phonon modes [9].

In the following, a derivation of the Brillouin frequency shift will be made on the basis of the Bragg condition for constructive interference: In a medium with refractive index n , a periodic density fluctuation, which is nothing else than a longitudinal sound wave, shall travel with velocity v_s as illustrated in Figure 2.6.

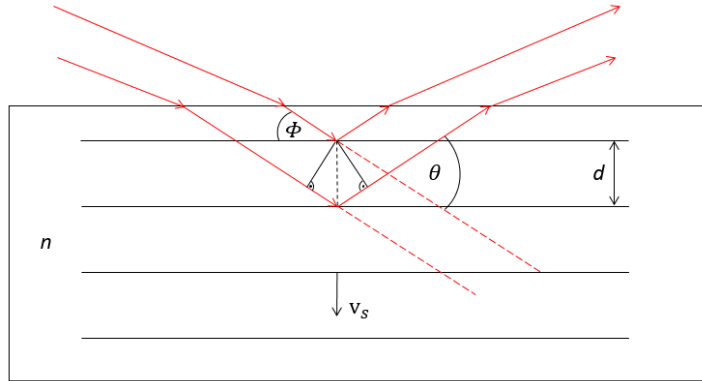


Figure 2.6: The Brillouin frequency shift can be derived by applying the Bragg condition for constructive interference for a light wave being reflected under $\Phi = \frac{\theta}{2}$ by the wavefronts of an acoustic wave, which are spaced by d and traveling with v_s . Scheme is adapted from [10].

2.1 Inelastic light scattering

Assuming a distance d between the sound wavefronts (i.e. the phonon wavelength), then the Bragg condition for an incident light wave reads as follows:

$$2 d \sin(\Phi) = m \lambda_n \quad (2.10)$$

where Φ is the angle between the incident light and the sound wave front, $\lambda_n = \frac{\lambda}{n}$ the light wavelength in the medium, and m the interference order.

Considering only the first interference order $m = 1$ and substituting $\Phi = \frac{\theta}{2}$ by the scattering angle θ , the distance d amounts to:

$$d = \frac{\lambda}{2 n \sin\left(\frac{\theta}{2}\right)} \quad (2.11)$$

In a last step, the Brillouin frequency shift ν_B , which is equal to the phonon frequency, can be calculated by $\nu_B = \frac{v_s}{d}$ (note the similarity to the well-known light wave equation $\nu = \frac{c}{\lambda}$ as both rely on a linear dispersion relation):

$$\nu_B = \frac{2 n v_s}{\lambda} \sin\left(\frac{\theta}{2}\right) \quad (2.12)$$

The equation shows that the Brillouin shift is on one hand dependent on instrumental parameters like the excitation wavelength and the scattering angle, and on the other hand on material properties like the refractive index and the sound velocity. Hence, by knowing the properties of a material, the Brillouin shift can easily be calculated for a given instrumental system. Typical Brillouin shift values are in the range of $3 - 45 \text{ GHz}$, which corresponds to $0.1 - 1.5 \text{ cm}^{-1}$ or a shift in wavelength of $6 - 91 \text{ pm}$ for 780 nm excitation, respectively. Another derivation of the Brillouin shift based on the Doppler effect can be found in appendix B, which is intended to highlight the small frequency shift that a light wave experiences when it interacts with a much slower sound wave.

It is the sound velocity v_s in equation 2.12, which links the Brillouin shift to the mechanical properties of a sample [11]. The real part of the complex longitudinal modulus $M^* = M' + M''$ is given by

$$M' = \rho v_s^2 \quad (2.13)$$

2 Theoretical background

and describes the relationship between axial stress and axial strain in a uni-axial compression/strain state and therefore provides information about the stiffness of a sample [11]. In contrast, the imaginary part

$$M'' = \frac{\rho v_s^2 \Delta}{\nu_B} \quad (2.14)$$

is a measure for viscosity, where Δ is the full width at half maximum of the Brillouin band [11]. All in all, a Brillouin spectrum thus provides information on the visco-elastic properties of a sample.

Figure 2.7 summarizes the key considerations of this section by sketching the Raman and Brillouin signals on a spectral axis. The strong Rayleigh band in the center indicates that both Raman and Brillouin scattering are much weaker. Symmetrical to this unshifted signal are the Brillouin bands being frequency shifted by several GHz . Also symmetrically, but in the THz -range, shifted are the Raman signals.

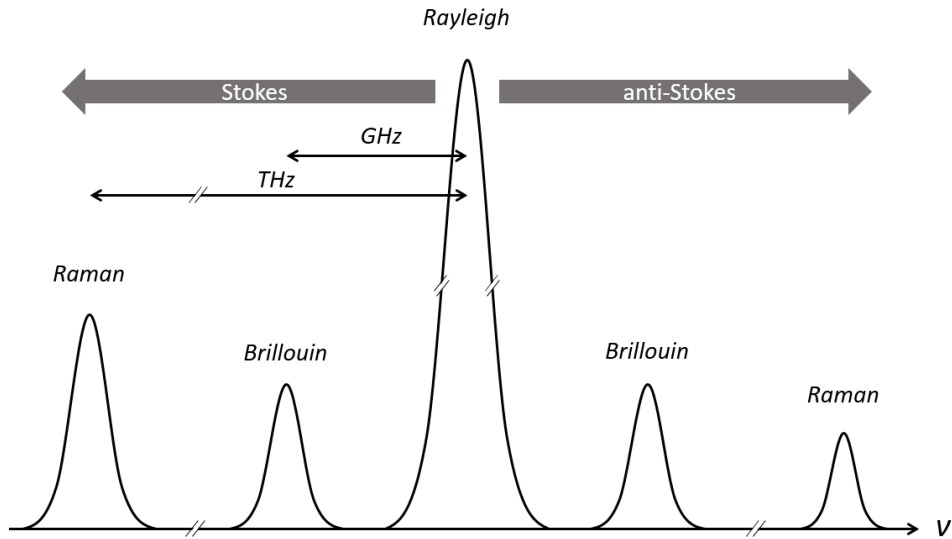


Figure 2.7: Overview of the possible scattering processes, i.e. besides elastic Rayleigh scattering, much weaker inelastic Raman (large frequency shift) and Brillouin scattering (small frequency shift) occurs. For Raman scattering, the Stokes process is highly preferred compared to the anti-Stokes process. Scheme is adapted from [12, 13].

2.2 Requirements for the experimental setup

Another feature gets apparent in Figure 2.7: For Raman scattering, the anti-Stokes signals are weaker than the Stokes ones. In contrast, both signals have almost same intensity in the case of Brillouin scattering. This can be explained by the Bose-Einstein statistics. According to this, higher energy levels are occupied less frequently than lower ones. Hence, the probability finding it in the excited state is higher than vice versa. This explains why the Stokes Raman process, starting from the ground state is more likely than the anti-Stokes process, which starts from an excited state (cf. Fig. 2.1). In the case of Brillouin scattering, the two states have an energy difference much less than the thermal energy $k_B T$, which amounts to 25 meV (corresponding to 6 THz) at room temperature. Hence, in Brillouin spectroscopy usually Stokes and anti-Stokes bands are measured, whereas in Raman spectroscopy only the Stokes signals are considered.

The natural linewidths for Brillouin and Raman scattering is determined by the phonon lifetime [14].

2.2 Requirements for the experimental setup

Requirements for the experimental setup of a combined Brillouin-Raman system can directly be derived from the theoretical considerations on inelastic scattering. This derivation shall be done in this section.

Because both methods are based on inelastic light scattering, a photon source is essential. In order to be able to determine a frequency shift after the scattering process, a monochromatic light source is needed. This requirement is generally met by a laser. Due to the weakness of the Brillouin and Raman effect, the laser line intensity has to be several orders of magnitude higher than parasitic signals such as laser side bands and continuous background from spontaneous emission, which therefore have to be eliminated [15]. Furthermore, the wavelength has to be long-term stable in order to ensure, especially for Brillouin scattering that the frequency shifts are reproducible. Another crucial point regarding the light source is its bandwidth. It has to be as narrow as possible, to ensure minimal line broadening. Thus, it should be in the sub- MHz regime so that it is at least two orders of magnitude smaller than typical Brillouin linewidths [16].

2 Theoretical background

In the further course of the experiment, an apparatus is needed that ensures a constant scattering geometry, because both Raman and Brillouin scattering depend on this. For example, this can be achieved by a microscope where both the incident and scattered photons are passing through the same objective (180°-back-scattering geometry). It should be mentioned that high-NA objectives relax the scattering geometries. Furthermore, the usage of objectives enables a focusing of the laser beam and thus allows high resolution measurements.

After the scattering event happened, an analyzing unit is required, which is able to determine the frequency shift of the scattered light. Since this shift is fundamentally different for Brillouin and Raman scattered light as described in section 2, two separate spectrometers are needed. Therefore, the scattered light has to be split into two channels. The splitting criteria is the wavelength of the scattered light. Unshifted (Rayleigh) and slightly shifted (Brillouin) light goes into one channel, whereas strongly shifted (Raman) light goes into another channel.

In a next step, the Rayleigh scattered light has to be filtered out. This is necessary in order to be able to more sensitively measure the Brillouin and Raman signals, which are orders of magnitude lower than the Rayleigh scattered light.

Consequently, the light has to be separated into its various wavelengths allowing the determination of the scattered photon frequency and thus the calculation of the phonon frequency. The spectral decomposition is realized in spectrometers, which contain a dispersive element as the main component.

Finally, this light needs to be collected by a detector and converted into a digital signal. To be able to measure the weak Brillouin and Raman signals, the detector should have a high quantum efficiency and extremely low noise allowing to convert almost each photon into an electronic signal with rare noise. Moreover, the detector has to be shielded from any stray light, which would dramatically lower its sensitivity or even disallow to measure the weak signals.

2.3 Multiple-beam interference

As pointed out in the previous section, the frequency shift is extremely small in case of Brillouin scattering. This results in the fact that typical instrumental

2.3 Multiple-beam interference

approaches, which are used for instance in Raman spectroscopy, are not capable of performing Brillouin spectroscopy. Particularly at three points in the experimental setup special solutions are needed for Brillouin spectroscopy.

The first challenge arises from the laser line cleaning in the excitation unit. An extremely narrow band-pass filter is needed, in order to only transmit the laser line, but block any light that is spectrally right next to it. Otherwise, these additional signals would either be misidentified as Brillouin signals or would mask weak Brillouin signals, depending on whether they are discrete or continuous.

Moreover, a similar challenge occurs when filtering the Rayleigh light. As only the Rayleigh light should be blocked, but the scattered light of interest is spectrally very close to it, a ultra-narrow notch filter is needed.

The third crucial point is the separation of the wavelengths in the spectrometer. Since gratings, which are often used for this purpose and suitable for Raman spectrometers, reach their resolution limit in case of Brillouin scattered light, new optical approaches and components are needed, which allow a very high dispersion.

While the Rayleigh light filtering can be done by vapor absorption, which is described in section 4.8, the laser line cleaning and the wavelength separation require a more sophisticated solution. This is provided by multiple-beam interference. It is instrumentally used in both a Fabry-Pérot interferometer (FPI) and a virtually imaged phased array (VIPA) in order to meet these challenges. Since both are key components of the experimental setup and essential for performing Brillouin spectroscopy, this section covers the basic principles of multiple-beam interference. A FPI is mainly composed of two plane-parallel surfaces being reflective ($R > 80\%$) and therefore acting as semi-transparent mirrors. They are separated by a piezoelectric medium, so that the distance d between the mirrors can incrementally be varied by applying a voltage. This is exploited in order to change the optical path length within this resonator. To allow light of wavelength λ to pass the FPI, the condition for constructive interference must be fulfilled; i.e. the path difference between a light wave that passes the FPI without any reflection and a light wave that is reflected back and forth once, amounts to an integer multiple m of the wavelength:

$$\Delta s = 2 n d = m \lambda \tag{2.15}$$

2 Theoretical background

where n is the refractive index of the medium between the mirrors.

Only wavelengths which almost meet this condition are transmitted by the FPI. All other wavelengths are reflected. When choosing the path difference to transmit only the laser wavelength, the FPI can be used as laser line cleaner.

The transmitted intensity I_T of a FPI can be described by the Airy formula (detailed derivation can be retraced in [17])

$$I_T = I_0 \cdot \frac{1}{1 + G \sin^2\left(\frac{\delta}{2}\right)} \quad (2.16)$$

where I_0 is the maximum transmitted intensity, $\delta = 2\pi \frac{\Delta s}{\lambda}$ the phase difference and $G = \frac{4R}{(1-R)^2}$ a factor considering the mirror reflectivities. The mathematical relationship is plotted in Figure 2.8 for different reflectivities as function of the phase difference. It is evident that the transmission behavior is strongly dependent on the reflectivity of the mirrors. The higher the reflectivity is, the narrower gets the transmission band width and the stronger gets the suppression of the wavelengths, which do not meet the interference condition. A measure that describes this behavior is the finesse $\mathcal{F} = \frac{\pi}{2} \sqrt{G} = \frac{\pi \sqrt{R}}{1-R}$. High finesses can be achieved by high reflectivities resulting in an ultra narrow spectral band-pass. The finesse can thus be understood as a measure, which describes the number of beams that interfere with each other.

In Figure 2.8 a second characteristic gets apparent. There is not just one single transmission peak, but multiple. This is the consequence of the fact that for a given mirror spacing the interference condition is fulfilled for several wavelengths. The spectral distance between two transmission peaks is named free spectral range (FSR) and typically given as a frequency $\nu_{FSR} = \frac{c}{2nd}$. It is directly related to the finesse via the full width at half maximum (FWHM) of the transmission peak:

$$\mathcal{F} = \frac{FSR}{FWHM} \quad (2.17)$$

Summing up, the multiple-beam interference occurring in a FPI can be used to suppress undesired wavelengths. However, in addition to the laser wavelength also other wavelengths are transmitted by the FPI, which are spectrally multiples of a FSR next to it.

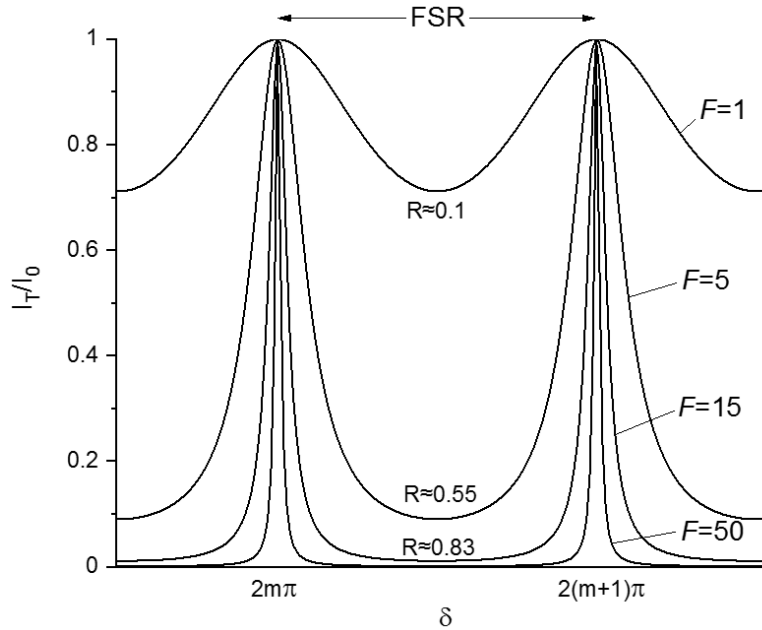


Figure 2.8: The visualization of the Airy formula shows that the transmission linewidth decreases with increasing reflectivity R and finesse \mathcal{F} , whereas the extinction of the background increases. Scheme is adapted from [17].

The phenomenon of multiple-beam interference is also used in VIPAs. Similar to a FPI, they consist of two plane-parallel mirroring surfaces, too. One mirror is reflecting almost all light ($R \approx 100\%$) and the other about $R \approx 95\%$ (cf. Fig. 2.9). In contrast to a FPI, the distance between the mirrors t is constant here. Therefore, the transmitted wavelength cannot be selected by varying the mirror spacing. For this reason, another way is needed for VIPAs to create different optical path lengths. Here, the laser beam is focused on an entrance slit onto the rear mirror. Minor tilting of the VIPA ensures that after the first back-reflection the beam is traveling back and forth between the mirrors. At this point, the name *virtually imaged phased array* becomes clear; all the back-reflections can be imagined as light from separate sources having an offset to each other, which is indicated in Figure 2.9. Here, the different optical path lengths result from the fact that the incident beam has a certain divergence and thus sub-beams enter the VIPA under different angles α_{VIPA} .

2 Theoretical background

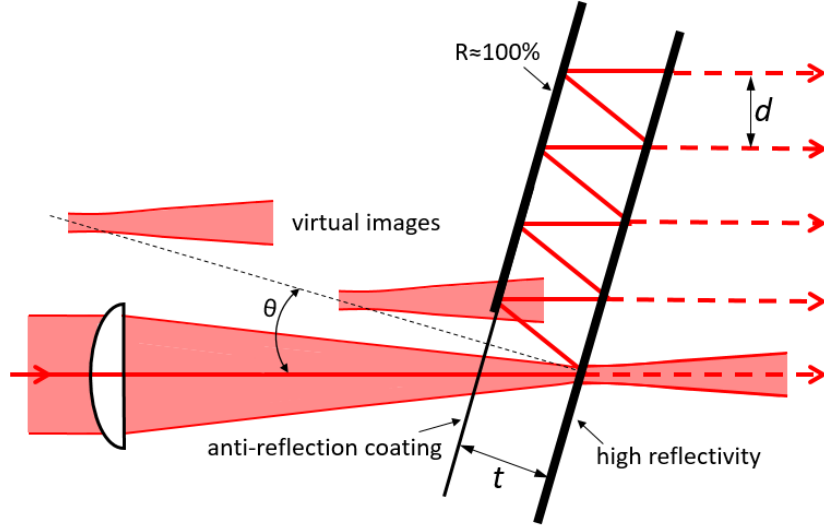


Figure 2.9: Scheme of a VIPA, mainly consisting of a glass plate with two high reflective surfaces. Only a small anti-reflection coated window allows the beam to enter the etalon. The indicated array of virtual light sources explains the naming. Scheme is adapted from [18].

The path difference of each sub-beam amounts to

$$\Delta s = 2 t \cos(\alpha_{VIPA}) \quad (2.18)$$

A detailed derivation on the basis of geometrical relations is given in appendix C. This relationship shows that in contrast to the FPI, the path difference and thus the transmission behavior for different wavelengths can be tuned by the tilting angle of the VIPA instead of the mirror spacing. Since simultaneously a bunch of sub-beams with different angles enters the VIPA, a spectrum can be obtained at one shot. This is in fundamental contrast to the FPI, where all the wavelengths have to be scanned sequentially in order to acquire a spectrum.

Analogous to the FPI, the interference condition is also fulfilled for different wavelengths in the case of VIPAs. Again, they are separated by multiples of the FSR and the finesse determines its band width.

Summing up, the multiple-beam interference occurring in a VIPA can be used to spectrally separate light with slightly different wavelengths and can thus be used as dispersive element in a spectrometer.

3 History and state of the art

In this chapter, current combined Brillouin-Raman systems from the literature are presented including research conducted with these systems. First, however, the development of Raman and Brillouin systems over the last decades is considered individually.

3.1 Technical development of Raman and Brillouin spectroscopy

After the first observation of the Raman effect in 1928 [3], it took until 1953 before the first Raman spectrometers were commercially available [19]. They incorporated gratings as dispersive element. However, the big breakthrough did not come until the 1960s with the invention of lasers, which facilitated the monochromatic excitation [19]. Further technical development steps were the use of a charged coupled device (CCD) instead of a photographic film and the combination of Raman spectrometers with confocal microscopes [19]. Moreover, the resolving power of the spectrometers was improved by using double and triple monochromators [20]. However, over all the years, Raman spectrometers were always based on optical gratings.

The development of Brillouin spectrometers was far more challenging due to the high requirements mentioned in Section 2.2. Therefore, the instrumental setup of a Brillouin spectrometer is still the subject of current research [16, 21, 22]. First

3 History and state of the art

Brillouin spectrometers from the 1960s were based on FPIs [23]. In order to achieve sufficient extinction, the Fabry-Pérot etalon was passed twice and more [24,25]. The scanning through the FSR was performed either by varying the refractive index via the pressure or by changing the distance between the mirroring faces using a piezo element [25]. This allowed the sequential acquisition of Brillouin spectra. Further improvement was achieved by using tandem-FPIs. Their usage eliminates the ambiguity resulting from overlapping orders [25]. Piezoelectrically driven multi-pass tandem-FPIs of the so-called Sandercock type (cf. Fig. 3.1) [26,27] became the standard for Brillouin spectrometers [28]. Only in 2007, Scarcelli and Yun introduced a revolutionary approach allowing for a simultaneous acquisition of the whole Brillouin spectrum [1]. This became possible due to the usage of VIPAs, which had already been known from the wavelength demultiplexing in the telecommunication sector [18]. The simultaneous acquisition of a whole spectrum at one shot decreased the measuring time from minutes and hours down to a fraction of a second [28]. This finally brought the breakthrough for Brillouin microscopy in biomedical research, where long acquisition times are unacceptable due to photodamage.

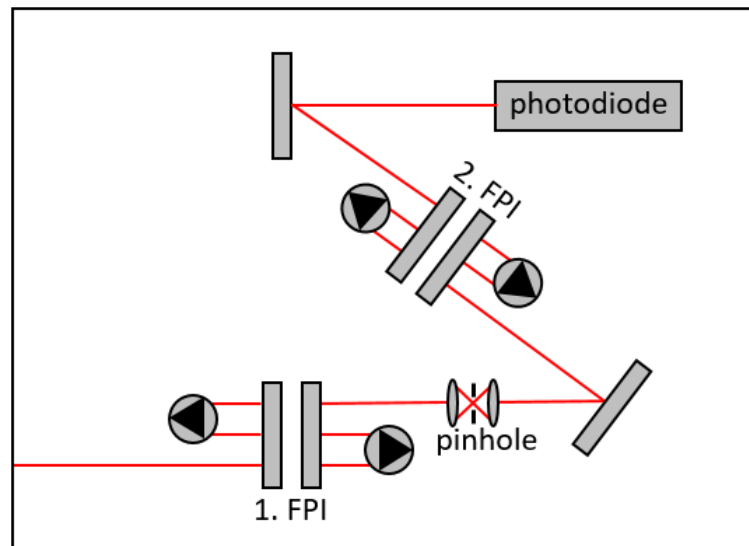


Figure 3.1: Scheme of a Brillouin spectrometer based on a 3 + 3 tandem-FPI traditionally used for the sequential acquisition of Brillouin spectra. Scheme is adapted from [29].

3.1 Technical development of Raman and Brillouin spectroscopy

While the first VIPA-based Brillouin spectrometers were equipped with only one VIPA [1, 30], the current state of the art are two-stage VIPA setups, where two cascading VIPAs are placed in cross-axis configuration (cf. Fig. 3.2) [31]. This substantially increased the extinction from 30 *dB* to 55 *dB* [21]. Further extinction to 80 *dB* is possible by adding another VIPA stage [21]. However, this comes along with an optical throughput decrease, wherefore always a trade-off between extinction and throughput efficiency has to be found [21]. For biological samples, the compromise is to use a two-stage VIPA configuration [32].

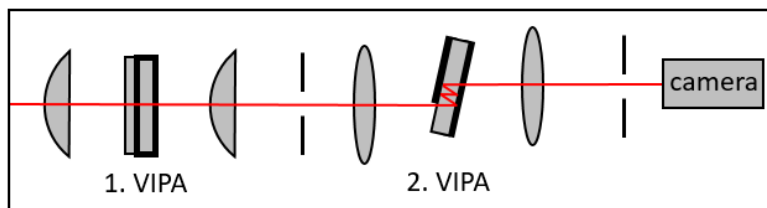


Figure 3.2: Scheme of a two-stage VIPA-based spectrometer allowing time-efficient simultaneous Brillouin spectrum acquisition. Scheme is adapted from [32].

VIPA-based Brillouin spectrometers are constantly being further improved. For example, Berghaus et al. showed in a proof-of-concept application that using two VIPAs with different dispersion power, i.e. they have a different FSR, greatly decreases the white-light background in a two-stage spectrometer [33]. Moreover, the usage of an apodization filter behind a VIPA is reported to increase the spectral contrast as well [34, 35]. A spatial light modulator is used to generate a Gaussian output field, resulting in a more efficient interference. Another approach to increase the spectral contrast is presented by Edrei et al., who inserted a Lyot stop into a two-stage spectrometer [28]. The usage of a Lyot stop, typically used in coronagraphs for exosolar planet imaging, yields in 20 *dB* further extinction coming along with minimal efficiency loss. Furthermore, Zhang et al. presented a line-scanning approach, by which a whole line is illuminated at once and the 90°-scattered light is coupled into a single-stage VIPA spectrometer [36]. This approach significantly speeds up the acquisition of maps, but is limited to special applications, where a sufficient side-illumination is possible. Finally, Fiore and Scarcelli demonstrated a

3 History and state of the art

two-stage VIPA setup consisting of only a single VIPA etalon [37]. In their setup, the output of the VIPA was coupled into the same VIPA again, just rotated by 90° in order to use the extinction advantage of a cross-axis configuration.

Besides these spectrometer-based approaches, which are by far most commonly used in current research, there are also other approaches to measure acoustic phonons. In 1986, Thomsen et al. presented a time-resolved technique, which they called ‘picosecond interferometry’ [38]. Based on this work, Lejman et al. built a pump-probe experiment, which will be presented in the following, as it exhibits several advantages compared to traditional spectrometer-based Brillouin experiments [39].

The idea of this time-resolved technique is to stay in the time-domain, rather than using a spectrometer to generate a frequency spectrum in the Fourier-domain. This allows to circumvent the typical broadening of a spectrometer, wherefore not only the frequency of acoustic phonons, but also their lifetime, can be measured very accurately. The main principle of this technique is to take advantage of the fact that an acoustic wave changes the optical properties of a sample in a time- and location-dependent manner. In more detail, the reflectivity slightly changes with the oscillations of an acoustic wave. Thus, a time-dependent measurement of the reflectivity can be used to obtain information about the acoustic phonons.

In the time-domain setup (cf. Fig. 3.3), first, light of a pulsed femtosecond laser is divided by a beam splitter into two beams. One of them is used as pump beam and the other as probe beam. For their application, Lejman et al. halve the pump beam wavelength by a second harmonic crystal to excite the sample above its band gap to efficiently generate acoustic phonons. Alternatively, they deposit a thin thermoelastic layer on the sample, which also generates acoustic phonons when exciting below the band gap. After generation, these phonons travel through the sample. The light of the probe beam is on one hand reflected at the wave front of this wave and on the other hand at the surface of the sample. These two parts constructively or destructively interfere with each other depending on the traveled distance, thus generating an oscillating reflectivity signal. The intensity of this reflectivity signal is detected by a balance photodiode subtracting a reference intensity of the probe beam. As the changes of the reflectivity signal

3.1 Technical development of Raman and Brillouin spectroscopy

are small (relative change of about 10^{-5}), the pump beam is modulated in time by an electro-optic modulator to increase the signal-to-noise ratio in combination with a lock-in amplifier.

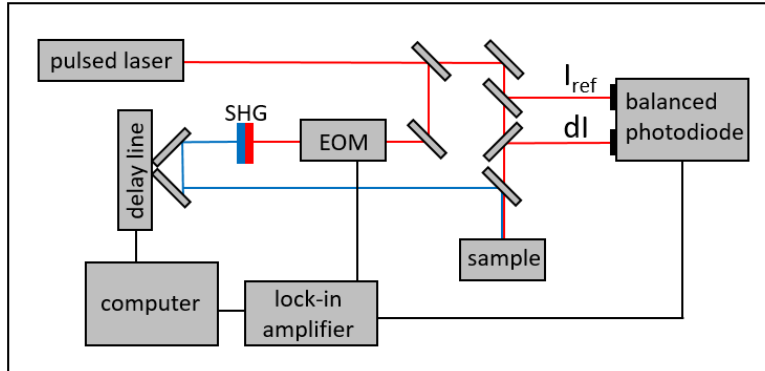


Figure 3.3: Scheme of a time-domain Brillouin spectrometer realized as a pump-probe experiment. Scheme is adapted from [39].

For achieving a high temporal resolution (hundreds of femtoseconds sampling), the signal is not detected at once, but recorded sequentially. By changing the optical path length between the pump and the probe beam using a delay line, the time difference between the two pulses can be varied. Thus, the whole reflectivity signal can be probed in very small time steps by using several similar pump events. The final frequency spectrum is obtained by fast Fourier transformation of the time-resolved signal.

Although this technique might be limited to special samples being transparent and resilient against high energy pulses, it clearly shows the advantage of a time-domain approach by circumventing the spectrometer broadening. Another underrepresented method is based on the physical principle of beating [40–42]. Thereby, the heterodyning of the Brillouin scattered light with a probe light beam, which has almost the same frequency, results in a beating signal. The lower frequency of the beating signal can be detected by state-of-the-art measuring technology. Although the metrological principle is simple and frequency resolutions up to 1 kHz can be achieved, the experimental implementation and effort limits the application of such systems.

The low probability of an inelastic scattering event is an intrinsic problem of both Raman and Brillouin scattering. This results in acquisition times, which prevent for example high resolution imaging or video-rate acquisition. To circumvent this issue being inherent in all spontaneous scattering techniques, stimulated methods are introduced, i.e. stimulated Raman scattering [43] and stimulated Brillouin scattering [44–46]. They use a strong pump laser for excitation of the sample and a probe laser, whose wavelength exactly matches the Stoke transition, so that a coupling path between the ground state and the vibrational state is established. In contrast to the spontaneous techniques, the wavelength of the probe laser is scanned over the respective frequency range and the gain of the Stokes laser light is measured in order to generate a spectrum. This allows for very time-efficient measurements, however, needs a highly wavelength-stable tunable laser [47]. A special type of stimulated Brillouin scattering is the so-called ‘impulsive stimulated Brillouin scattering’, which uses an impulsive generation of a transient acoustic wave by electrostriction and thermal coupling [47, 48]. For Raman spectroscopy, another multi-photon technique is frequently used to speed up acquisition time, i.e. coherent anti-Stokes Raman scattering (CARS) [49, 50]. Here, the mixing of three photons is used to generate anti-Stokes photons. A similar approach for Brillouin spectroscopy has not yet been reported in literature.

3.2 Combined Brillouin-Raman systems

The combination of Brillouin and Raman spectroscopy in one system allows the simultaneous and co-localized retrieval of mechanical and chemical information. Starting in 2014, several combined systems are reported in literature, which were used for diverse research.

Palombo et al. reported a FPI-based system working with 532 *nm* excitation in order to *ex vivo* investigate human epithelial tissue from Barrett’s oesophagus [51]. Sub-micrometer raster-scanning revealed variations in the measured stiffness of glandular

3.2 Combined Brillouin-Raman systems

and fibrillar regions, which could be correlated to the chemical composition. Further research demonstrated that a principle component analysis of the Raman spectra allows to identify those chemical components, which mainly trigger the Brillouin shift [52]. Moreover, non-negative matrix factorization was applied to Brillouin maps of amyloid-beta plaques from Alzheimer diseased mouse brains in order to disentangle hyperspectral information [53]. It revealed that the core of such a plaque is stiffer than the periphery. In another study of Fioretto et al., spectral moment analysis was applied to correlate the cysteine Raman band of a wool fiber to the observed Brillouin shift [54].

In a proof-of-principle paper, Scarponi et al. showed that combined systems working with 532 *nm* excitation and a multi-pass tandem-FPI allow widespread application from measurements of single cells and biofilms to investigations of curing processes in epoxy-based resin [29]. Furthermore, using the same system, Mattana et al. and Cardinali et al. performed investigations of single fibroblast cells and bone tissue, indicating that spectral analysis is often complicated due to the presence of several components within the measuring volume [55–58]. Moreover, Mercatelli et al. conducted a correlative study together with second harmonic generation on corneal lamellae showing that subtle variations in the collage supramolecular structure result in alterations of the corneal mechanical behavior.

Caponi et al. used the same system to investigate basic metrological questions, i.e. what determines the spatial resolution of Brillouin imaging and is the resolution the same as for Raman scattering [14, 59]. They observed that the mean free path of acoustic phonons can play a major role and hamper the spatial resolution. In contrast, Raman scattering is not affected by this issue, since the optical phonons are non-propagating as introduced in the theory chapter. Another basic study was conducted by Bailey et al. highlighting that, after appropriate calibration, the Raman data can be used to predict the refractive index, which has a substantial impact on the Brillouin shift [60].

A different experimental approach was reported by the group of Yakovlev, which used a single-stage VIPA-based Brillouin spectrometer in their combined system [61]. Even though they used a 780 *nm* excitation wavelength in their proof-of-principle paper, further research on adipose tissue and red blood cells was conducted with 532 *nm* [62–64]. This opens up the question, of what excitation wavelength is most

3 History and state of the art

favorable. For biological tissue, near-infrared wavelengths enable high penetration depths and low risk of photodamage [65]. However, for both Raman and Brillouin scattering, the usage of long-wavelength excitation comes along with the drawback of a small scattering intensity, as it goes with λ^{-4} . Thus, to achieve the same signal-to-noise quality, the laser power or the acquisition time has to be increased. All in all, it is always a trade-off between these parameters, wherefore no general recommendation can be given. Moreover, this trade-off must be performed for each individual sample.

Another fundamental question is, whether the usage of a VIPA-based or multi-pass tandem-FPI-based Brillouin spectrometer is favorable in a combined system. Although the latter ones have an unprecedented spectral contrast of up to 150 *dB* [29], they suffer from the fact that the spectrum acquisition is sequential and thus more time-consuming. In combined systems, however, not only the integration time of the Brillouin spectrometer is important, but also that of the Raman spectrometer, wherefore also this question must be answered for each individual application. For reasons of completeness, it shall be stated that the Raman spectrometers in the above mentioned combined systems were commercial ones from Andor Inc., Horiba Ltd. and Renishaw plc. based on diffraction gratings.

4 Setup of the combined Brillouin-Raman system

After presenting combined Brillouin-Raman systems from the literature in the previous chapter, this chapter describes the experimental setup used in this thesis. Thereby, the theoretical considerations of section 2 are used to explain the need and functionality of the respective optical components.

The experimental setup of the Brillouin-Raman system is sketched in Figure 4.1. It serves as an overview and is gradually explained in the course of this chapter by going along the beam path from one component to the next.

It should be mentioned that parts of the system were set up during my master thesis with the title “Set-up and test of a Brillouin spectrometer for biomedical applications”. Therefore, there might be overlapping information to the master thesis, especially in this chapter when describing the Brillouin spectrometer.

4.1 Laser

A continuous wave diode laser (TApro, TOPTICA Photonics AG, Gräfelfing, Germany) served as light source for the experiments. It consists of two parts; a laser diode head, where the initial lasing process takes place, and a tapered amplifier, where the laser power is increased up to 4 W. Typically, the amplification was

4 Setup of the combined Brillouin-Raman system

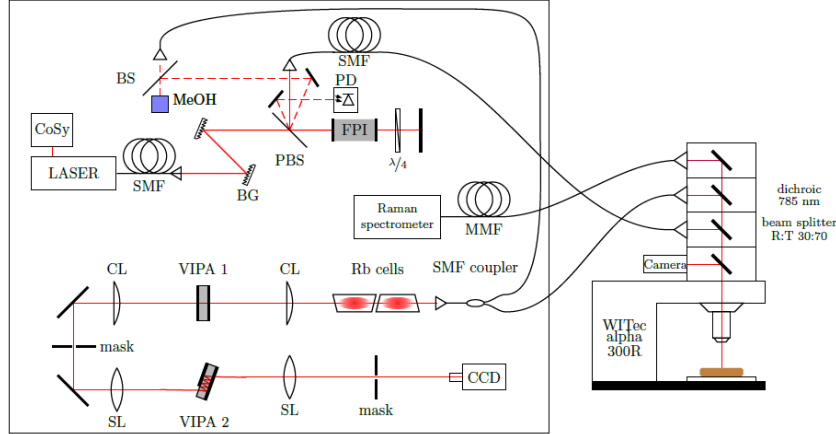


Figure 4.1: Scheme of the experimental setup consisting of an excitation unit, a microscope and two spectrometers. CoSy: Compact saturation spectroscopy, SMF/MMF: single/multi mode fiber, PBS: polarizing beam splitter, FPI: Fabry-Pérot interferometer, PD: photodiode, BS: beam splitter, CL/SL: cylindrical/spherical lens, VIPA: virtually imaged phased array, CCD: charged coupled device

set to a level so that the laser power on the sample was about 25 mW . The laser emission wavelength is located in the near-infrared spectral region and can be tuned in the range from 765 nm to 795 nm . A coarse tune can be done by manually rotating a grating mounted in a Littrow setup of the external cavity diode laser. In this work, it was adjusted to amplify a central wavelength of 780 nm . A fine tuning can be performed by changing the diode laser current. At the same time, a piezo actuator slightly changes the external resonator length to ensure a wide mode hop-free tuning range. This feed forward voltage, the piezo actuator offset voltage and the diode temperature can be set in the menu of the laser controller (DLCpro, TOPTICA Photonics AG, Gräfelfing, Germany) and have to be considered as highly interrelated parameters, which means that a change of one parameter often entails changes in the other parameters. Typical mode hop-free tuning ranges are 20 GHz wide. A mode hop-free operation is important to guarantee stable and high-precision excitation. To ensure high frequency stability, which is required for Brillouin spectroscopy (as mentioned in section 2.2), the laser is locked to an electronic transition of rubidium at 780.24 nm . Details on the frequency locking are described in the next section. The emission wavelength is at the short-wavelength

edge of the near-infrared, so that it is still visible without any additional equipment. However, the human eyes are insensitive in this spectral range, wherefore the actual power can hardly be assessed, which is important to keep in mind because of laser safety reasons.

After the seeding laser, which is limited to small laser powers, a tapered amplifier is placed. It simply amplifies all incoming photons. Ideally, these are only photons generated during the lasing process. However, besides this desired type of photons, there are also few photons originating from spontaneous emission. They are amplified, too, and form a broad background in the emission spectrum, since they have no defined wavelength. Typical ratios between the laser intensity peak and the amplified spontaneous emission (ASE) background are 40 *dB*. As mentioned above, this is not high enough to perform Brillouin spectroscopy on turbid media, wherefore further contrast increase is necessary. On the other hand, the laser already meets the condition that its emission linewidth is very sharp (50 *kHz*), which is much less than typical Brillouin shifts and Brillouin linewidths.

To ensure single wavelength excitation, the mode profile of the laser has to be considered. Unfortunately, the output of the tapered amplifier does not correspond to a Gaussian beam, but looks like a TEM₃₀ one, where one of the central spots has most intensity. In order to generate a Gaussian beam, a single mode fiber is placed at the laser aperture operating as transversal mode filter. Moreover, several longitudinal modes lay inside the gain profile of the laser. Even though mainly one mode is amplified, the intensity of neighboring longitudinal modes is still strong enough so that they can hamper the Brillouin spectrum. This becomes apparent when calculating the frequency spacing between neighboring longitudinal modes, i.e. $\Delta\nu = \frac{c}{2L}$, where c is the speed of light and L the laser cavity length. As the latter is in the centimeter regime, the longitudinal modes are separated by a few *GHz*. As this is exactly the same spectral range, where also the Brillouin signals appear, they would interfere with each other. Therefore, an appropriate longitudinal mode filter is needed to guarantee single wavelength excitation and an artifact-free Brillouin spectrum. In the present setup, a FPI is used for this purpose, which is described in section 4.4 in more detail.

4.2 Frequency locking

One key point highlighted in the section about the requirements on the setup is the need of a high wavelength-stable laser. This can generally be achieved by actively locking the laser to a known ultra-stable frequency reference.

In the present experimental setup, the D_2 transition of rubidium serves as absolute frequency reference. The transition energy corresponds to a wavelength of 780.24 nm and is thus well suited as reference for a near-infrared laser. In nature, the metal rubidium occurs mainly in two isotopes, with an abundance of 72.17% as ^{85}Rb and with an abundance of 27.83% as ^{87}Rb [66]. The energy levels of the two isotopes are slightly different, which can be seen in the Jablonski diagram (cf. Fig. 4.2).

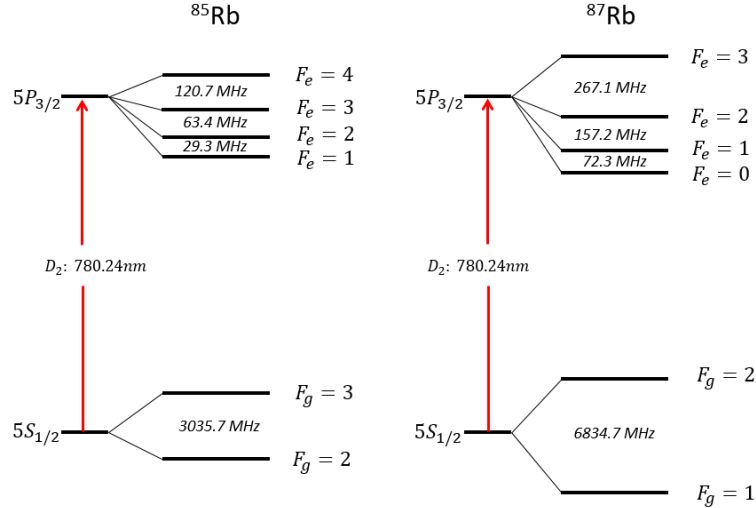


Figure 4.2: Jablonski diagram of the two naturally occurring rubidium isotopes showing slight variations in the energy differences. Scheme is adapted from [67].

The ground state $5S_{1/2}$ splits in its hyperfine structure into two levels, which are separated by about 3.0 GHz and 6.8 GHz , respectively. From each of these four energy levels a transition into the excited state $5P_{3/2}$ is possible resulting in four absorption bands (cf. Fig. 4.3). In principle, each of these bands can be used as frequency reference. However, since the ^{85}Rb $F_g = 3$ band is the strongest, a stabilization to this transition is most robust.

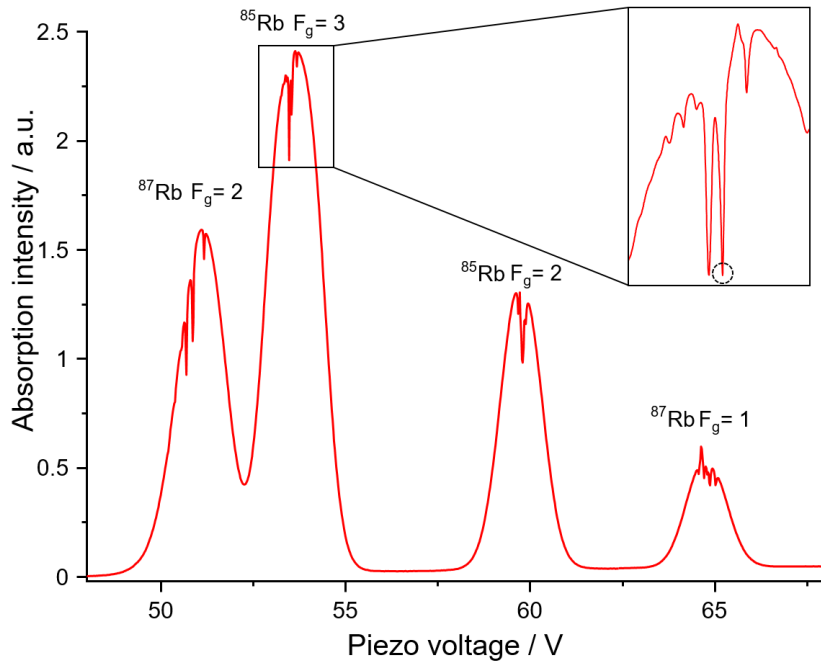


Figure 4.3: Absorption bands of rubidium corresponding to the D_2 transition, which can be used for frequency locking.

From a practical perspective, the laser frequency is periodically scanned over the relevant spectral range by changing the piezo voltage. At the same time, a probe beam from the laser is coupled via a single mode fiber to a compact saturation spectroscopy (CoSy) module (CoSy, TOPTICA Photonics AG, Gräfelfing, Germany), mainly consisting of a rubidium cell and a photodiode to detect the absorption spectrum. The absorption cell is heated to 45°C in order to transfer the atoms into gas phase allowing effective absorption. However, the rubidium atoms move with a velocity according to the Maxwell-Boltzmann distribution into all directions, when they are in gas phase. Due to the Doppler effect, this motion would result in an individual shift of the absorption frequency and would thus broaden the absorption spectrum. Since this would hamper resolving the hyperfine structure [67], which is needed for the frequency locking, a special technique is necessary to circumvent the Doppler-broadening.

This technique is provided by Doppler-free saturation spectroscopy. Hereby, the incoming laser beam is split into a pump and a probe beam (cf. Fig. 4.4). The transmitted intensity of the probe beam through the vapor cell is detected by a

4 Setup of the combined Brillouin-Raman system

photodiode. However, a transmission is only possible, when no absorption takes place. For this reason, a counter-propagating pump beam is used to transfer the atoms into the excited state. This allows the probe beam to pass the vapor cell and generate a signal on the detector. However, the transmission is only possible, when the pump and the probe beam interact with the same group of atoms. This is only the case, when the velocity of the atoms is zero or at least the velocity component in beam direction is zero. It is this condition that circumvents Doppler-broadening, because without motion, there is no Doppler frequency shift. As a result, the absorption spectrum shows so-called Lamb-dips (cf. inset of Fig. 4.3), where the laser frequency exactly matches a transition from one ground state level to one of the hyperfine levels of the excited states. The residual linewidth is limited by the lifetime of the excited state.

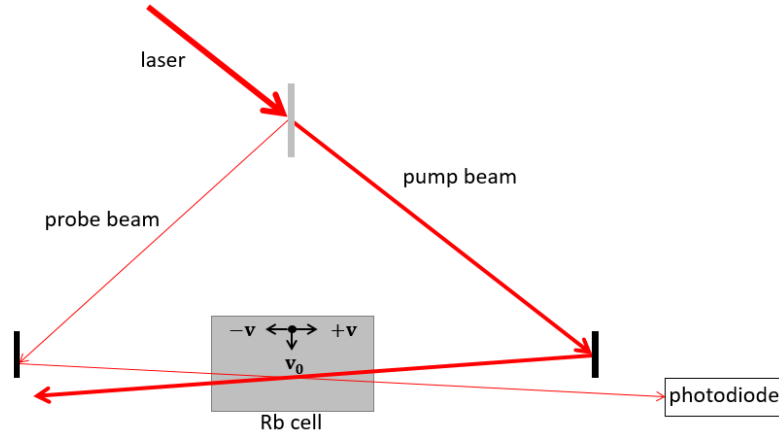


Figure 4.4: Scheme is showing the principle of Doppler-free saturation spectroscopy, where a pump beam excites rubidium atoms in the gas phase. This allows the probe beam to pass the vapor cell. Scheme is adapted from [68].

The scanning mode of the laser can be used to get an overview of the absorption spectrum allowing to select an appropriate lock point. Two lock type options are provided by the laser controller unit, which are side-of-fringe and top-of-fringe locking. While the first one can be used to stabilize the laser frequency to a slope in the absorption spectrum, the latter one is used for local extreme points. In the present work, the top-of-fringe locking was applied to the central Lamb-dip in the $F_g = 3$ transition of ^{85}Rb (cf. inset of Fig. 4.3). The laser controller generates a

small modulation of the laser current in order to generate the derivative of the absorption signal. After demodulation in the lock-in module, the zero-crossing error signal serves as input for a proportional-integral-derivative (PID) controller, which adjusts the laser current to minimize the error signal and thus stabilizes the laser frequency to the local minimum.

4.3 Bragg grating

The laser output of the single mode fiber is collimated and directed to two Bragg gratings (NoiseBlockTM, ONDAX Inc, Monrovia, United States). They further suppress the broad ASE-background and thus increase the laser peak-to-background ratio by about 10 dB each [15]. The structure and the working principle of a Bragg grating is sketched in Figure 4.5.

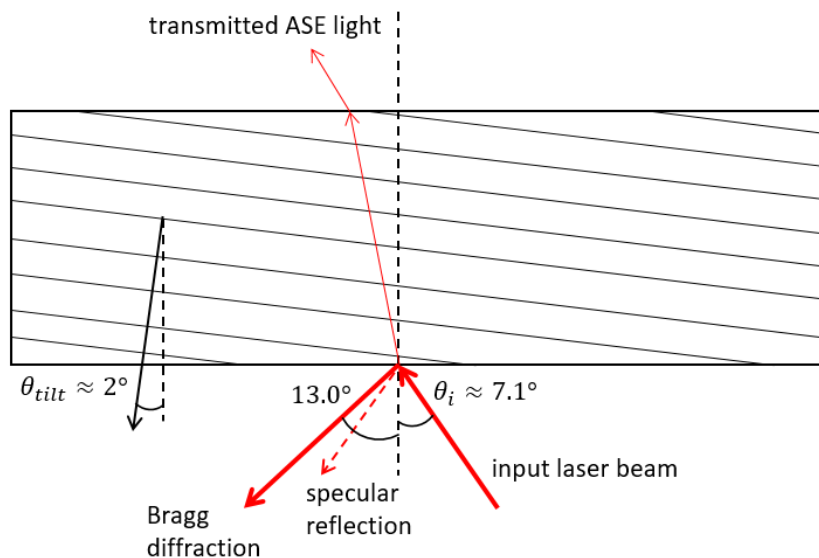


Figure 4.5: Scheme is adapted from product sheet of ONDAX NoiseBlockTM.

A volume Bragg grating consists of an alternating structure of two materials with different refractive indices. According to the Fresnel equations, a small portion of light is reflected at each interface. Because of the periodic repetition and the

4 Setup of the combined Brillouin-Raman system

constant spacing of these interfaces, Bragg's condition for constructive interference needs to be considered. It says that in first order approximation, the diffracted wavelength λ depends on the incident angle θ_i [69]:

$$\lambda = 2 d \cos(\theta_i + \theta_{tilt}) \quad (4.1)$$

where d denotes the period length of the grating and θ_{tilt} a small angle, by which the Bragg grating is rotated with respect to the surface. This should prevent that the specular reflection originating from the air-Bragg grating interface coincides with the Bragg diffracted light.

Even though a Bragg grating is a passive optical component that simply needs to be placed in the beam path, it requires a precise alignment, i.e. the correct angle of incident has to be adjusted, in order to diffract only the laser line. The ASE-background, which does not meet Eq. (4.1), shall be transmitted by the Bragg grating, which thus cleans up the laser emission spectrum. The adjustment was done by continuously measuring the diffracted light intensity with a power meter, while rotating the grating. When the intensity reached its maximum, i.e. where the wavelength of the laser line matches the Bragg condition, the Bragg grating was fixed. When mounting the second Bragg grating, care was taken that only the diffracted but not the specular reflected light from the first Bragg grating hit the aperture.

Although the Bragg gratings work as effective band pass filters, which in a first step suppress most of the ASE-background, they come along with an inherent problem: The band width of the band pass amounts to 0.12 nm (60 GHz) and is thus considerably larger than the laser peak linewidth. Therefore, the ASE-light close to the laser line is not filtered out, wherefore a more sophisticated approach is needed being presented in the next section.

4.4 Fabry-Pérot interferometer

Next in the beam path comes a FPI (Tunable Fabry-Pérot-Etalon FSR = 15 GHz, LightMachinery Inc., Nepean, Canada). On one hand, it is intended to suppress the longitudinal side modes, and on the other hand, to further suppress the ASE-background, especially that close to the laser line. A FPI is particularly suitable for both tasks, because it acts as a very narrow band pass. This becomes obvious when looking at the transmission curve, which is described by the Airy formula (see Fig. 2.8 in the theory section).

The filtering effect of the FPI can be increased by passing it twice. Therefore, a group of optical components is needed, to manage the beam guidance. At first, the linear polarized laser beam passes a polarizing beam splitter, which is oriented in such a way that most of the laser beam is transmitted. Next, the FPI is passed for the first time. Afterwards, a $\lambda/4$ waveplate converts the linear polarized light into a circular polarization. After reflection on a mirror, the beam passes the same waveplate again, whereby the circular polarization is converted back to linear polarization, but with a polarization direction that is rotated by 90° with respect to that of the beginning. Then, the beam passes the FPI for the second time. As its polarization direction is 90° -rotated, it is now reflected by the polarizing beam splitter. Finally, the beam is coupled into a single mode fiber, which delivers the light to the microscope. At this point, the laser peak-to-background ratio amounts to 90 dB and is free of any side modes. Thus, it meets the requirements for performing Brillouin spectroscopy. It should be mentioned that this laser line clean-up is not necessary for Raman spectroscopy, because the ASE-background is considerably lower in the spectral range, which is of interest for Raman spectroscopy. On the other hand, however, the clean-up has no drawbacks for performing Raman spectroscopy.

In contrast to the Bragg grating, the FPI must be actively controlled, so that it always transmits the desired wavelength, since small temperature variation already change the optical path length, wherefore a readjustment of the cavity length is necessary. For this purpose, a control loop is used, which sets the mirror spacing in such a way that the transmission is stabilized to the laser frequency.

4 Setup of the combined Brillouin-Raman system

The control variable of the feedback loop is the transmitted intensity of the FPI. Therefore, a photodiode monitors the light intensity of a ghost beam occurring at the polarizing beam splitter. The photodiode voltage is recorded by a data acquisition card and processed by a self-written LabVIEW software (National Instruments Inc., Austin, United States). The output value of the software is a piezo voltage, which is applied to the FPI in order to change the optical path length. The software has two modes, i.e. a scanning and a locking mode. In the scanning mode (cf. Fig. 4.6), the user can define a piezo voltage range, which is scanned in a predefined step size to produce an overview graph of the transmission behavior of the FPI. It shows periodically repeating transmission peaks at certain piezo voltages, which agrees with the theoretical relationship of the Airy formula. The overview graph is intended to identify lock-point candidates, i.e. a piezo voltage, where the transmission is maximal. This piezo voltage serves as initial value for the lock mode.

The lock mode fulfills the task of continuously measuring the transmitted intensity and readjust the piezo voltage in the case that the intensity is not at its optimum. As the transmitted intensity, however, decreases for both higher and lower piezo voltages, it is not straightforward to say, in which direction the piezo voltage has to be readjusted. This issue is usually solved by the so-called Pound-Drever-Hall control method [70]. A simplified version is implemented in the LabVIEW software. The key idea is to modulate the laser wavelength with a known frequency. As this is already needed for the top-of-fringe laser stabilization, the same modulation can be used here. The laser controller modulates the laser current with 20 kHz and a modulation depth of $0.5 V_{PP} \hat{=} 13.5 A_{PP}$. This modulation depth corresponds to a laser frequency variation of 11 MHz , which is smaller than the laser line and thus does not result in a significant additional broadening. The modulation signal is recorded and digitized by the data acquisition card.

The small variation of the laser wavelength results in a small variation of the transmitted intensity, which has the same modulation frequency. The digitized signals can be corrected for a phase difference to ensure that the two signals are in-phase. Additionally, the steady component of the photodiode voltage is subtracted in order to allow a signed multiplication of the two sine signals, which constitutes the

4.4 Fabry-Pérot interferometer

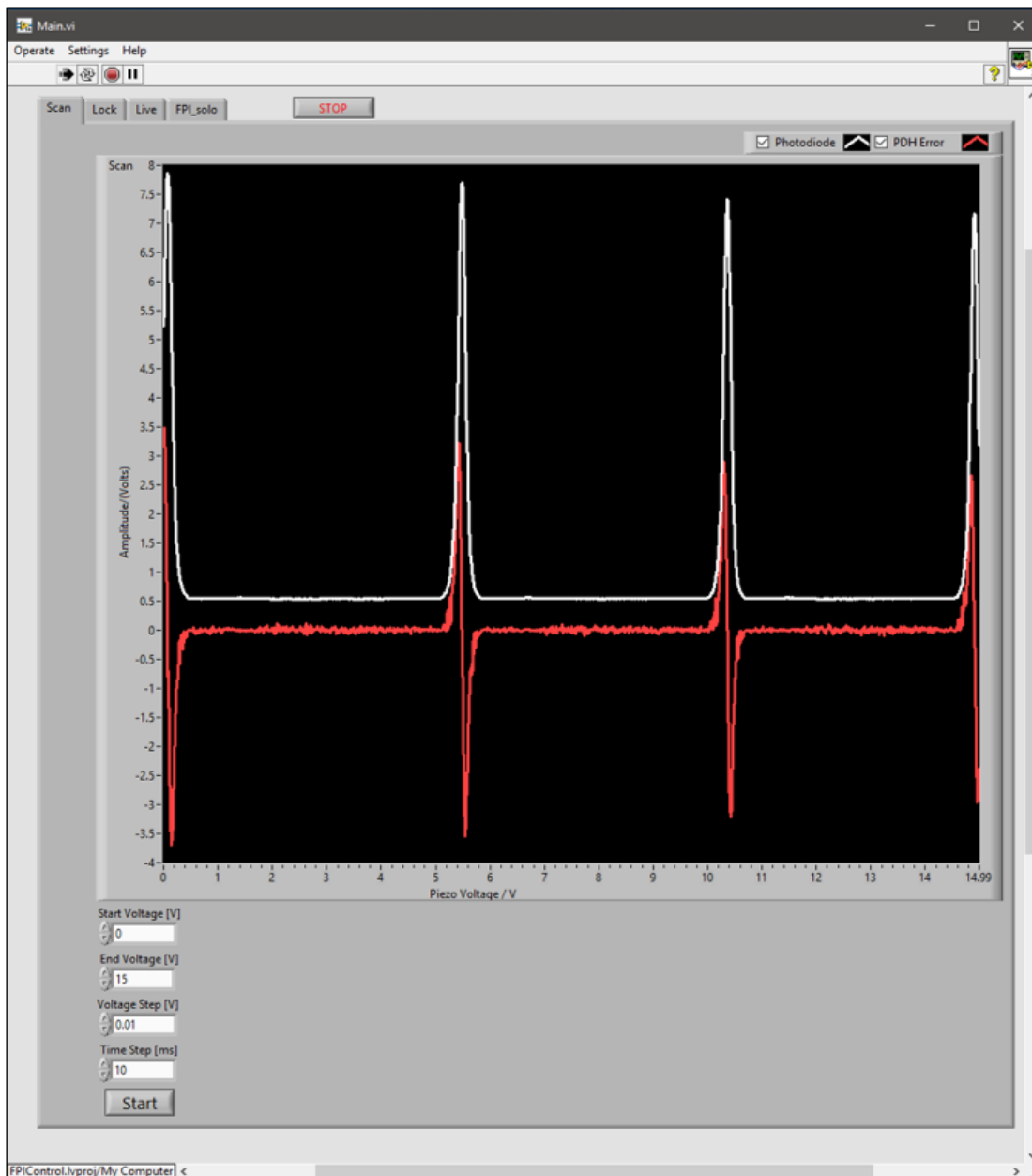


Figure 4.6: The screenshot of the LabVIEW software, which controls the FPI, shows an exemplary scan in the piezo voltage range of 0 V to 15 V where several transmission peaks are located.

4 Setup of the combined Brillouin-Raman system

error signal. The result of this multiplication is positive in the case that the signals are in-phase, or negative in the case that the signals are 180° out-of-phase. This relationship can be used to determine the direction of the piezo voltage mismatch, i.e. on the positive edge of the transmission peak the signals are in-phase, while they are out-of-phase on the negative edge. That means that for a positive error signal, the piezo voltage has to be increased and vice versa.

The readjustment rate was set to 100 Hz , i.e. every 10 ms the FPI was corrected to its maximum transmission. Therefore, the photodiode signal and the reference signal were simultaneously acquired with 1000 samples within 1.568 ms . The mean error signal in this time interval served as input for the controller to either increase or decrease the piezo voltage by 0.001 V , which corresponds to 2.7 MHz . After the lock mode is started, the piezo voltage is automatically set via this control algorithm. Within two seconds, the local maximum transmission is found and then stabilized.

A very crucial but cumbersome point during the setup of the system is the exact adjustment of the FPI. The laser beam has to enter the FPI exactly perpendicular to its entrance plane, because otherwise side band and additional peaks occur in the transmission spectrum. Therefore, the FPI is mounted with two tilt degrees of freedom. In an iterative way, both screws have to be marginally turned as long as the transmission spectrum shows the sharp and equidistant peaks well-known from the Airy formula. For this purpose, after each iterative change of the alignment, a new transmission spectrum was acquired. After final alignment, the laser beam was coupled into a single mode fiber transferring the cleaned up light to the microscope. The alignment of the fiber coupler is another crucial point, since a small misalignment already results in huge power losses. Therefore, its alignment should be done after the FPI is finally aligned, because otherwise each small tilting of the FPI entails a new adjustment of the fiber coupler from the very beginning.

4.5 Microscope

The single mode fiber is coupled to a confocal microscope (WITec alpha 300R, WITec GmbH, Ulm, Germany). Inside the microscope (cf. Fig. 4.7), a laser line filter suppresses the Raman signals generated by the fiber itself. Afterwards, a $\lambda/4$ wave plate can in principle be used to change the polarization state of the incident light from linear polarization to circular or elliptic polarization. In the present work, however, the linear polarization state, where the electric field vector is in the horizontal plane, was maintained.

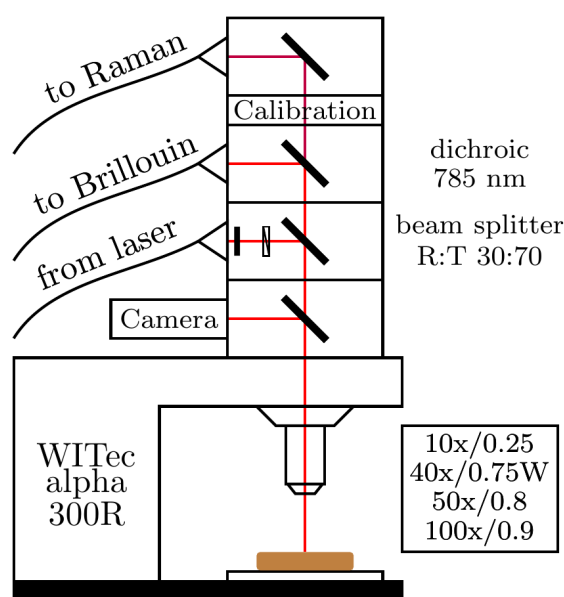


Figure 4.7: Scheme of the modular WITec alpha 300R microscope, which has been configured to allow simultaneous and co-localized Raman and Brillouin spectroscopy.

A neutral beam splitter reflecting 30% (and transmitting 70%) of the incoming light is used to redirect the excitation beam to the objectives. Several Zeiss objectives with different magnifications (10x, 40x, 50x, 100x) were available. A xy-translation stage allowed to navigate to any desired point on the sample. By means of sliders, additional beam splitters can be placed into the beam path, which allow for a white light illumination and a bright field imaging of the sample.

After interacting with the sample, the scattered light is collected by the same

4 Setup of the combined Brillouin-Raman system

objective lens (epi-detection) and passing the neutral beam splitter. Afterwards, there is a long-pass dichroic mirror with a cut-on wavelength of 785 nm . It is used to separate the Raman scattered light (Stokes-shifted by more than 5 nm corresponding to 78 cm^{-1}) from the Brillouin and Rayleigh scattered light. In the Raman beam path, an edge filter, which cuts at a Raman shift of 117 cm^{-1} , suppresses any misdirected Rayleigh and Brillouin scattered light. Then, both light beams are coupled into fibers directing the light to the respective spectrometers. For calibration purposes, a Ar/Hg lamp can be slid into the Raman beam path, which has well-defined Raman bands.

Since the microscope is a commercial system, in general no adjustment needs to be done. The only thing, which has to be checked before each measuring day, is the correct alignment of the two output fibers. By means of fine screws, the two lateral degrees of freedom of each fiber can be corrected so that most of the scattered light from the focal point is coupled into the fiber. Since the fibers function as pinhole to ensure confocality, a precise alignment is crucial. In a first step, the signal intensities can be used to check whether both fibers collect the light from the same focal point. In a second more sophisticated step, a fine rastering over a heavy-side or Dirac-delta feature was used, to fine-adjust the overlapping in both lateral directions.

4.6 Reference beam path

In a reference beam path, which is located parallel to the microscope, the Brillouin signal of methanol is acquired. Its well-known Brillouin shift is used to calibrate the spectral axis of the Brillouin spectrum. Methanol is particularly suitable, because it has one of the strongest Brillouin signals. Moreover, the Brillouin shift is considerably different to that of water, which is crucial when investigating biological tissue. The minor drawback is that methanol is a volatile liquid, which therefore has to be stored in a cuvette with screw cap to prevent evaporation. At the same time, this ensures that no air humidity condensates into the cuvette and dilutes the pure methanol.

In the setup, the reference beam path is realized in the following way: another ghost beam from the polarizing beam splitter (cf. Fig. 4.1) is directed to the inside of the cuvette via a $10\times$ magnification objective. The scattered light is collected by the same objective and passed via a 50 : 50 beam splitter to a fiber coupler. The outgoing single mode fiber is then connected with the Brillouin output fiber of the microscope in a beam combiner and coupled into the Brillouin spectrometer. From a practical point of view, again the loss-less coupling of the scattered light into the fiber is important. Moreover, it is crucial to really focus inside the cuvette to circumvent the collection of non-shifted light at the glass-methanol surface. Although the extra beam path allows to permanently acquire a reference signal ensuring high frequency stability, this approach comes along with an efficiency drawback: The output of the beam combiner is equally partitioned into two fibers. However, only one can be used as input for the Brillouin spectrometer. Therefore, half of the Brillouin intensity gets lost.

4.7 Raman spectrometer

A multi mode fiber transmits the Raman scattered light from the microscope directly to a commercial Raman spectrometer (UHTS 400, WITec GmbH, Ulm, Germany). It is equipped with two optical gratings. One has 300 *grooves/mm* and is intended to cover a broad spectral range with a resolution of 3 cm^{-1} . The other grating has 1200 *grooves/mm* and allows to acquire a high resolution spectrum with 0.5 cm^{-1} resolution. The appropriate grating can be selected via the control software (WITec Suite FIVE, WITec GmbH, Ulm, Germany), which effectively rotates the grating turret. For detection, 20 rows of a CCD camera (Andor iDUS 401A-BR-DD-352, Andor Technology Ltd, Belfast, Northern Ireland) are used to convert the spectral intensity distribution into an electronic signal, which is then captured by the control software.

4.8 Rubidium absorption cells

Before the Brillouin scattered light enters the Brillouin spectrometer, the Rayleigh scattered light has to be suppressed. Otherwise, the intense Rayleigh band would overwhelm the Brillouin signals. In order to meet this requirement (cf. Section 2.2), an ultra-narrow band notch filter is needed, which spectrally cuts only the Rayleigh band, but not the Brillouin signals several GHz adjacent to it. This issue is solved by vapor absorption cells, which use the strong and sharp absorption of one specific wavelength, which corresponds to an electronic transition. Since the laser frequency is stabilized to a rubidium transition, which thus determines the Rayleigh frequency, the same electronic transition can be used for filtering the Rayleigh scattered light. Hence, two more rubidium cells (Rubidium Vapor Cell TG-ABRB-Q, Precision Glassblowing Inc, Englewood, United States) having a diameter of 19 mm and a path length of 7.5 cm are placed in a row in the setup. They are heated up to $50^\circ C$ to transfer enough rubidium atoms from the solid to the gas phase (rubidium's melting point is at $38.9^\circ C$).

In contrast to the rubidium cell used in the CoSy module, here only one rubidium isotope is encapsulated in the cell, which is ^{85}Rb . This is crucial, because otherwise the ^{87}Rb atoms would cause additional absorption in the spectral range of interest. Despite the isotopic purity, there are the two absorption bands of ^{85}Rb being about 3 GHz apart from each other. Since the laser frequency is locked to the $F_g = 3$ absorption band, the $F_g = 2$ absorption band might suppress Brillouin signals on the anti-Stokes side of the spectrum. Fortunately, most samples have a Brillouin shift higher than 3 GHz , wherefore this additional absorption can be ignored.

From a practical point of view, the electronic rubidium cell heaters have to be turned on about 15 minutes in advance of a measurement, so that enough rubidium is in the gas phase to ensure a strong suppression of the Rayleigh light. To accelerate the heat-up process, the cells are covered with aluminum foil. Care has to be taken that also the entrance windows are covered as far as possible, to prevent that the rubidium gas condensates there during the cool down, which would result in undesired mirroring surfaces. Instead, the center of the glass cell remained unwrapped to create a passive heat sink, where condensation takes place.

4.9 Brillouin spectrometer

After passing the rubidium cells, the remaining Brillouin scattered light enters the Brillouin spectrometer. It is based on a two-stage VIPA setup. The first stage spectrally separates the light in the vertical direction and the second stage in the horizontal direction, so that in the end the spectral axis is on a 45° -tilted axis.

First, a cylindrical lens with a focal length of 200 mm focuses the collimated beam onto the rear surface of the first VIPA. As described in the theory section (cf. chapter 2), inside the VIPA the beam is reflected back and forth. The multiple exiting beams interfere with each other. The angular-dispersed light is collimated by a second cylindrical lens with focal length 200 mm . A subsequent vertical mask can be used to select the interference order(s) of interest. Figure 4.8a shows an exemplary image of the interference pattern, when coupling laser light into the spectrometer and using only the first VIPA stage. The horizontal lines originate from the different interference orders. They are separated by exactly one FSR.

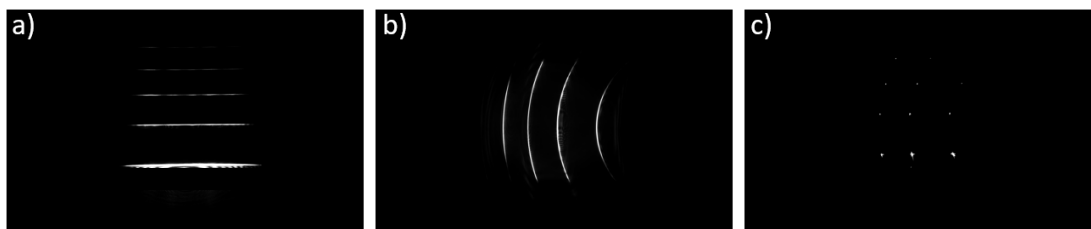


Figure 4.8: The interference pattern shows a) horizontal lines when using only the first spectrometer stage, b) vertical arches when using only the second spectrometer stage, and c) a dot pattern when using both together.

In the second stage of the spectrometer, the same principle is used as in the first stage, but now the dispersion is in the horizontal direction. Therefore, the second VIPA is rotated by 90° and instead of cylindrical lenses spherical ones are used. The occurring interference pattern for the case that only the second stage is used is depicted in Figure 4.8b. Compared to the pattern of the first stage, here, vertical arches occur due to the usage of spherical lenses.

When combining the first and the second stage, the interference pattern shows only the intersection points of the individual ones (cf. Fig. 4.8c). The dot pattern

4 Setup of the combined Brillouin-Raman system

indicates the two-dimensional frequency separation, whereby the spectral axis is now on the 45° -axis.

The setup of a two-stage VIPA-spectrometer is described in detail by Berghaus et al. [32]. The most crucial point for achieving a high-contrast interference pattern is to maximize the light coupled into each VIPA. For this purpose, the VIPAs have to be aligned in such a way that the incident beam fully enters the VIPA and after first reflection hits the high-reflective front face. On the other hand, the VIPA tilting angle has to be minimized in order to choose a preferably low interference order, where the frequencies are spatially well separated. Therefore, a perfect combination of the tilting angle and the lateral input position of the VIPA has to be found.

Another important step during the spectrometer configuration is the exact alignment of both the focusing and the collimating lenses. Their distance to the VIPA has to match the focal length as best as possible to obtain a sharp interference pattern image. At this point, the large focal lengths of 200 mm are helpful in these $4f$ -systems, since they reduce the sensitivity of small misalignments.

A special feature of the Brillouin spectrometer present in this work is the utilization of two VIPAs with different FSRs, which are $\text{FSR}_1 = 15\text{ GHz}$ and $\text{FSR}_2 = 21.6\text{ GHz}$ (OP-6721-6743-4, OP-6721-4720-4, LightMachinery Inc., Nepean, Canada). This results in a different interference pattern compared to that of a setup with equal VIPAs. While the equal FSRs show a square-like pattern (which is visible in Fig. 4.8c, when considering e.g. the four dots in the bottom-right corner), two different FSRs cause a rectangular pattern. The spectral axis, however, remains in 45° -direction. This results in the fact that it does not pass two opposite corners anymore. From another point of view, this can be understood as a separation of the Stokes and anti-Stokes spectral axis (cf. Fig. 4.9). One big advantage is that this allows to unambiguously determine the Brillouin shift, which in the case of a setup with two equal VIPAs requires prior knowledge. In the case of biological tissue with high water content, this is no issue, because the Brillouin shift will be near to that of water. For unknown or never before investigated samples, however, the ambiguity whether the signal originates from the Stokes or the anti-Stokes process is eliminated.

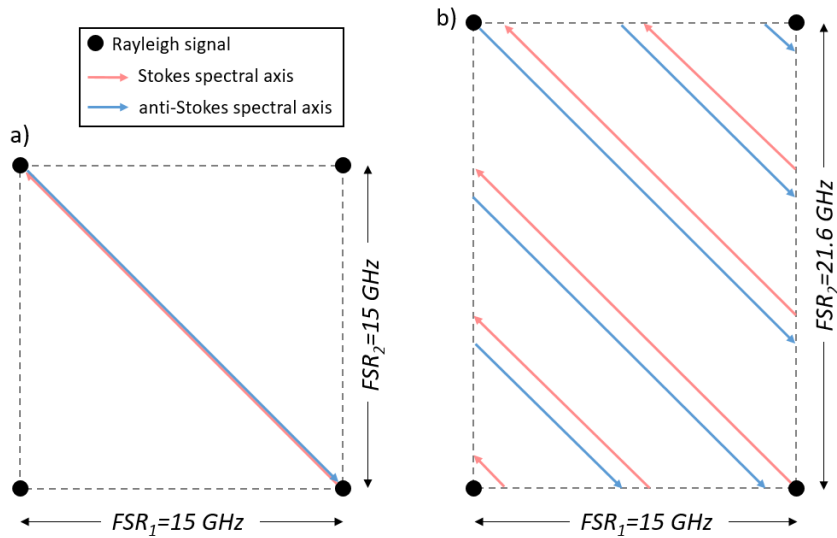


Figure 4.9: a) In the configuration with two equal FSRs, the Stokes and the anti-Stokes spectral axis coincide on the diagonal of the square-shaped interference pattern. b) Due to the different FSRs, the interference pattern gets rectangular and the Stokes and anti-Stokes spectral axis (first 45 GHz) are separated from each other.

Another advantage of the spectral axis separation is that the broad band ASE light, which in the configuration with two equal VIPAs accumulates all in the single spectral axis, is spatially distributed over all the spectral axis in the case of unequal VIPAs. This further increases the signal-to-noise ratio [33].

The usage of two VIPAs with unequal FSR results in another more subtle feature, which, however, has great impact on the analysis of the spectral signals: Since the rubidium vapor cells filter the Rayleigh light, at least a strong dip is expected in the corresponding band in the spectrum. This is indeed observable for the configuration with two unequal VIPAs. For the configuration with two equal VIPAs, however, the Rayleigh band has no central dip. The reason for this behavior is that signals from higher orders, which have a Brillouin shift that is an integer multiple of the VIPA's FSR, appear at the same spatial position. Since the FSR of the FPI in this setup is coincidentally the same as that of the two equal VIPAs, the expected dip is filled by these additional signals. As there is no guarantee that the superimposed signal is symmetric anymore, the determination of its Brillouin shift might be error-prone, wherefore this signal should not be used for calibration purposes.

4 Setup of the combined Brillouin-Raman system

Following consideration should be taken into account, when choosing the FSRs of the VIPAs: The least common multiple of the two FSRs should be as high as possible. This ensures that the spectral axes coincide only after a large spectral range. As a consequence, it would be quite ineffective, if one FSR is exactly an integer multiple of the other, because then the least common multiple matches one of the FSRs, but is not significantly higher, resulting in no separation effect. In the present setup, the FSRs of 15 GHz and 21.6 GHz have a least common multiple of 540 GHz . Since this value is much higher than the single FSRs, the spectral axis are effectively separated. From a theoretical point of view, only after 270 GHz they start to coincide again, which is much higher than typical Brillouin shifts. From a practical point of view, this value is limited by the fact that the detector is not able to resolve spectral axes from each other, which are spatially close together. However, Figure 4.9b shows that for the first 45 GHz the axes are well separated, which is still sufficient for most applications.

In a final step, the interference pattern is imaged on a CCD camera (iDUS 420A-BR-DD, Andor Technology Ltd., Belfast, Northern Ireland), which is mounted in 45° with respect to the optical table to account for the orientation of the spectral axis. For making better use of the detector area, a magnification can variably be set using an objective in front of the camera (InfiniProbe TS-160, Infinity Photo-Optical Company, Centennial, United States). It should be noted that on one hand a larger image allows to more precisely determine the Brillouin shifts, but on the other hand, it comes along with more readout noise from the camera pixels, wherefore an individual trade-off is necessary. Typical detector resolutions were between 30 MHz/pixel and 50 MHz/pixel .

To minimize any thermal noise, the spectroscopic cameras of the Brillouin spectrometer and that of the Raman spectrometer are thermoelectrically cooled to -90°C . Moreover, the two cameras are synchronized by a transistor-transistor logic (TTL)-signal, so that the WITec control unit can trigger the simultaneous acquisition of both spectra.

One characteristic value to define the spectrometer performance is the peak-to-background ratio of the laser line. For the present setup a ratio of 90 dB was measured, which is at the head of current two-stage VIPA-setups. Furthermore, the

FWHM of the laser line provides information about the spectral broadening of the spectrometer. For the current setup, a FWHM of 400 MHz was measured, which is about 8000 times larger than the laser emission linewidth. This spectrometer resolution is mainly limited by the VIPAs, where only a finite number of rays interfere with each other (finesse is about 50).

4.10 Brillouin shift axis calibration

For the generation of a Brillouin spectrum from the camera image, several rows of the detector, which encompass the spectral axis of interest, were selected. The columns of these rows were vertically binned together and its count value plotted as function of the respective pixel number. In a subsequent step, the pixel numbers had to be transformed into frequencies. In case of the Raman spectrometer, the Ar/Hg calibration lamp with its sharp and well-known emission lines can be used to automatically calibrate the spectral axis. In case of the Brillouin spectrometer the general approach of using known reference values is the same, however, there is no automated solution for this, nor is there a standard procedure. Therefore, the Brillouin shift axis calibration, i.e. the transformation from camera pixels into frequency values, is described in the following.

From a theoretical point of view, one needs to consider the imaging characteristic of the spectrometer and its dispersive element in order to decide, what kind of transformation rule is most appropriate to convert the spatial information of the camera into a frequency information. As described in the theory section by equation 2.18, the path difference of two light beams in a VIPA depends on the cosine of angle under which the beam enters/exits the VIPA. Therefore, the frequencies are not equidistantly imaged on the camera, but follow this cosine relation. In order to account for this, a parabolic function is used as transformation rule, since the first terms of a Taylor series expansion of a cosine function with small angles (which can be assumed due to the small tilting of the VIPAs) are a parabola.

Using a parabola comes along with small errors, since higher order Taylor terms are neglected. However, the big advantage of a parabola is that only three reference

4 Setup of the combined Brillouin-Raman system

points/conditions are needed to uniquely define the parabola. Taking the next Taylor term into account would already require five reference points, which are often not available in practice. Hence, typically small errors are accepted at this point.

For the present setup with two unequal VIPAs, the Brillouin shift axis calibration was done in two different ways, depending on the spectral range, where the expected signal is located. In the first case, where the Brillouin shift is less than 15 GHz , the Stokes and the anti-Stokes signal of methanol (3.81 GHz [32]) provided two reference points. For the third condition, it was exploited that Stokes and the anti-Stokes signal of the sample must have the same Brillouin shift. These three conditions could be transferred into a linear equation system to determine the coefficients of the parabola. The great advantage of this approach is that the Rayleigh signal is not required, which is especially in greater measuring depths very small and would result in an error-prone calibration.

In the second case, where the expected Brillouin shift is greater than 15 GHz , first, the respective spectral axis must be identified on the camera. The intersection points of the spectral axis with the rectangle (cf. Fig. 4.9b), which correspond to an integer multiple of 15 GHz , constitute two of the three conditions. Since in this case only the Stokes or the anti-Stokes signal of the sample is measured, another condition than their equal absolute shift is needed. In the special case that the spectral axis of interest is spatially adjacent to that where the methanol signal is located on, the tail of the methanol signal can be used to geometrically determine a quasi-reference point. It would be more exact to have a reference signal on the same spectral axis like that of the sample. However, an appropriate reference material is not always existing, especially for high Brillouin shift values.

A unique feature of the present setup is the permanent co-acquisition of the methanol reference signal, which allows to calibrate each spectrum individually. The benefit of such a permanent calibration becomes apparent when considering external perturbations. The most disturbing influence has the ambient temperature. Small variations in the temperature cause changes in the optical path difference of the VIPA. They are due to the temperature dependence of the refractive index and due to the thermal expansion of the spacing material between the mirroring

surfaces. As a consequence, the interference pattern image shifts on the camera. Fortunately, both VIPAs experience almost the same temperature change, so that the spectral axis changes at least not its orientation, but stays in the 45° -direction. The shift is mainly along the spectral axis, wherefore the transformation rule from camera pixel to frequency values needs to be updated. Since the ambient temperature permanently undergoes small variations (in the range of 1 K), a permanent recalibration of the spectral axis can compensate for those external perturbations.

4.11 Lorentzian fitting procedure

For the axis calibration and the subsequent evaluation of the Brillouin shift a precise determination of the peak positions is required. For this purpose, a non-linear fitting procedure written as Matlab code (Matlab, MathWorks Inc., Natick, United States) is used, which after initial value specification automatically fits Lorentzian functions to the measured data, so that the sum of all individual functions best fits them (cf. Fig. 4.10). Lorentzian curves are used, since they approximate the damped-harmonic-oscillator characteristic of acoustic phonons. Mathematically, Lorentzian functions are represented by the following relationship:

$$I(\nu) = \frac{I_0}{1 + \left(\frac{\nu - \nu_B}{\Delta/2}\right)^2} \quad (4.2)$$

where I_0 is the peak maximum at center frequency ν_B and Δ is the FWHM.

One Lorentzian curve was used for each Stokes and anti-Stokes signal. Although the remaining shoulders of the Rayleigh band do not underlie the characteristic of an acoustic phonon, they show a similar line shape, wherefore they were fitted with Lorentzian functions, too.

From a practical point of view, first a set of initial parameters, i.e. where the peaks are roughly located, is handed over to a Matlab function together with boundaries between which the solutions should be determined. Here, especially the exclusion

4 Setup of the combined Brillouin-Raman system

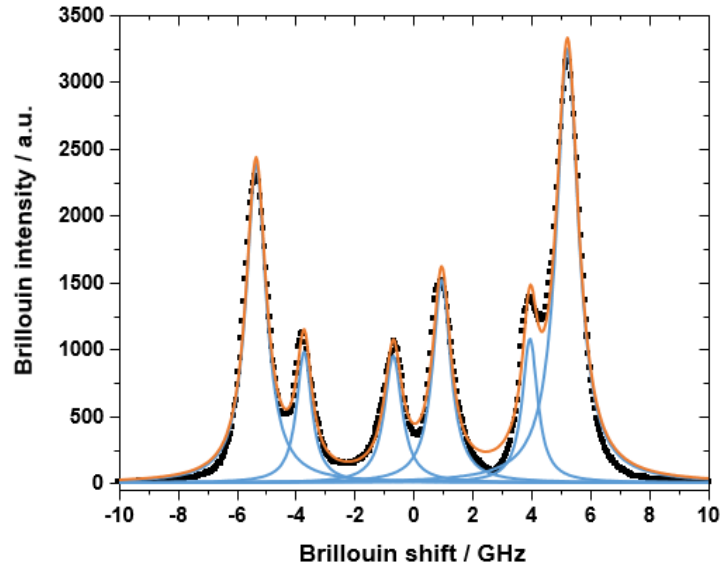


Figure 4.10: Exemplary fitting of six Lorentzian functions (blue) to the measured Brillouin spectrum (black dots). A nonlinear iterative fitting algorithm finds the best match of the sum (orange) of all functions to the measured data points.

of negative peak heights is important. Afterwards, a non-linear solver based on Matlab's *lsqnonlin* function iteratively changes the peak position, peak height and peak width of each function in order to minimize the overall least-square error. The stop criterion is met when either 3000 iterations times the number of fitted curves are performed or the least-square error is less than 10^{-6} . The best-fit values are provided as output for further data analysis. This fitting procedure is especially then powerful, when the peak height is considerably higher than the background noise and when the peaks are not overlapping too much.

5 Applications

The Brillouin-Raman system was utilized for two different applications, which are presented in this chapter. In a first application, the solid state physics of domain walls in periodically-poled lithium niobate was investigated. The second application dealt with the oncological properties of brain tumor cells.

5.1 Domain walls in lithium niobate

5.1.1 Introduction

Lithium niobate (LiNbO_3) is a crystalline solid, which has widespread applications due to its exceptional properties, which are originating from the unique crystal structure. For example, it is commonly used in frequency doublers due to its great non-linear constants [71]. Moreover, it is applied in integrated optics [72] and surface acoustic wave generators [73] as well as in mechanical and piezoelectric devices [74]. Due to its high Curie temperature of 1140 K , LiNbO_3 shows ferroelectric behavior also at temperatures much higher than room temperature [75]. Ferroelectricity describes the phenomenon that a material possesses a spontaneous electric polarization, which in the case of LiNbO_3 amounts to $5 \mu\text{C}/\text{cm}^2$ [76].

The direction of the spontaneous polarization is along the optical z axis and can be inverted by applying an electric field. Areas within which the polarization direction is the same are called domains. By means of poling, an almost arbitrary

5 Applications

pattern of domains can be written into the crystals. This is typically exploited in periodically-poled ferroelectrics in order to create structures, which allow for quasi-phase matching [77].

Recently, the domain walls, i.e. the interface between two neighboring domains, attracted interest, because they show properties, which are different than those of the bulk domains due to its two-dimensionality. For example, the domain walls in LiNbO_3 show electric conductivity in the order of $0.02 (\Omega \text{ cm})^{-1}$, whereas the bulk material behaves like an insulator [78, 79]. On one hand, this opens up novel applications for example in micro-electronic and opto-electronic. On the other hand, a deeper understanding and characterization of the underlying physics of the domain walls is needed to be able to tune specific parameters and make maximal use of these outstanding properties.

5.1.2 State of the science

The crystalline structure with its strict symmetry makes vibrational spectroscopy a predestined tool for investigations of LiNbO_3 . In a few studies, Brillouin spectroscopy was used to determine the temperature dependence and the effect of stoichiometry on the elastic constants of the bulk LiNbO_3 [80–82]. However, no investigations of domain walls by Brillouin spectroscopy are present so far. In contrast, Raman spectroscopy was used in a wide range of studies for investigating both bulk domains and domain walls. The main results and accompanying theory will be presented in the following.

The crystal structure of LiNbO_3 , which is the archetype of a lot of ferroelectric materials, was first investigated by Abrahams et al. by x-ray diffraction [83]. They found that LiNbO_3 crystallizes in a trigonal structure, which belongs to the space group $R3c$. One primitive unit cell contains two formula units, i.e. two lithium, two niobium and six oxygen atoms. The crystal structure is depicted in Figure 5.1 showing that the lithium and niobium atoms are laying on the crystallographic c -axis (which is the principle axis of the crystal) and the oxygen atoms form tilted octahedrons around them.

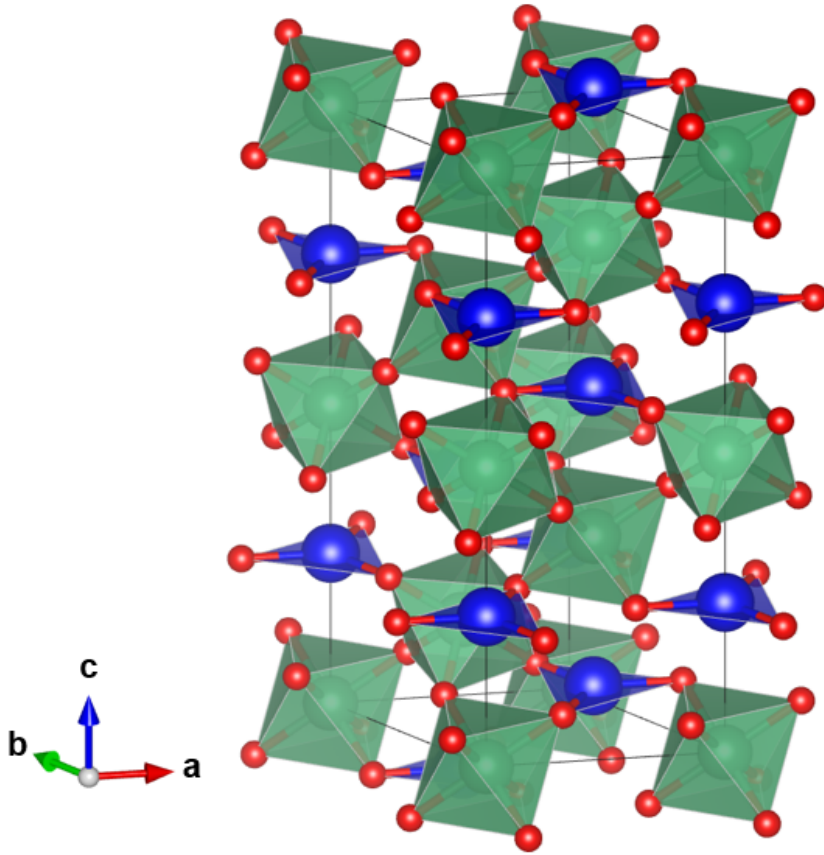


Figure 5.1: Crystal structure of a conventional unit cell, where the lithium atoms (blue) and the niobium atoms (green) are laying on the c-axis coinciding with the direction of spontaneous polarization, whereas the oxygen atoms (red) are off-axis and forming octahedrons. Scheme was created with VESTA [84].

Group theory is a powerful tool for predicting the number and characters of phonon modes in crystalline materials. It is commonly used for interpreting the Raman spectra of LiNbO₃. The only a priori knowledge, which is needed for conducting the group theoretical considerations, is the point group of LiNbO₃ and how the crystal structure behaves when carrying out the symmetry operations of the corresponding character table [85]. For LiNbO₃, which belongs to the point group C_{3v} , group theory predicts 27 optical and 3 acoustic phonon modes at the Brillouin zone center [86]. They split into $\Gamma_{opt.} = 4A_1 + 5A_2 + 9E$ and $\Gamma_{acou.} = A_1 + E$, where

5 Applications

A and E are so-called Mulliken symbols indicating non- and twofold-degeneracy, respectively. While the A_1 and E modes are Raman, Brillouin and infrared active, i.e. the polarizability and the dipole moment change during the vibration, the A_2 modes are silent meaning that they cannot be observed in the experiment.

The Raman modes can further be divided into transversal optic (TO) and longitudinal optic (LO) ones (cf. Fig. 2.5 in the theory section). It depends on the actual measuring geometry what kind of symmetry species are observable. These selection rules are summarized in Table 5.1 for the backscattering configurations along the three main crystal axes. The measuring geometry thereby is defined in Porto notation $k_i(e_i, e_s)k_s$, where k_i and k_s denote the direction of the incident and scattered light, respectively, and e_i and e_s its polarization direction with respect to the crystal axis [87].

Table 5.1: The selection rules of the optical phonon modes in LiNbO₃ indicate that depending on the measuring geometry only distinct symmetry species are observable [88].

measuring geometry	allowed phonon mode	tensor elements
$x(y, y)\bar{x}$	$A_1(\text{TO}) + E(\text{TO})$	$a^2 + c^2$
$x(y, z)\bar{x}$	$E(\text{TO})$	d^2
$x(z, z)\bar{x}$	$A_1(\text{TO})$	b^2
$y(x, x)\bar{y}$	$A_1(\text{TO}) + E(\text{LO})$	$a^2 + c^2$
$y(x, z)\bar{y}$	$E(\text{TO})$	d^2
$y(z, z)\bar{y}$	$A_1(\text{TO})$	b^2
$z(x, x)\bar{z}$	$A_1(\text{LO}) + E(\text{TO})$	$a^2 + c^2$
$z(x, y)\bar{z}$	$E(\text{TO})$	c^2
$z(y, y)\bar{z}$	$A_1(\text{LO}) + E(\text{TO})$	$a^2 + c^2$

Each of the irreducible representations of the point group C_{3v} has a corresponding Raman tensor R , which can be used in the Raman tensor formalism to calculate the contribution of the different phonon modes to the Raman spectrum according to the following relationship [89]:

$$I \propto |e_s R e_i|^2 \quad (5.1)$$

For LiNbO₃, the following three 3×3 matrices reflect the symmetry of the crystal, whereby the non-negative tensor elements, which are addressed by the particular

measuring geometry, are listed in the last column of Table 5.1 [90]:

$$A_1(z) = \begin{pmatrix} a & 0 & 0 \\ 0 & a & 0 \\ 0 & 0 & b \end{pmatrix} \quad E(x) = \begin{pmatrix} 0 & c & d \\ c & 0 & 0 \\ d & 0 & 0 \end{pmatrix} \quad E(y) = \begin{pmatrix} c & 0 & 0 \\ 0 & c & d \\ 0 & d & 0 \end{pmatrix} \quad (5.2)$$

Experimentally, several Raman studies were performed (e.g. [85, 91, 92]), where almost all of the predicted phonon modes were observed and assigned to the respective symmetry species. The assignment was possible due to polarization-dependent measurements, where the above outlined selection rules were exploited, i.e. that the presence of the different phonon modes highly depends on the measuring geometry. All in all, the bulk domains are well characterized.

In contrast, the domain walls were sparsely investigated by Raman spectroscopy. However, there are few studies from Fontana et al. [93] as well as Stone and Dierolf [94] on this topic. They both observed changes in the Raman spectrum when investigating a domain wall instead of a bulk domain. However, they developed different theories to explain these spectral changes. Rüsing et al. [88] discussed both theories in a broader context and found that neither theory is able to explain all observed changes. In the following, the two theories will be explained in detail, since they build the basis of the interpretation of the results in the present work. The theory of Stone and Dierolf [94] is based on the assumption that domain walls act like extended planar defects and generate a quasi-momentum perpendicular to the plane. This additional momentum has a direct impact on the selection rules. Due to momentum conservation, the bulk selection rules are relaxed, wherefore the domain wall Raman spectrum consists of additional bands, which are not allowed in bulk domains.

Figure 5.2 shows the two different situations. In a bulk domain (situation (a)), the wave vectors of the incident and the scattered light point into 180° opposite directions, which is predefined by the measuring geometry. The difference between them is attributed to the investigated phonon wave vector. At the domain wall (situation (b)), the additional quasi-momentum q_{DW} causes the difference wave vector to change (now it is not on the same axis like the light wave vectors, but

5 Applications

tilted to them due to the transverse momentum), which means that other phonons are subject of investigation. It is noteworthy that the measuring geometry is in both cases the same, but the selection rules are changed due to the intrinsic defect. In the particular case, which is shown in Figure 5.2, the incident/scattered light goes along the z -axis but the phonon wave vector is laying in the xz -plane. Therefore, not only contributions of the z -direction but also of the x -direction are allowed. The exact proportion of the two contributions depends on the strength of the transverse momentum. The angle α between the phonon wave vector and the photon propagation direction can be used as a measure for this mixing. In the case of $\alpha = 0$, the additional quasi-momentum is negligible, whereas α increases with increasing q_{DW} . Generally, such a mixed behavior is known from directional dispersion.

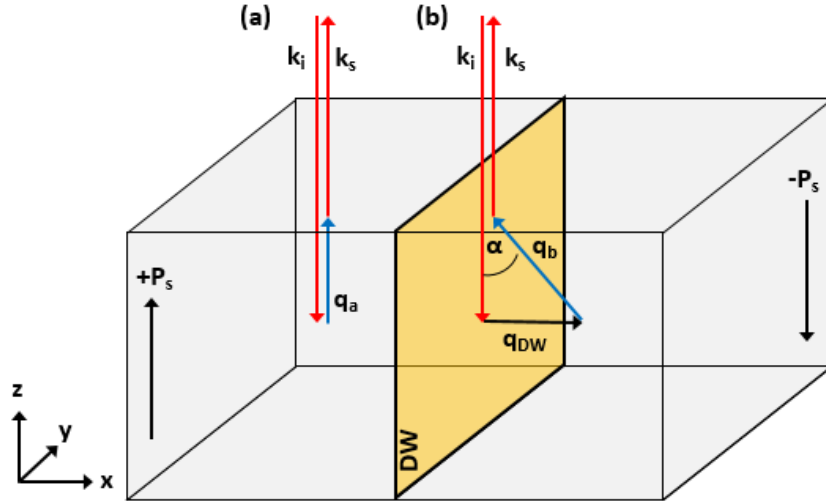


Figure 5.2: The momentum conservation is sketched for a scattering event happening (a) in a bulk domain and (b) at a domain wall (DW). In the latter case, an additional momentum of the domain wall results in an inclination of the investigated phonon wavevector. Scheme is adapted from [88].

Fontana et al. [93] developed another model to explain the changes in the Raman spectrum at the domain wall. It is based on the findings that local strain and electric fields are present in the vicinity of a domain wall [95, 96]. This is not surprising, since the direction of the spontaneous electric polarization is changing

by 180° within a few unit cells, resulting in distortions of the crystal structure. Domain walls can be classified into Ising, Bloch and Néel type (cf. Fig. 5.3), depending on how the spontaneous polarization vector changes its direction at the domain wall. It is assumed that the domain walls in LiNbO_3 are not of pure Ising type, but have a mixed Ising-Bloch-Néel character [97], which strengthens the assumption that additional strain and electric fields are present at the domain wall.

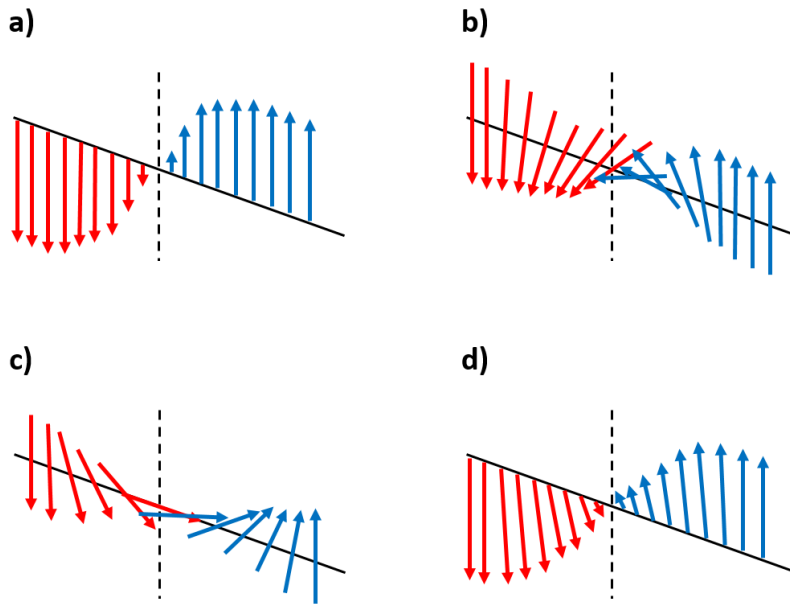


Figure 5.3: The different types of domain walls vary depending on how the spontaneous polarization vector behaves at the domain wall: a) Ising b) Bloch c) Néel d) mixed Ising-Néel. Scheme is adapted from [97].

According to the theory of Fontana et al., the additional fields have an impact on the Raman scattering efficiency due to elasto-optic and electro-optic coupling [93]. In more detail, the usual polarizability change with respect to the normal coordinates is altered by the additional strain and electric fields. Since the polarizability change is proportional to the Raman scattering intensity, this theory explains the observed changes in the Raman spectrum, too.

All in all, there are already Raman studies on domain walls in LiNbO_3 , which show interesting topological results. Two different theories are given in literature to explain the differences between a bulk domain and a domain wall spectrum. The

5 Applications

open question is, how the Brillouin spectrum behaves when crossing a domain wall. Therefore, the combined Brillouin-Raman system was used to investigate the following questions: a) Is there also a change in the Brillouin spectrum at the domain wall? b) How large is the spatial dimension in which this effect can be observed? c) Can the existing theories from Raman spectroscopy be used to explain the changes in the Brillouin spectrum, too?

5.1.3 Results

To answer these questions, a periodically-poled 5 *mol%* MgO doped LiNbO₃ crystal was investigated, which was supplied by Crystal Technology Inc. (Palo Alto, United States). The typical MgO doping of LiNbO₃ results in 100 times higher resistance against optical damage [98] compared to undoped crystals. At the same time, the selection rules stay the same, since the doping does not change the crystal structure, and thus there are only minor changes in the Raman spectrum (cf. Fig. 5.4), which can be explained by broadening due to the presence of an additional atom type.

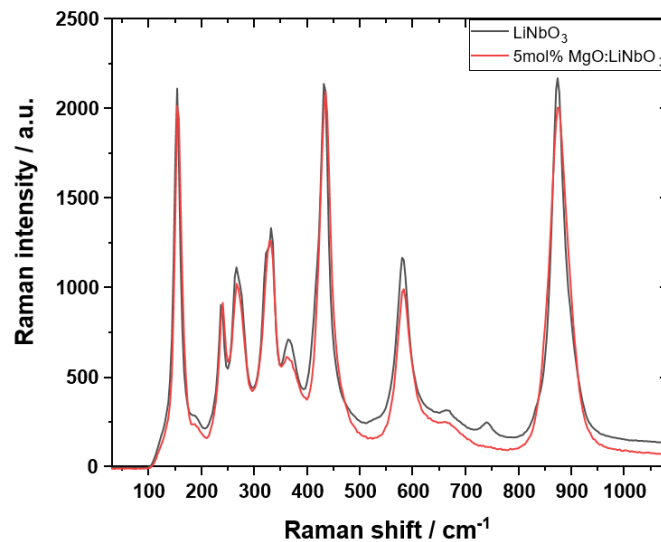


Figure 5.4: The doping of LiNbO₃ with 5 *mol%* MgO results only in small changes in the Raman spectrum, because the general crystal structure remains the same. (2 s integration time, 10 repetitions)

5.1 Domain walls in lithium niobate

The period length of the domains in the crystal amounted to $6.9 \mu\text{m}$. The polarization direction of the alternating domains was perpendicular to the large surface of the z-cut crystal (cf. Fig. 5.5), i.e. the surface normal coincided with the crystallographic c-axis. The domain walls between the virgin and the inverted domains were mainly located in the yz-plane. Hence, the large z-cut surface provided good access to domain walls. Furthermore, the thickness of $500 \mu\text{m}$ allowed to measure also the x-cut and the y-cut surface.

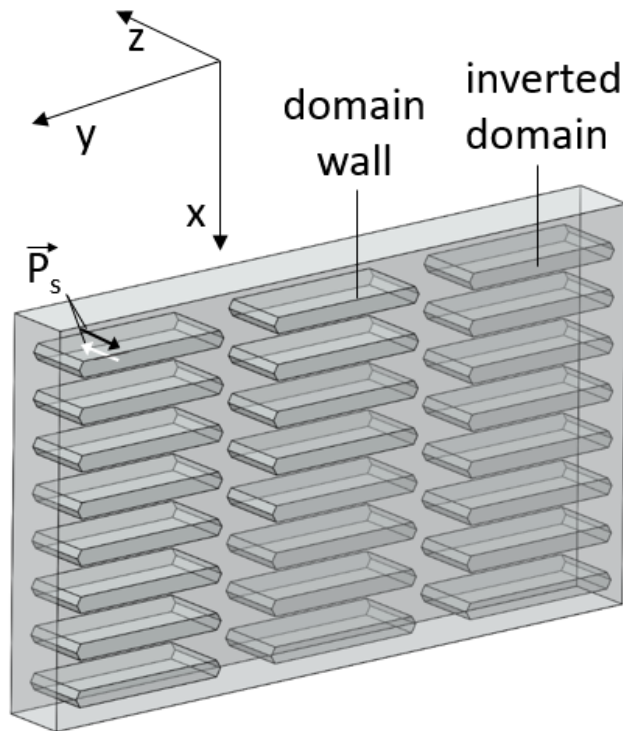


Figure 5.5: Sketch of the periodically-poled LiNbO_3 crystal possessing domain walls mainly in the yz-plane. Scheme is adapted from [99].

By means of equations 2.12 and 2.13, the Brillouin shifts in the different directions of space can roughly be estimated. Therefore, only the knowledge of the refractive index, the mass density and the longitudinal modulus, i.e. the respective element in the elastic tensor, is required as well as the excitation wavelength and the scattering geometry. While the two latter are defined by the experimental setup (780.24 nm excitation wavelength and backscattering geometry), the refractive index, the mass density and the elastic constants can be looked up in literature.

5 Applications

Since LiNbO_3 is an uniaxial birefringent crystal, there is both an ordinary refractive index n_o and an extraordinary refractive index n_e . Their wavelength dependence is described by the Sellmeier equations [100]. For 780.24 nm excitation wavelength, the refractive indices of 5 mol% $\text{MgO}:\text{LiNbO}_3$ amount to $n_o = 2.254$ and $n_e = 2.169$, whereby the ordinary refractive index is for light propagation in the xy-plane and the extraordinary refractive index along the z-axis.

In general, the elastic tensor C_{klmn} is a fourth-order tensor, which links the stress tensor σ_{kl} with the strain tensor ϵ_{mn} , resulting in 81 tensor elements. However, due to symmetry, several of them are equal, wherefore a different notation can be used, which accounts for this fact. This is provided by the Voigt notation, which uses the following rule [101]:

$$11 \mapsto 1, \quad 22 \mapsto 2, \quad 33 \mapsto 3, \quad 23 \mapsto 4, \quad 13 \mapsto 5, \quad 12 \mapsto 6 \quad (5.3)$$

whereby two Cartesian coordinates are converted into one Voigt coordinate, which hence reduces the number of indices and thus the number of tensor elements. Moreover, the trigonal structure of LiNbO_3 reduces the number of non-zero tensor elements to six, wherefore the elastic tensor has the following form (with the experimental values retrieved from 7 mol% $\text{MgO}:\text{LiNbO}_3$) [102]:

$$C_{ij} = \begin{pmatrix} C_{11} & C_{12} & C_{13} & C_{14} & 0 & 0 \\ C_{12} & C_{11} & C_{13} & -C_{14} & 0 & 0 \\ C_{13} & C_{13} & C_{33} & 0 & 0 & 0 \\ C_{14} & -C_{14} & 0 & C_{44} & 0 & 0 \\ 0 & 0 & 0 & 0 & C_{44} & C_{14} \\ 0 & 0 & 0 & 0 & C_{14} & \frac{1}{2}(C_{11} - C_{12}) \end{pmatrix} = \begin{pmatrix} C_{11} \\ C_{12} \\ C_{13} \\ C_{14} \\ C_{33} \\ C_{44} \end{pmatrix} = \begin{pmatrix} 205 \text{ GPa} \\ 57 \text{ GPa} \\ 74 \text{ GPa} \\ 8 \text{ GPa} \\ 240 \text{ GPa} \\ 61 \text{ GPa} \end{pmatrix} \quad (5.4)$$

The longitudinal modulus in x-direction is thus determined by the elastic coefficient C_{11} and the mass density $\rho = 4683 \text{ kg/m}^3$ [102], since both the uniaxial stress and the uniaxial strain are in x-direction. Same is valid for the y-direction, because of symmetry. In the z-direction, however, C_{33} determines the elastic properties.

A rough estimation with a refractive index of 2.2 and an elastic constant of 230 GPa results in a Brillouin shift value of about 40 GHz. This indicates that the expected

5.1 Domain walls in lithium niobate

frequency shift is larger than the FSRs of the VIPAs. As a consequence, the Brillouin signals do not appear on the spectral axes, which directly cross the corners of the rectangular interference pattern, but lay on adjacent ones, which is sketched in Figure 5.6. The roughly estimated Brillouin shift of 40 GHz allows to determine the spectral axis of interest, i.e. the spectral axis, which intersects the rectangle at 30 GHz and 43.2 GHz .

From a practical point of view, a similar interference pattern like the sketched one can be found on the Brillouin camera image. Small differences are due to the fact that the spherical lenses in the second stage of the spectrometer result in a bending of the horizontal edges of the rectangular. Nevertheless, an identification of the spectral axis of interest is possible, so that the respective camera rows for vertical binning can be selected. As mentioned in the axis calibration section, a tail of the methanol signal, which spreads out to these rows, is used to calibrate the Brillouin shift axis. A geometrical consideration provides that the methanol signal (3.81 GHz) appears at 40.29 GHz . This is the result, when subtracting 3.81 GHz from 45 GHz (vertical intersection with the rectangle) and additionally accounting for an offset of 0.9 GHz between the adjacent spectral axes.

All in all, this procedure allows to create a calibrated Brillouin spectrum of LiNbO_3 out of the camera raw image. As a first step, this was used to determine the Brillouin shifts of x-,y- and z-cut $\text{MgO}:\text{LiNbO}_3$ as well as that of a domain wall. The results are summarized in the interference pattern scheme (Fig. 5.6).

The Brillouin and Raman single point spectra of a z-cut bulk domain and a domain wall are shown in Figure 5.7. The polarization direction of the incident light was parallel to the crystal's y-axis, so that the scattering geometry in Porto notation was $z(y, u)\bar{z}$, where u indicates that no polarization filter was used in the detection channel. For all measurements on LiNbO_3 , a $50\times$ magnification objective with $NA = 0.8$ was used.

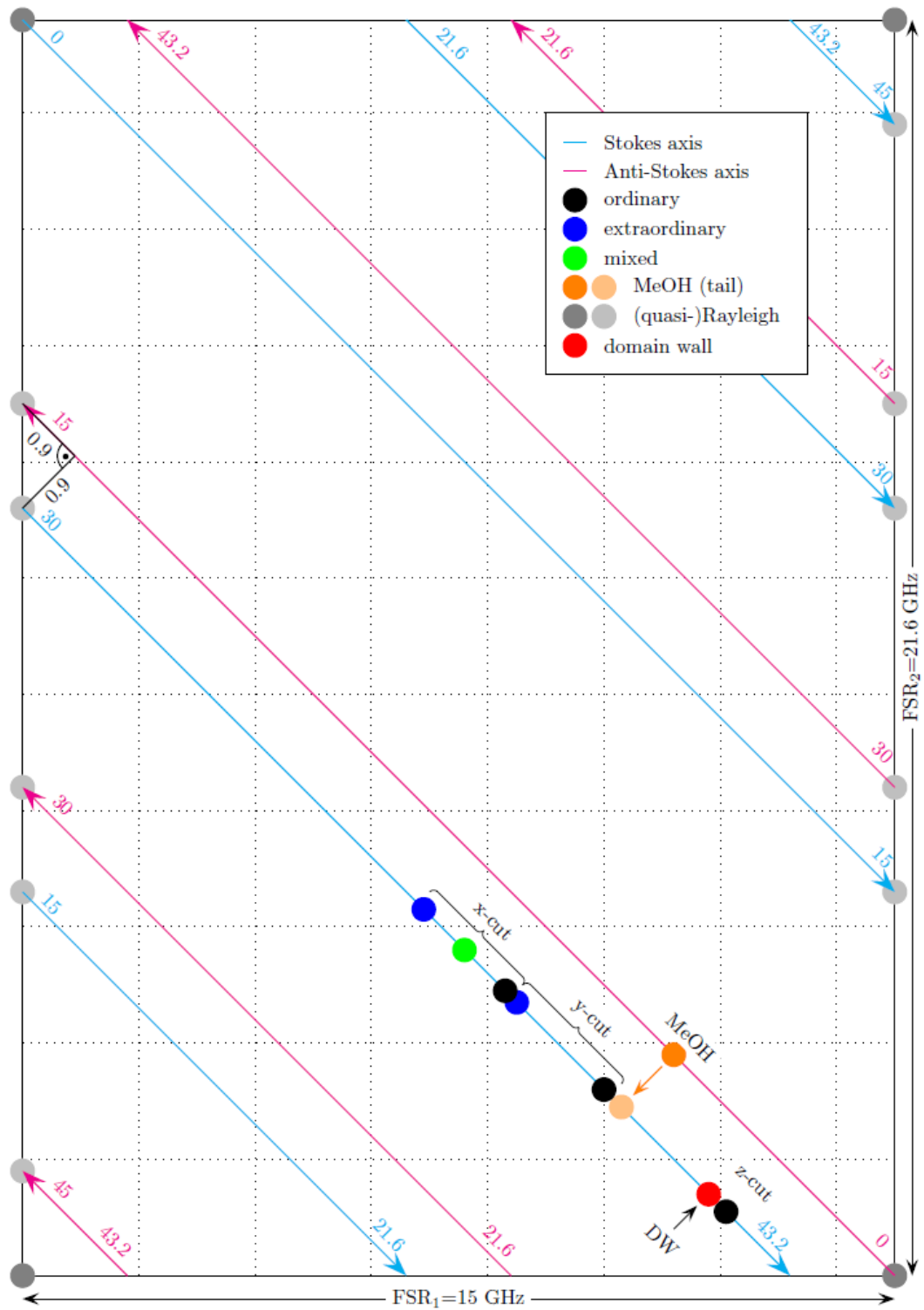


Figure 5.6: Sketch of the first-order interference pattern, in which the Brillouin signals of the different measuring geometries are marked on the selected spectral axis. Scheme is adapted from [99].

The Raman spectra of the domain wall and the bulk domain are almost identical and show several bands in the range from 100 cm^{-1} to 900 cm^{-1} , which can be assigned to $A_1(LO)$ and $E(TO)$ modes [103]. However, the domain wall spectrum has a shoulder at 635 cm^{-1} , which is not present in the bulk domain spectrum and can neither be assigned to an $A_1(LO)$ mode nor to an $E(TO)$ mode.

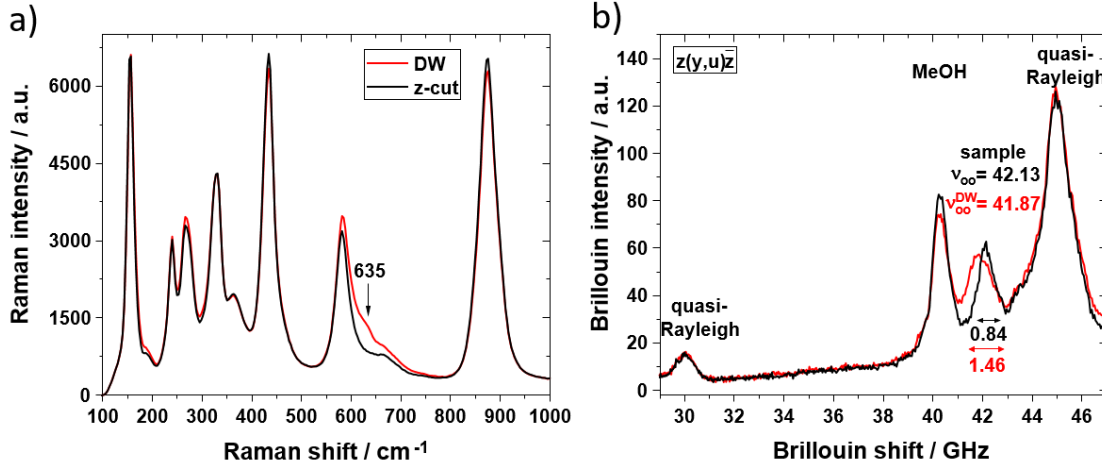


Figure 5.7: a) Raman and b) Brillouin spectra obtained from a bulk domain (black) and a domain wall (red) in z-cut geometry (5 s integration time, 20 repetitions). The main difference in the Raman spectra is at 635 cm^{-1} , where the domain wall spectrum has an additional shoulder. In the Brillouin spectra, the Brillouin band shifts towards lower frequencies when hitting a domain wall. Figure is adapted from [99].

The Brillouin spectra show quasi-Rayleigh bands at 30 GHz and 45 GHz (integer multiples of the FSR of the FPI and the first VIPA) as well as the methanol band at 40.29 GHz , which all three were used for calibration of the Brillouin shift axis. Additionally, there is the band at 42.13 GHz and 41.87 GHz in the case of the bulk domain and the domain wall of $\text{MgO}:\text{LiNbO}_3$, respectively. Its FWHM amounts to 0.84 GHz and 1.46 GHz , respectively. Hence, on one hand the Brillouin shift decreases when hitting a domain wall and on the other hand, the distribution of Brillouin shifts gets broader.

In order to find a possible explanation for these findings, also the Raman and Brillouin spectra of x-cut and y-cut $\text{MgO}:\text{LiNbO}_3$ were acquired, which are shown

5 Applications

in Figure 5.8 and 5.9. Here, the polarization direction of the incident light takes effect. Therefore, three different polarization directions were chosen to account for this, which were along the ordinary and the extraordinary direction as well as 45° in between.

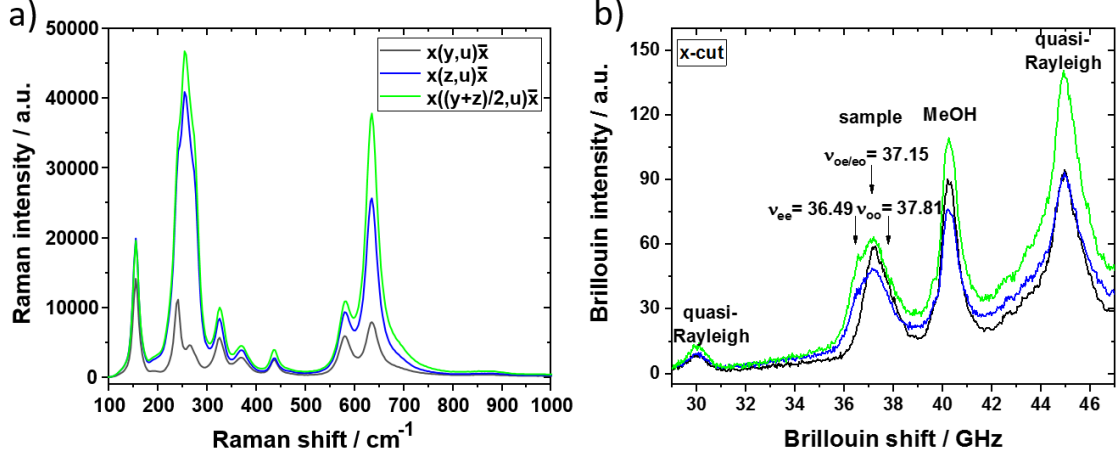


Figure 5.8: a) Raman and b) Brillouin spectra obtained from a bulk domain in x-cut geometry with different incident light polarization (5 s integration time, 20 repetitions). Figure is partly adapted from [99].

The x-cut Raman spectra show a great dependence on the incident light polarization direction affecting the intensity. This is not surprising, since different tensor elements are addressed. Incident light with ordinary polarization ($x(y, u)\bar{x}$) is sensitive to the tensor elements a , c and d , whereas light with extraordinary polarization ($x(z, u)\bar{x}$) is sensitive to b and d . Light with a polarization direction between the ordinary and extraordinary one is sensitive to all tensor elements.

The x-cut Brillouin spectra show a dependence on the incident light polarization direction, too. For ordinary incident polarization, there are two bands at 37.81 GHz and 37.15 GHz and for extraordinary incident polarization at 36.49 GHz and 37.15 GHz . The 45° polarization direction shows all three bands. According to the considerations of Lejman et al. [39], the different bands originate from the different refractive indices. The bands with the lowest and highest Brillouin shift belong to the cases, where the light is solely sensitive to the extraordinary and ordinary refractive index on the forward and backward path, respectively. In contrast, the band in the middle represents the case, where the light is incident with

one polarization direction, but scattered with a 90° -rotated polarization direction, wherefore it is sensitive to both refractive indices resulting in an average value. The ability of a change in light polarization direction at interaction with a phonon is described by Lejman et al. as mode conversion.

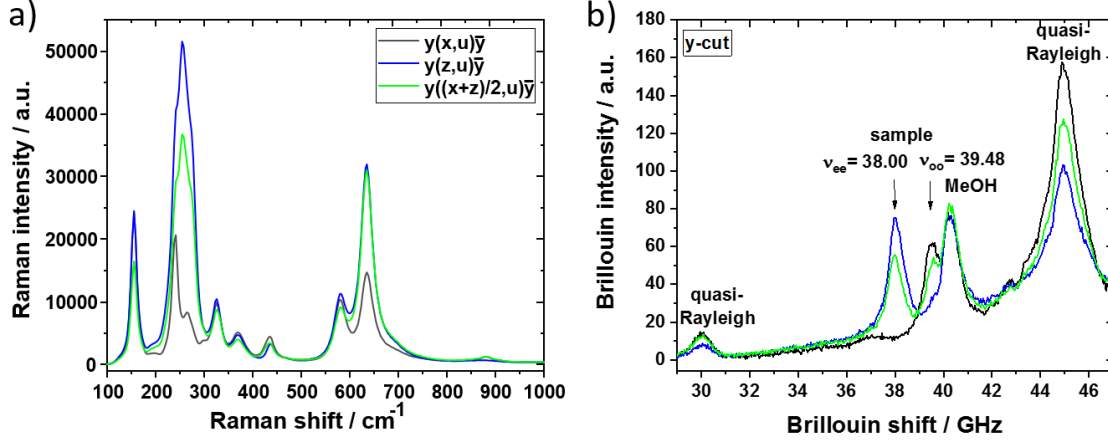


Figure 5.9: a) Raman and b) Brillouin spectra obtained from a bulk domain in y-cut geometry with different incident light polarization (5 s integration time, 20 repetitions). Figure is partly adapted from [99].

The y-cut Raman spectra (cf. Fig. 5.9) show a similar behavior like the x-cut ones. I.e., depending on the incident polarization, different tensor elements are addressed, wherefore the bands are of different intensity.

Also the Brillouin spectra show again a dependence on the incident polarization direction, i.e. bands appear at 38.00 GHz and 39.48 GHz . However, in the y-cut Brillouin spectra the mixed band is missing, which leads to the assumption that the mode conversion effect is not present in this direction or at least very weak. Lejman et al. demonstrate by means of the elasto-optical tensor that the mode conversion effect is indeed not expected in the y-cut configuration, because the corresponding tensor element is zero [39].

When comparing the Raman spectra of the z-cut domain wall (Fig. 5.7a) with that of the x-cut bulk domain (Fig. 5.8a), one observation gets apparent, which is a strong indication for the theory of Stone and Dierolf: At the spectral position

5 Applications

of 635 cm^{-1} , where the shoulder appears in the domain wall spectrum, the x-cut spectrum shows a band, which corresponds to the $A_1(TO_4)$ mode. According to the selection rules (cf. Table 5.1), $A_1(TO)$ modes are only allowed in x-cut and y-cut geometry, but not in z-cut. This gives rise to the assumption that an additional momentum changes the wavevector of the investigated phonon [88].

In a next step, the differences in the Raman and Brillouin spectra between the z-cut bulk domain and the domain wall were used to visualize the domain walls. On one hand, the Raman intensity at 635 cm^{-1} served as Raman contrast mechanism, and on the other hand, the Brillouin shift provided a Brillouin contrast mechanism. Figure 5.10 shows the results of a line scan crossing several domain walls in z-cut MgO:LiNbO₃, where the two contrast mechanisms were applied. The $20\text{ }\mu\text{m}$ traveled distance was rastered with a step size of $0.1\text{ }\mu\text{m}$, whereby at each point a Raman spectrum and a Brillouin spectrum (both with 5 s integration time and 3 repetitions) were acquired.

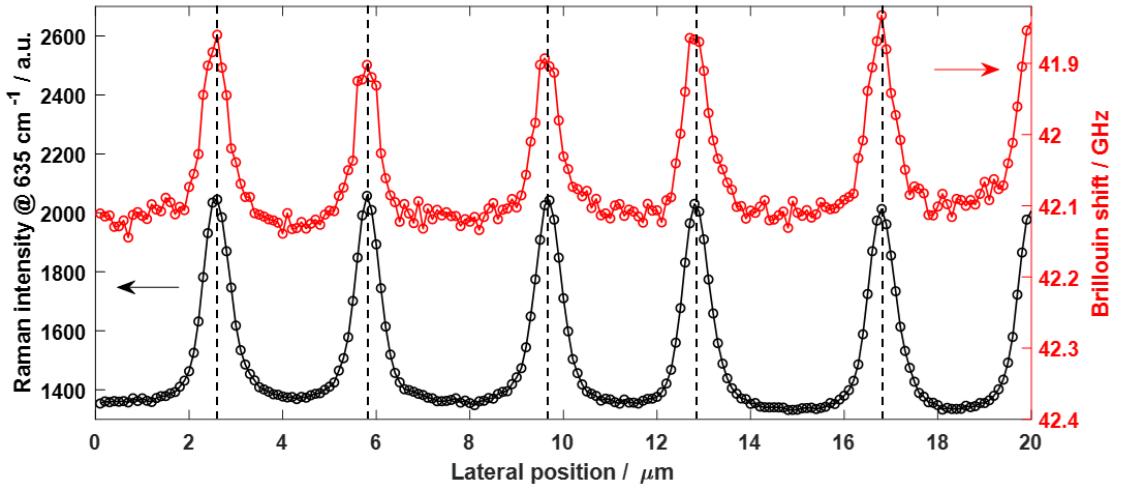


Figure 5.10: Line scan crossing several domain walls, where the Raman intensity at 635 cm^{-1} (black) and the Brillouin shift (red) were used as contrast. Figure is adapted from [99].

The line scan confirms the behavior, which was already seen in the single point spectra. I.e., at the domain wall, the Raman intensity at 635 cm^{-1} increases,

while the Brillouin shift decreases. Beyond that, the line scan provides additional information on the extent of this effect and thus the extent of the domain wall itself. Therefore, the FWHM of the domain wall signal was determined from both the Raman and the Brillouin contrast. Interestingly, in both cases it amounts to approximately 650 nm . This length matches well with the laser spot diameter. Moreover, it is noteworthy that the signal-to-noise ratio is better in the case of the Raman contrast mechanism compared to the Brillouin one. On one hand, this is due to the very strong and low-noise Raman spectra compared to noisy Brillouin spectra with weak bands. On the other hand, the different contrast mechanisms themselves are differently susceptible to errors. While the evaluation of the Raman intensity is straight forward and reliable by calculating the mean of the intensity values in the respective region, the determination of the Brillouin shift needs a Lorentzian fitting, which is more error-prone, especially in the case of a weak and noisy signal.

The Lorentzian fitting of the Brillouin band allows not only to evaluate the peak position, i.e. the Brillouin shift, but also the maximum intensity and the FWHM. Both quantities are plotted in Figure 5.11.

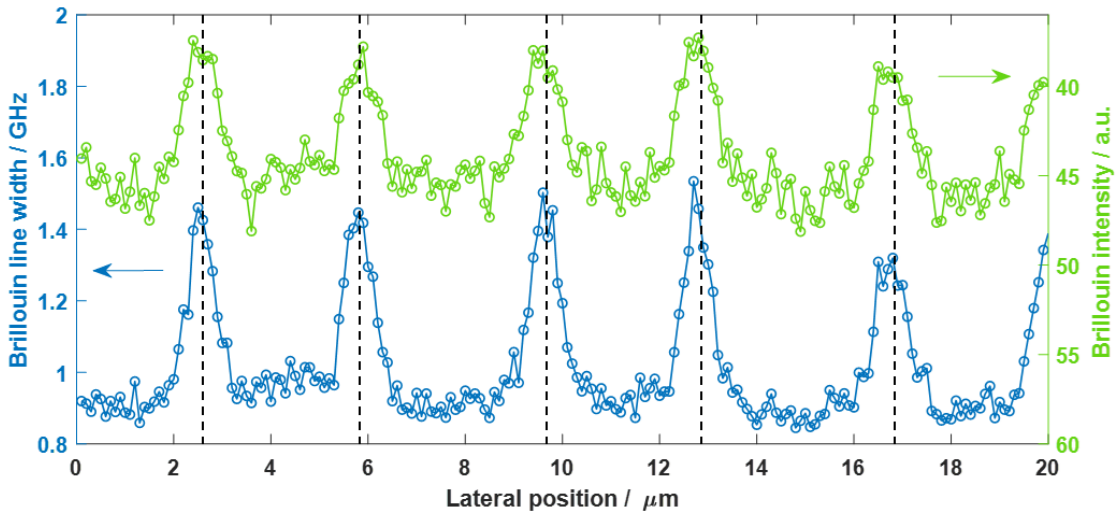


Figure 5.11: Line scan crossing several domain walls, where the Brillouin linewidth (blue) and the Brillouin intensity (green) were used as contrast. Figure is adapted from [99].

5 Applications

They show the position of the domain walls, too, at which the band intensity is lower and the FWHM increased. However, they are even more noisy than the curve of the Brillouin shift. Again, this might be an effect of the fitting procedure, which detects the central position of a peak more precisely than the width and the band height.

Finally, an area scan was performed to demonstrate that both contrast mechanisms allow for an imaging of the domain walls. Figure 5.12 shows a rectangular area ($7.5 \mu\text{m} \times 30 \mu\text{m}$) of the z-cut surface, where the domain walls lie in the horizontal direction, which is sketched in part a). The distance between the domain walls is alternately about $3 \mu\text{m}$ and $4 \mu\text{m}$. The raster step size in both directions amounted to $0.5 \mu\text{m}$.

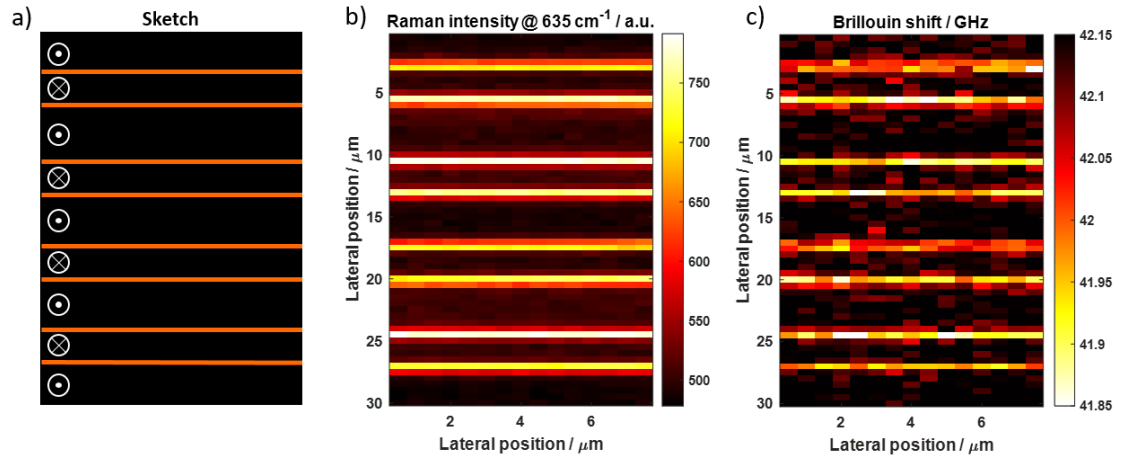


Figure 5.12: a) Sketch of an area containing several domain walls, which appear as horizontal lines. The same picture emerges, when using b) the Raman intensity at 635 cm^{-1} and c) the Brillouin shift as contrast. The alternating spontaneous polarization direction of the domains is indicated by arrow notation. Integration time was 3 s per pixel with 2 repetitions. Figure is adapted from [99].

Both the generated Raman map (Fig. 5.12b) and the Brillouin map (Fig. 5.12c) show the domain walls, whereby the strength of the contrast is color-coded. Again, the Raman map is less noisy, which can be explained in the same way as for the line scan.

Furthermore, it is noteworthy that there is only a contrast between the domain

walls and the bulk domains, but there is no difference between the virgin and inverted domains.

5.1.4 Discussion

Coming back to the initial question, whether also the Brillouin spectrum changes when hitting a domain wall, which can definitely be answered with yes. On one hand, the Brillouin shift decreases at the domain wall, and on the other hand, the Brillouin band gets broader and less intense. Besides the single point spectrum, also the line scan and the area scan showed a clear difference between the domain wall and the bulk domain. Raman spectroscopy, and especially the intensity at 635 cm^{-1} , turn out to be a reliable reference method for detecting the domain wall. The second question, how large the spatial dimension of the observed effect is, can be answered with about 650 nm . However, the question, what this implies for the dimension of the domain wall, is more sophisticated. Since the spatial extent of 650 nm matches well with the laser spot size, it can be assumed that the domain wall is only several nanometers thick and the oversampling results in a convolution effect of the laser spot size with the actual effect of the domain wall. Interestingly, both the Brillouin and the Raman contrast show the same spatial extent. This gives rise to the assumption that the origin of the two contrasts is in the same mechanism.

Therefore, the third question is, whether the Brillouin contrast can be explained by the same theories, which are already existing to explain the Raman contrast. First, the quasi-momentum theory of Stone and Dierolf [94] shall be tested. The domain wall, which is assumed as extended planar defect, generates an additional quasi-momentum perpendicular to it, wherefore the wavevector of the investigated phonon changes, which is equal to a relaxing of the selection rules.

Indeed, this is what can be observed in the Raman spectrum. The $A_1(TO_4)$ mode at 635 cm^{-1} , which is present in the x-cut measuring geometry, is normally forbidden in the z-cut measuring geometry. However, in the domain wall spectrum, it is nevertheless present. Thus, the relaxing of the strict selection rules, allows that also modes of other geometries are observable.

5 Applications

In the Brillouin domain wall spectrum, however, there is no new band showing up, but the existing band is shifted to lower frequencies. Thus, the impact of the quasi-momentum is more subtle. Nonetheless, the same mechanism is able to explain this behavior, which gets obvious, when looking again at the momentum conservation scheme (cf. Fig. 5.2). The additional momentum of the domain wall results in the fact that the investigated acoustic phonon is not traveling along the z-axis anymore, but with an angle α to it. This has an impact on the Brillouin shift, since the elastic properties and thus the speed of sound are depending on the direction. For example, the speed of sound along the z-axis amounts to 7399 m/s , whereas it is only 6654 m/s along the x-axis [102]. Therefore the additional momentum, no matter how strong it is, results (according to equation 2.12) in a decreased Brillouin shift, since the speed of sound is lower in all directions different from the z-direction.

The above mentioned behavior is similar to the so-called directional dispersion known from Raman spectroscopy [104]. Therefore, the following equation for the speed of sound $v_s(\alpha)$ may be used to estimate the angle α , by which the wavevector is inclined in the x-direction with respect to the z-axis:

$$v_s(\alpha) = \sqrt{\frac{v_{s,x}^2 v_{s,z}^2}{v_{s,x}^2 \cos^2(\alpha) + v_{s,z}^2 \sin^2(\alpha)}} \quad (5.5)$$

where $v_{s,x}$ and $v_{s,z}$ are the speeds of sound in x- and z-direction, respectively. Assuming a Brillouin shift of 41.14 GHz , which is at the lower bound of the FWHM of the Brillouin band, results in an angle $\alpha = 27^\circ$. This means that the investigated acoustic phonon travels under an angle of up to 27° with respect to the z-axis.

The broadening of the domain wall Brillouin band in comparison to the bulk domain Brillouin band, may be explained by the quasi-momentum, which has not always the same strength. Therefore, the 27° inclination is an upper limit, however, all other angles between 0° and 27° are possible, too. An indicator for this behavior is that the Brillouin band is not simply shifting to lower frequencies, but broadens in this direction.

When assuming that the total number of participating photons is almost the same in case of the domain wall and the bulk domain spectrum, the area under the curve

has to be the same. This is what can actually be observed in the line scan, as the peak height compensates the broadening in case of the domain wall Brillouin band. So far, only the speed of sound was considered, when investigating a domain wall. However, also the refractive index has an impact on the Brillouin shift and Golde et al. [105] recently showed that there is a refractive index increase at the domain wall, which would lead to higher Brillouin shifts. However, this refractive index increase is assumed to be only in the order of 10^{-3} to 10^{-4} , wherefore the effect of the speed of sound clearly dominates.

The theory of Fontana et al. [93] is explaining the changes of the Raman spectrum at the domain wall by strain and electrical fields, which result in a changed polarizability. When looking for an explanation for the changes in the Brillouin spectrum, it is known that additional electric (and because of the piezoelectricity of LiNbO_3 also strain) fields lead to a change in the elastic properties [106]. The implication of additional fields on the speed of sound can be calculated by using the Christoffel equation. However, for this purpose, an exact knowledge of the fields present at the domain walls is necessary. Without this knowledge, at this point, it can only be said that it is possible that the additional fields may result in a lower Brillouin shift. And the fields will highly depend on the type of the domain wall. While Ising type domain walls have a vanishing polarization at the domain wall due to the sign change, the Bloch and the Néel type domain walls show an out-of-plane and an in-plane polarization vector rotation, respectively. Since it is assumed that often mixed domain wall types are present [97], a prediction of the fields is even more complex.

5.1.5 Outlook

The discussion has shown that both theories known from Raman spectroscopy, i.e. the quasi-momentum theory of Stone and Dierolf and the local field theory of Fontana et al., are principally also able to explain the observations in the Brillouin spectrum of the domain wall. For a complete validation of both theories, further

5 Applications

measurements should be conducted. This section is intended to provide an outlook on possible further measurements.

First of all, the effect of external electric fields on the Brillouin shift should be clarified in order to be able to evaluate the theory of Fontana et al. in more detail. Therefore, Brillouin measurements should be performed in analogy to previously conducted Raman measurements [107], where liquid electrodes on a LiNbO_3 crystal allowed to measure in-situ the implications of an external electric field.

Moreover, the present work was limited to domain walls in the yz -plane, which were only accessible in z -direction. In future studies, it would be interesting to investigate domain walls from the x - and the y - direction as well. One experimental obstacle might be that in those measuring geometries the two different refractive indices come into effect. Since the Brillouin bands now are already strongly overlapping in x -cut geometry, it might be impossible to detect the domain wall Brillouin band(s) with the current setup. One possible solution for this issue would be to use a time-domain spectrometer like that of Lejman et al. [39]. In comparison to VIPA-based spectrometers, the spectra suffer not so much from spectrometer broadening, wherefore an overlapping of the Brillouin bands can be prevented.

Another way to address this issue would be to use a rotatable polarization filter in the detection channel. This would provide the ability to detect only light with a desired polarization direction, which would reduce the number of observable Brillouin bands.

Beyond that, a fully polarization dependent setup would yield the opportunity to perform measurements individually in all possible geometries listed in Table 5.1. Therefore, not a set but single tensor elements can be addressed individually. This would allow for a direct correlation between theory and experiment.

A series of fundamental questions comes along with such considerations. a) Is there in analogy to the Raman tensor formalism a similar way for Brillouin spectroscopy to take advantage of the crystal symmetry? b) Are there also Brillouin tensors similar to the Raman tensors? c) If yes, to what extent do theory and experiment yield the same results? Although it is not the aim of this thesis to completely

5.1 Domain walls in lithium niobate

answer these questions, a first insight into this topic shall be given in the following in order to motivate further measurements.

According to classical mechanics, one can state the following equation of motion to describe the dynamics of acoustic waves [108, 109]

$$\rho \ddot{u}_k = C_{klmn} \frac{\partial^2 u_n}{\partial r_l \partial r_m} \quad (5.6)$$

where u_k and u_n are components of the local displacement vector, C_{klmn} the elastic constants and r_l and r_m spatial components. This second order partial differential equation can be solved by a plane wave ansatz of the common form $u_k = u_k^0 e^{i(\mathbf{q} \cdot \mathbf{r} - \omega t)}$, where \mathbf{q} denotes the wavevector of the acoustic wave. The arising eigenvalue problem

$$|C_{klmn} \hat{q}_l \hat{q}_m - \rho v_s^2 \delta_{mn}| = 0 \quad (5.7)$$

can be solved for one given wavevector, whereby $\hat{q}_m = \frac{q_m}{|q|}$ is the directional cosine between \mathbf{q} and the m -axis. This results in three modes (eigenvalues), which are of pure longitudinal or transverse character only for distinct \mathbf{q} , but generally of mixed character. The corresponding displacement eigenvectors give exact information whether it is (quasi-)longitudinal or (quasi-)transverse.

For given values of C_{klmn} and ρ [102], equation 5.7 allows to directly calculate the speeds of sound for acoustic waves traveling along a given direction. This can be used to simulate the effect of an additional quasi-momentum of the domain wall. Figure 5.13 shows the calculated (quasi-)longitudinal speeds of sound (black curve) for different angles α in the xz -plane in the range from 0° to 90° , i.e. from wave propagation along z -direction to x -direction.

As expected, the speed of sound decreases when going from z -direction to x -direction. However, it is surprising that there is a local minimum at approximately 70° . For comparison, also the equation 5.5 known from the directional dispersion of Raman modes was plotted assuming the same speeds of sound in the pure x - and z -direction. It shows a slightly different behavior. The value of 27° calculated by this equation might be a bit overestimated, since the curve based on the equation of motion reaches comparable speeds of sound already at 20° .

Future experimental studies will show, which equation simulates the angular depen-

5 Applications

dence of the speed of sound best. Ideally, a LiNbO_3 crystal can be fabricated with hemispheric shape. On one hand, this allows a mounting on a biaxial goniometer stage for changing the incident light angle in arbitrary direction. On the other hand, the spherical shape prevents any light refraction at the surface, when focusing to the center. In a second step, also the investigation of domain walls in such a hemispherical crystal would be interesting, since nothing is known about how the quasi-momentum of the domain wall behaves at other angles of incidence.

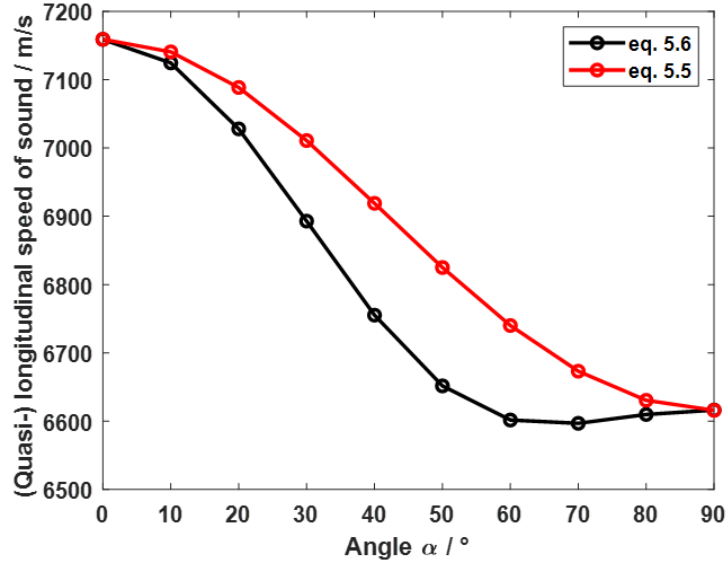


Figure 5.13: Calculated speeds of sound using either the equation of motion (5.6, black) or the equation known from directional dispersion (5.5, red).

Returning to the question of whether there is an analog to the Raman tensor formalism for Brillouin spectroscopy, brings one to the fundamental connection between the local displacement and the accompanying strain with the variation of the dielectric tensor, which ultimately causes the Brillouin scattering. Cummins et al. show that these quantities are linked by the photo-elastic effect (Pockel's tensor) and thus 3×3 matrices can be derived, which describe the Brillouin scattering intensity [109]. Interestingly, the form of these Brillouin tensors is similar to that of the Raman tensors. However, it needs to be mentioned that due to the propagation of the acoustic waves, there is not only one set of tensors like in Raman spectroscopy, but a set of three tensors for each different propagation direction. This might be the reason why the formalism is widely used in Raman spectroscopy only, but

5.1 Domain walls in lithium niobate

not in Brillouin spectroscopy. However, this would allow an important correlation between theory and experiment and should therefore be done in future studies.

5.2 Tumor biology of glioblastoma cells

5.2.1 Introduction

Along with cardiovascular diseases, tumor diseases are one of the most frequent causes of death in today's society [110]. Although cancer research is a growing field in which permanently new and more effective therapeutic treatment methods are developed, there are still tumor diseases, which are incurable and even lack of any satisfactory treatment [111].

One of these tumor types is the glioblastoma (GBM). It is a malignant primary brain tumor, which is categorized by the world health organization as grade 4 tumor pointing out that it is very aggressive and accompanied with a poor survival [111,112]. However, the overall incidence rate for a GBM is only about 3 per 100.000 persons [113]. GBMs belong to the brain tumor type of gliomas indicating that the tumor has its origin in the glial cells.

GBMs are characterized by a fast and aggressive growth [111]. This often results in a space-occupying lesion, which compresses the remaining brain tissue. As a result, most patients die after short time.

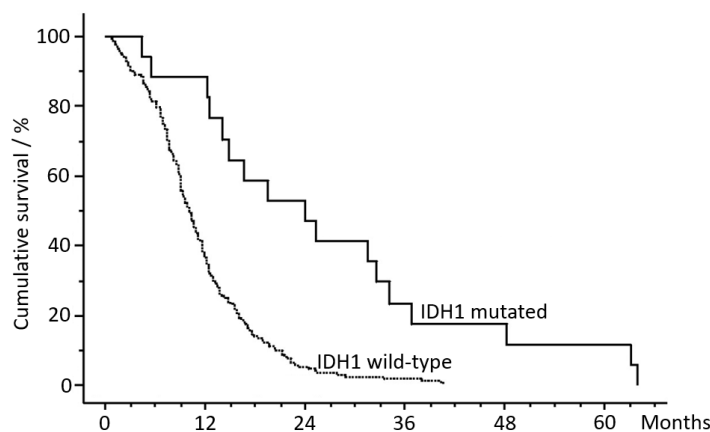


Figure 5.14: Kaplan-Meier plot for GBMs with and without *IDH1* mutation, showing that the *IDH1* mutation is associated with a prolonged survival time. Diagram is adapted from [114].

5.2 Tumor biology of glioblastoma cells

Kaplan-Meier plots, in which the cumulative survival is depicted as function of the time after treatment begin, exhibit how aggressive and difficult to treat GBMs are (cf. Fig. 5.14). The Kaplan-Meier plot of the wild-type tumors shows that the mean survival time is only about nine months [114]. Interestingly, patients with a mutation in the gene sequence, which codes for the *isocitrate dehydrogenase 1* (*IDH1*) enzyme, show a prolonged mean survival time of about 24 months. They make up 6 – 7 % of the primary GBM patients [115–117].

The typical treatment of a GBM consists of a neurosurgical resection, where the tumor is removed, and a subsequent radio- and/or chemotherapy [118]. The operation is sophisticated in the sense that only the tumor should be removed, but no surrounding normal brain tissue, because this could result in the loss of specific brain functions. For this balancing act, the neurosurgeons use different assistive tools, e.g. the 5-aminolevulinic acid fluorescence, magnet resonance and computer tomography images as well as immunohistochemical staining of intra-surgical frozen sections [119, 120] in order to resect the tumor with millimeter accuracy. The overall goal is to remove as much of the tumor while preserving important brain functions [121].

Despite these drastic medical interventions, the tumor recurrent rate is very high (> 90 %) leading to the high mortality [122]. This underlines the aggressive invasion of the tumor cells into surrounding tissue. The fact that the clinical treatment outcome has not notably improved in the last three decades, motivates the development of new therapeutic methods [113]. One promising target of a new therapy is the cellular biomechanics [123], because it is assumed to play a key role in tumor biology. On one hand, the solid tumor is very dense due to the fast replicating cells so that it compresses the surrounding tissue. The lack of sufficient nutrient supply in the center of the tumor results in a stiff necrotic core. On the other hand, single cells at the rim of the tumor are able to invade the surrounding tissue, whereby they have to be highly deformable in order to migrate through the cell-cell junctions [123]. This suggests that the biomechanical properties are not fixed but change during the tumor development stages.

One promising technique to characterize the biomechanical properties is Brillouin spectroscopy, since the Brillouin shift is related to the elastic modulus via the speed of sound (cf. 2.12 and 2.13). Its combination with related Raman spectroscopy

5 Applications

allows the correlation of biochemical with biomechanical properties. Therefore, the question, whether there are biochemical reasons underlying the cellular and tissue stiffness, can be answered by a combined setup.

5.2.2 State of the science

In the past, various techniques like atomic force microscopy (AFM), ultrasound microscopy and rheometry were used to characterize the biomechanics in cells and tissue. However, they either suffer from the fact that they are contact-based, or that they have low spatial resolution [1]. Therefore, the application of VIPAs in Brillouin spectrometers, first done by Scarcelli et al., was a great milestone, because from then on the accelerated acquisition of Brillouin spectra allowed to investigate also biological samples and to circumvent these drawbacks. Brillouin microscopy has the big advantage over the other techniques that it is contact-, label- and marker-free, non-destructive and has a high spatial resolution. Moreover, it can easily be combined with other optical techniques. Therefore, it is a promising tool for investigating biomechanics in oncology. However, Brillouin microscopy is still at the beginning of its widespread application, wherefore there are only few studies on tumor mechanics with this technique. Specifically on brain tumors, there are no Brillouin studies yet, wherefore first Brillouin investigations on other tumor entities will be presented in the following.

Conrad et al. cultured ovarian cancer nodules and investigated the effect of osmotic pressure on their biomechanical properties with Brillouin microscopy [124]. They demonstrated that the Brillouin shift shows the same trend as the Young's modulus determined by stress-strain measurement, which is up to date commonly used as gold standard. Although Brillouin spectroscopy and stress-strain measurements are not sensitive to the same modulus (longitudinal vs. Young's modulus), it is known from other studies [34,125] that they are related to each other and show the same trend, if the water content is not too high ($> 90\%$) [126]. Furthermore, it has to be mentioned that according to equations 2.12 and 2.13 the Brillouin shift and the longitudinal modulus are only proportional to each other, if the ratio of

the refractive index and the mass density is constant. Typically, this assumption is valid for biological tissue, which behaves as a two-substance water mixture [125]. Moreover, Conrad et al. showed that carboplatin, which is commonly used as chemotherapeutic agent for ovarian cancer, decreases the Brillouin shift. In another study, they investigated the effect of mechanical stress by applying a long-term continuous flow to the noduli, which resulted in decreased longitudinal moduli [127]. This study highlights that the tumor microenvironment plays an important role in tumor progression [123], which is also known from breast cancer cells [128].

Margueritat et al. investigated spheroids of colorectal carcinoma [129]. On one hand, they could show that the rim of a spheroid is more sensitive to drug therapy than the core. This is in line with other studies that indicate the presence of nutrient and diffusion gradients from the rim to the core of a spheroid [130, 131]. This highlights the features of spheroids serving as three-dimensional tumor model. Moreover, the authors demonstrated that there are complex signaling pathways in the cells, which regulate the cellular stiffness, for example by the expression of the glycoprotein E-cadherin. The pathways are promising targets for therapeutic treatment.

Trojanova-Wood et al. conducted Brillouin measurements on healthy and melanoma tissue of swines [132]. They found out that melanomas have a higher Brillouin shift than normal tissue. However, the mechanical properties of regressing melanoma are close to that of normal tissue. The study highlights the huge diagnostic potential of Brillouin spectroscopy.

In the past, the mechanical properties of brain tumor tissue were mainly investigated by AFM. It was reported that AFM measurements can be used to classify astrocytomas of grade II to IV with high accuracy [133]. In contrast to conventional classification by means of histopathology, this circumvents the interobserver variability. Moreover, AFM measurements revealed that durotactic cues play a major role in cell migration [134]. Furthermore, it was shown on different glioma cell lines that the rigidity of the extracellular matrix has a large impact on the structure, motility and proliferation, which play a key role for the invasion of cells into the brain parenchyma [135, 136]. The correlation between extracellular matrix stiffness and brain tumor aggressiveness is mediated by HIF1 protein [137]. Interestingly, this protein is dependent on the *IDH1* mutation state, whereby the presence of the mutation results in reduced mechanosignaling and thus less aggressiveness.

5 Applications

The *IDH1* mutation is a missense mutation, where the amino acid arginine is substituted [138]. Therefore, the correct function of the the *IDH1* enzyme is hampered. It occurs in an early stage of tumor development. Normally, it would catalyze the conversion from isocitrate to α -ketoglutarate. In the mutated state, however, α -ketoglutarate is converted into the oncometabolite 2-hydroxyglutarate [138]. The accumulation of 2-hydroxyglutarate inhibits α -ketoglutarate-dependent reactions. This leads to an increased histone and DNA methylation as well as an impaired cell differentiation. The DNA methylation, in turn, results in a plenty of other metabolic changes, because the transcription activity of the corresponding genes is altered (epigenetics). All in all, the genetic mutation disturbs the whole biochemistry of the cell, which leads to a less aggressive tumor that is less therapy-resistant and thus comes along with prolonged survival times [139].

Raman spectroscopy, on the other hand, has not only been used to distinguish between normal and neo-plastic tissue, but also for differentiation between different brain tumor types [140]. Moreover, the biochemical fingerprint was used to distinguish between necrotic and GBM tissue [141, 142]. Interestingly, Raman spectroscopy is also able to define the *IDH1* mutation status, because of the highly different biochemistry [143]. In general, Raman spectroscopy can be used to identify cellular compartments by their characteristic biochemical fingerprints [144].

The aim of the present work is to investigate the correlation of the biochemical with the biomechanical properties in GBM tumor models.

5.2.3 Results

In a first step, U87-MG glioblastoma cells were cultured on microscopy slides in order to allow a characterization of their biomechanical properties at subcellular resolution and correlate them with the cellular components. Therefore, cells were seeded on a Raman-grade CaF₂ slide. They were cultured with Dulbecco's Modified Eagle Medium (DMEM, Thermo Fisher Scientific Inc., Waltham, United States) in a cell culture incubator at 37° and 5% O₂ for one week. Afterwards, the slides were transferred to a petri dish with fresh culture medium and directly measured in order to ensure best environmental conditions. Generally, a water dipping objective

with $40\times$ magnification and $NA = 0.75$ was used for all measurements conducted in the culture medium.

Combined Brillouin and Raman maps were acquired from four different cells (15 s integration time, 2 accumulations for each measuring point, $1\ \mu\text{m}$ step size). Figure 5.15 shows a representative example.

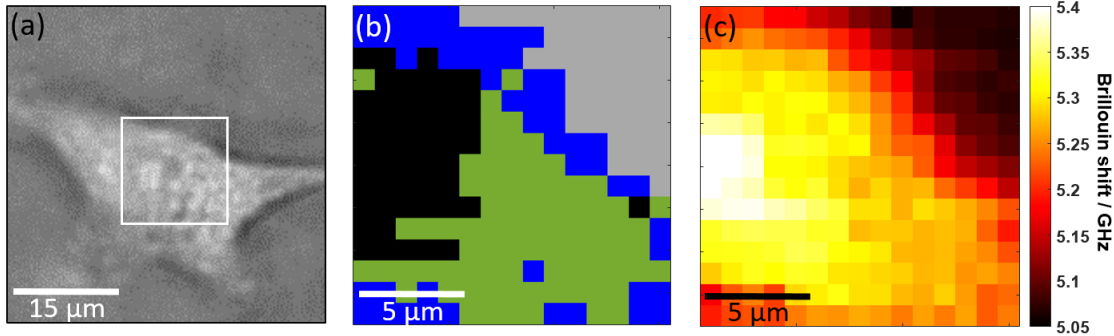


Figure 5.15: a) Bright field image of an adherent cell, which was visualized using b) a Raman k-means clustering and c) the Brillouin shift. Figure is adapted from [145].

The quadratic area marked by the white box in the bright field imaged (cf. Fig. 5.15a) was raster-scanned. The Raman spectra of each measuring point were background-corrected and normalized. A k-means clustering (using Matlab's *kmeans* function with Euclidean norm distance) was applied in order to identify four spectrally different clusters. The spectral signatures in the mean spectra (cf. Fig. 5.16) can be used to assign the clusters to the different cellular compartments. The mean spectrum of the black cluster shows prominent bands at $785\ \text{cm}^{-1}$, $1341\ \text{cm}^{-1}$ and $1579\ \text{cm}^{-1}$, which are associated with the DNA [146]. The green cluster has characteristic bands at $1264\ \text{cm}^{-1}$ and $1308\ \text{cm}^{-1}$, which indicate the presence of (phospho)lipids [146]. Since the green cluster is always located around the nucleus (cf. Fig. 5.15b), it represents a perinuclear region with high lipid content, which might include the endoplasmic reticulum, where lipids are synthesized [147]. The mean spectrum of the blue cluster indicates the presence of proteins ($820\ \text{cm}^{-1}$ [146]), which are present in the remaining part of the cytoplasm. The gray cluster is quite noisy, which indicates that mainly water was measured, wherefore the cluster can be assigned to the culturing medium. An approval of

5 Applications

this assignment is the location of the gray cluster in the Raman map, which is in agreement with the location of the culturing medium in the bright field image.

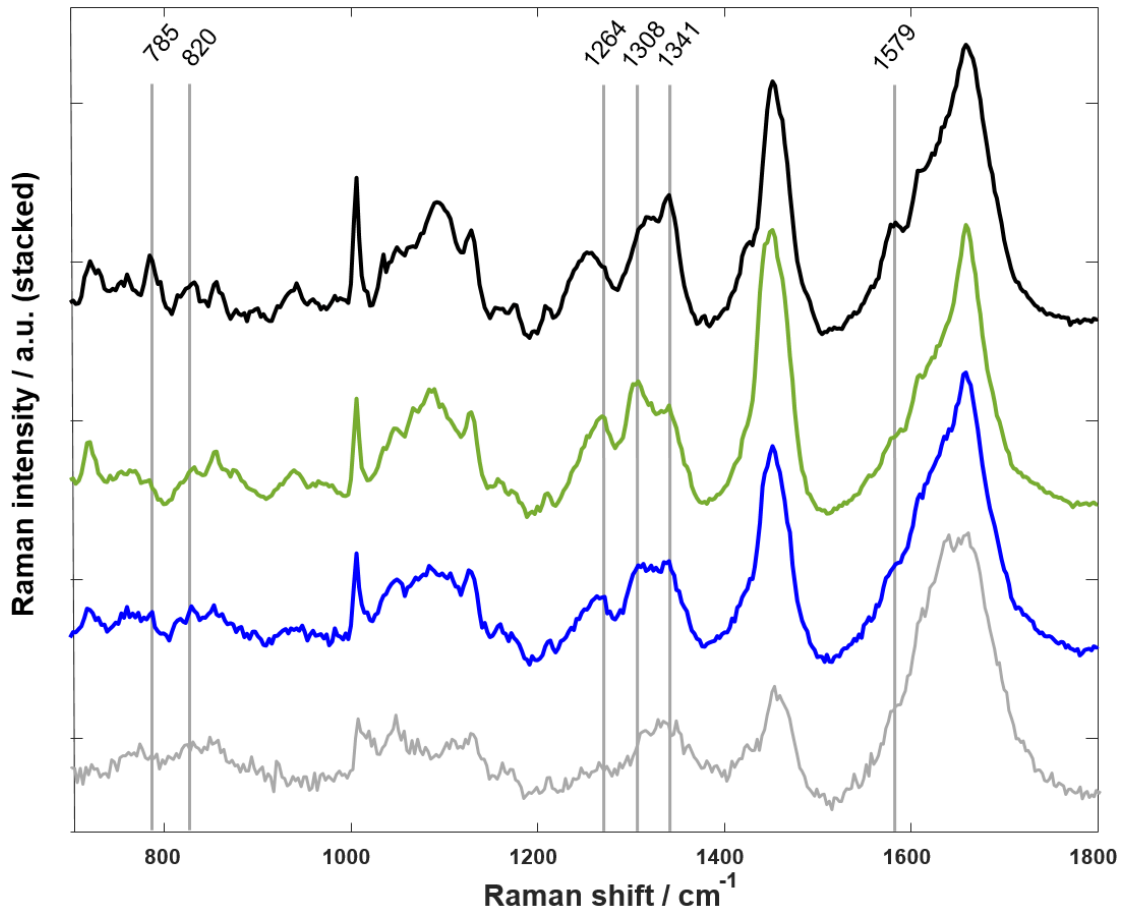


Figure 5.16: Mean spectra of the Raman clusters, which can be assigned to the nucleus (black), a perinuclear region (green), the remaining cytoplasm (blue) and the culturing medium (gray). Figure is adapted from [145].

Brillouin spectra were acquired simultaneously and co-localized with the Raman spectra. The Brillouin shift was used to generate a Brillouin map (cf. Fig. 5.15), where yellow and blue indicate high and low Brillouin shift values, respectively. The map shows high values (>5.30 GHz) in the region, which was previously assigned to the cell nucleus by the Raman clustering. A sub part of this region has actually the highest Brillouin shifts (5.35 GHz), which might represent the nucleolus. The remaining part of the cell and the surrounding culturing medium have a Brillouin shift of about 5.25 GHz and 5.1 GHz, respectively. It is noteworthy that the

Brillouin shift map shows no sharp border between the cell and the medium, but a continuous transition. This might be due to the nature of acoustic phonons, which are propagating inside the sample. Therefore, the measured Brillouin shift does not necessarily originate from the actual measuring point, but from a spot within the mean free path of the acoustic phonon resulting in a blurring [14].

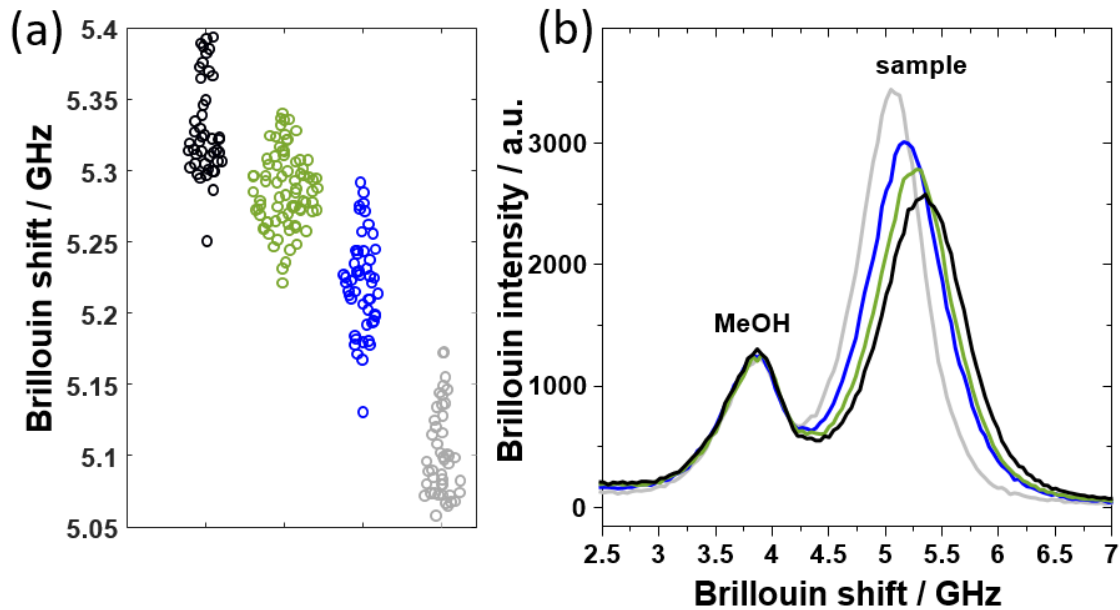


Figure 5.17: a) Correlation of the Brillouin shift values of each pixel with the corresponding Raman cluster showing that the cellular compartment of the black cluster is in average stiffer than that of the green, blue and gray cluster. b) The same trend can be seen in exemplary Brillouin spectra of the four clusters, where the band associated with the sample is shifting, whereas the methanol reference band is fix at 3.81 GHz . Figure is adapted from [145].

The co-localized acquisition of the Brillouin and Raman spectra allows to group the Brillouin shift values according to the Raman cluster assignment of the respective measurement position. The resulting scatter plot is depicted in Figure 5.17a. It shows that the Brillouin shift decreases, as one passes from the black to the gray cluster, although there is an overlap between the clusters. Interestingly, there is a subgroup in the black cluster, which has especially high Brillouin shifts, which again represents the nucleolus.

5 Applications

Figure 5.17b shows exemplary Brillouin spectra of the respective cell organelles assigned to the clusters. They show the same trend as the scatter plot, i.e. the Brillouin band associated with the sample is shifting with respect to the cluster. In contrast, the reference Brillouin band of methanol is constant at 3.81 GHz . Besides the shifting of the sample's Brillouin band, two other effects can be observed when comparing the different clusters. First, the Brillouin intensity behaves inversely to the Brillouin shift, i.e. lower Brillouin shift values are accompanied with higher intensity and vice versa. Second, the linewidth of the Brillouin band increases with increasing Brillouin shift. This suggests that not only the Brillouin shift can be used to generate a Brillouin map, but also the other two parameters retrieved from Lorentzian fitting. The corresponding maps are depicted in Figure 5.18.

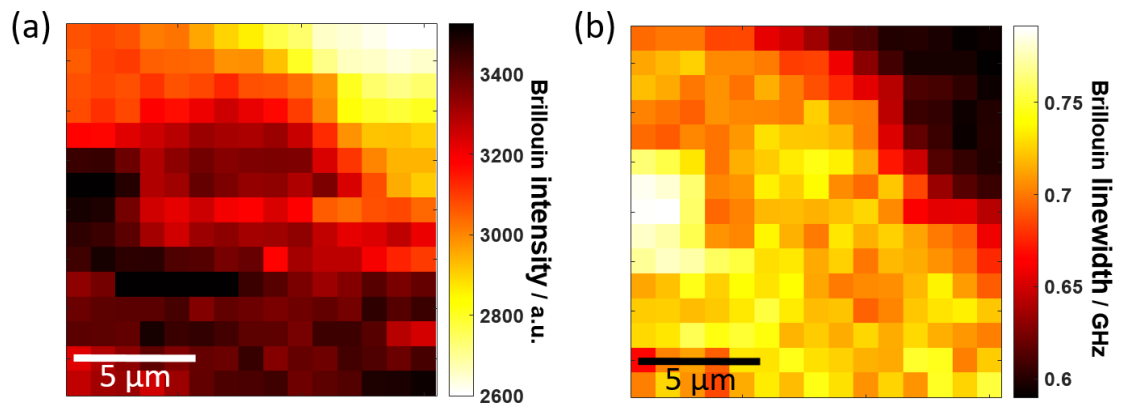


Figure 5.18: Brillouin maps using a) the intensity and b) the linewidth as contrast mechanism. While the intensity map shows an inverse behavior to the Brillouin shift map in Fig. 5.15c, the linewidth map has great similarity. Figure is adapted from [145].

Indeed, in both maps the cell can be distinguished from the culturing medium and even small variations in the cell are observable. Since the intensity map shows an inverse behavior compared to the Brillouin shift map, the culturing medium appears in bright color and the cell in dark one. In contrast, the linewidth map is in great accordance with the Brillouin shift map. One feature, however, is even better visible in the linewidth and the intensity map than in the Brillouin shift map, it is the region, where the nucleolus is assumed that is clearly separated.

The overall measuring time of one combined measurement was about two hours,

5.2 Tumor biology of glioblastoma cells

which is at the upper limit of what is acceptable for the cells without changing their shape due to blebbing. Thus, an increase of the integration time per pixel or of the number of pixels is not simply possible. However, a fixation of the cells with 4% formalin overcomes this limit. The only drawback is that the fixation alters the biomechanical properties, wherefore only the evaluation of the Raman data is reasonable. Nevertheless, this allows to perform a high-resolution Raman map, which can be used for verification of the Raman cluster assignment.

Eight Raman maps of fixed U87-MG cells were acquired with an overall measuring time of fifteen hours per map. One example is shown in Figure 5.19. Again, the Raman data were clustered with four clusters. The cluster map (cf. Fig. 5.19a) shows features, which are also visible in the bright field image (cf. Fig. 5.19b). The corresponding mean spectra (cf. Fig. 5.19c) are in great accordance with that of the living cell (cf. Fig. 5.15b). Therefore, the black cluster can again be assigned to the nucleus, the green one to a perinuclear region and the blue one to the cytoplasm. Here, the gray cluster is not associated with culturing medium, but with surrounding air, wherefore the Raman spectrum mainly consists of noise. All in all, this serves as a verification for the assignment of the clusters to the respective cell compartments. Thus, even in low-resolution maps with short integration times per pixel these clusters can be identified.

Although adherent cells are commonly used as tumor model, they are lacking of some characteristics, which are present in real tumors. For example, cell-cell contacts are neglected, which however play an important role in mechanosignaling [123]. Also the development of an extra cellular matrix is not possible in this tumor model. Furthermore, the typical nutrient gradient is missing [130]. All these points give rise to the need of another tumor model, which represents the properties of a tumor in a more realistic way. Cell spheroids are a tumor model, which exactly account for these issues. They are cell clusters growing in three dimensions. Spheroids are cultured from single cells by preventing any adhesion on the culturing flask. Proliferation of the cells results in the formation of spheroids.

In order to check, whether spheroids have other biomechanical properties than adherent cells, also spheroids of the U87-MG cell line were grown. They were cultured free-floating in DMEM under same conditions and transferred to a petri

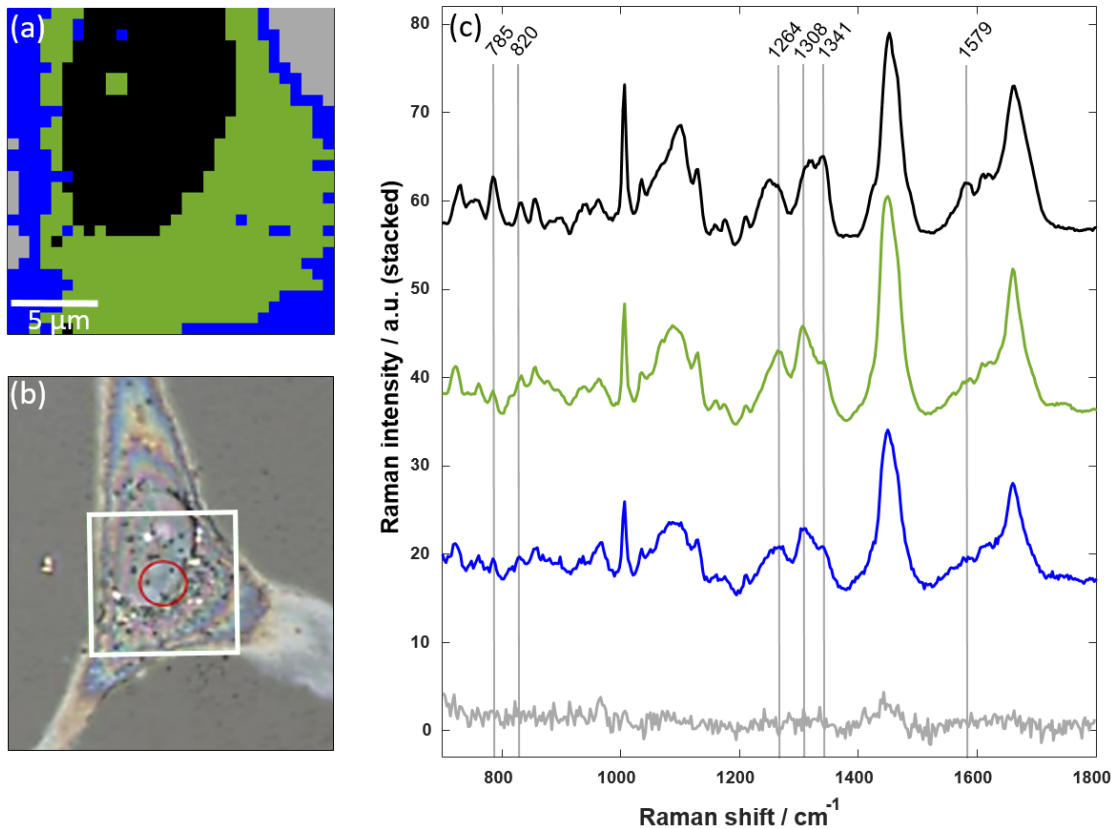


Figure 5.19: a) Raman cluster map of a fixed U87-MG cell revealing the same features visible in the b) bright field image of the cell (15 s integration time, 4 repetitions for each measuring point, 0.67 μm step size, 50 \times magnification objective). c) The mean spectra of the clusters show the same characteristic bands as for the living cells (cf. Fig. 5.15b), wherefore the assignment to the cellular compartments is confirmed. Figure is adapted from [145].

dish for measurement. For the comparison, eleven Brillouin maps of adherent cells and nine of spheroids were performed (0.2 s integration time per pixel, step size of 1 μm for adherent cells and 2 μm for spheroids, 50×50 pixels). An exemplary spheroid measurement is shown in Figure 5.20.

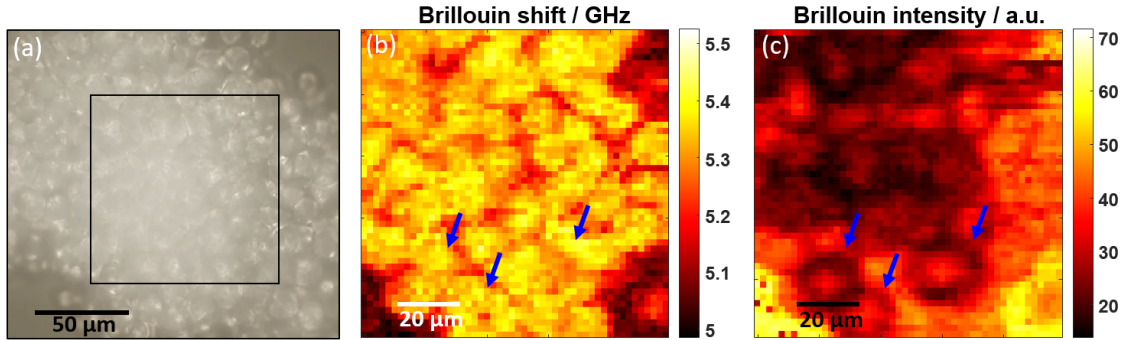


Figure 5.20: a) Bright field image of a U87-MG spheroid. b) Brillouin shift and c) Brillouin intensity map acquired from the black framed area. Blue arrows indicate positions, where different features are visible in the two maps. Figure is adapted from [145].

The bright field image (cf. Fig. 5.20a) shows the cell cluster structure of a spheroid, of which the black framed area in the focal plane was measured. The Brillouin shift map (cf. Fig. 5.20b) reveals not only the cells and the surrounding culturing medium, but also intercellular space. Interestingly, the Brillouin intensity map (cf. Fig. 5.20c) is not completely showing the same features. The three blue arrows indicate positions in the intensity map, where ring-shaped structures are visible, which are, however, missing in the Brillouin shift map. A plausible explanation for this observation is that the spheroids are three-dimensional objects and the scanned area is actually a section through the spheroid. Therefore, the scattering and absorption of light from cell layers above have to be taken into account. This has an impact on the Brillouin intensity, because it affects the amount of scattered photons. The Brillouin shift, however, is unaffected by this phenomenon, because the confocal measurement ensures that only the properties inside the confocal plane are investigated. Thus, in contrast to measurements on flat objects like the adherent cells, here, the Brillouin shift and the Brillouin intensity map do not contain completely the same information.

5 Applications

For comparing the biomechanics of cells grown as adherent cells and spheroids, the mean value of Brillouin maps cannot simply be used, since the maps contain a varying amount of surrounding medium and in the case of spheroids show also the presence of intercellular spaces. Therefore, the Brillouin shift values are plotted in a histogram, where the different contributions to the map are deconvoluted by fitting functions to the distribution. Figure 5.21 shows cumulative histograms for the adherent cell and the spheroids maps. Note that in the case of the adherent cells, the prominent medium contribution was subtracted for visualization reasons.

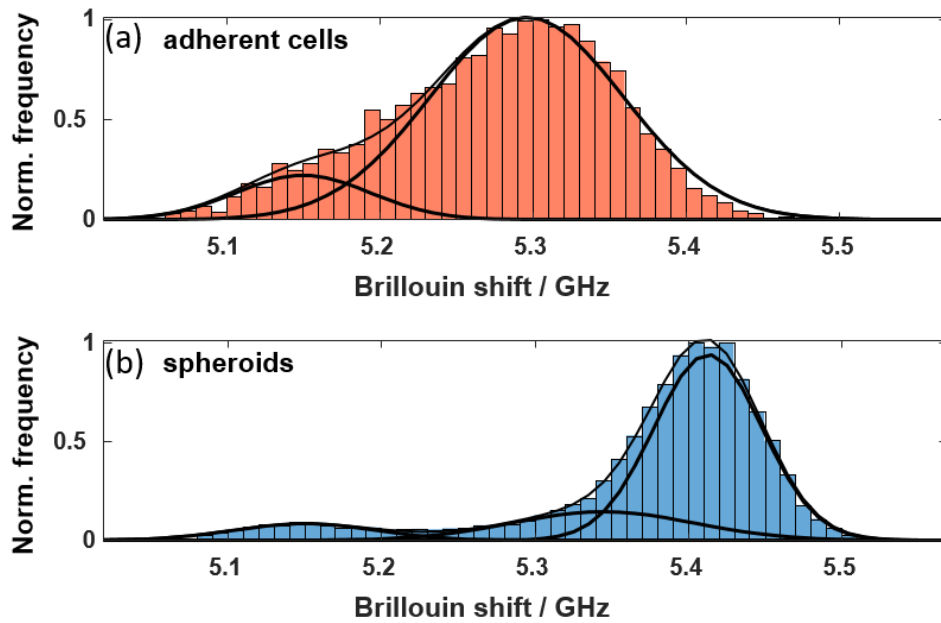


Figure 5.21: Cumulative histogram of the Brillouin shift values of the a) adherent cell maps and b) spheroid maps. Gaussian fitting reveals that the Brillouin shift is lower in adherent cells than in spheroids. Figure is adapted from [145].

Besides a major contribution at 5.3 GHz attributed to the cell itself, the histogram of the adherent cells reveals a contribution at 5.15 GHz . It can be attributed to the border between cells and medium and is also present in the histogram of the spheroids. Furthermore, the spheroid histogram has a major cell contribution at 5.4 GHz and minor contribution at 5.35 GHz , which is associated with the intercellular space. It is noteworthy that the contribution of the cell was only fitted by one Gaussian function, although the different cellular compartments

have different biomechanical properties as shown above. However, the scatter plot in Fig. 5.17a revealed a large overlap between the components, wherefore it is acceptable to use one Gaussian function for all of them.

Now, the biomechanics of the two tumor models can be compared by determining the Brillouin shift of the cell contribution for each single map, which is summarized in Figure 5.22.

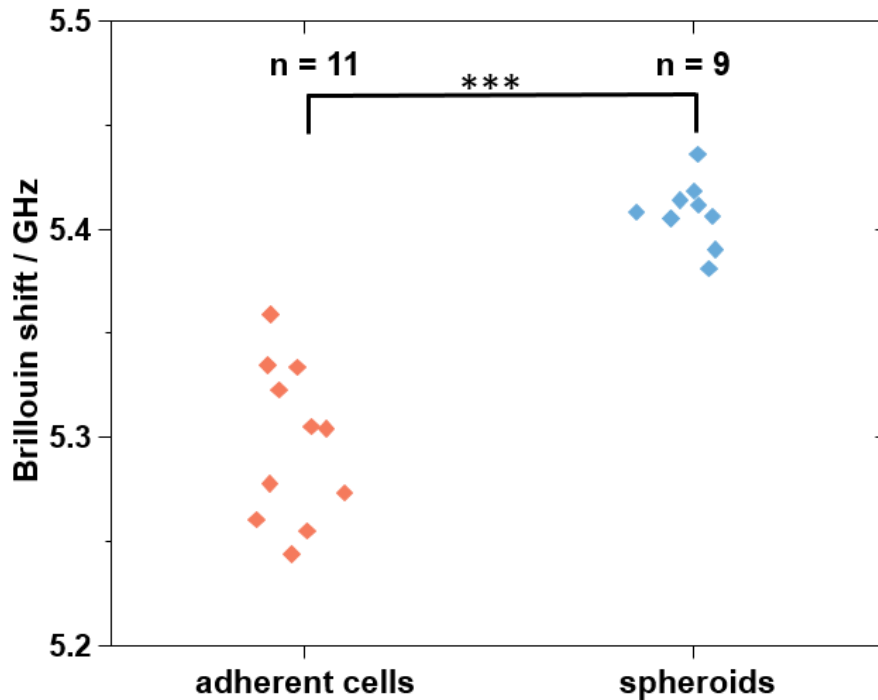


Figure 5.22: Comparison between the cellular Brillouin shift of adherent cells and spheroids showing the cells in three-dimensional tumor model are significantly stiffer. (Mann-Whitney U-test, *** $p < 0.001$) Figure is adapted from [145].

As already seen in the cumulative histograms, the Brillouin shift of the cell contribution is in the case of spheroids higher than that of the adherent cells (5.4 GHz vs. 5.3 GHz). A Mann-Whitney U-test confirmed that the values are significantly different ($p < 0.001$). Moreover, Figure 5.22 reveals a higher Brillouin shift variability for the adherent cell measurements. Most likely, this is due to the fact that the Brillouin shift is not only varying in lateral direction, but also in axial dimension. The focal plane position determines, which section plane is measured. In case of the

5 Applications

spheroids, a tight focusing is of minor relevance, because the cells are statistically laying in different axial depths. For the adherent cells, however, small variations in the focus position result in deviations of the Brillouin shift. All in all, this spreading of the measuring points does not alter the observation that the cellular stiffness is higher in the three-dimensional tumor model than in the two-dimensional one.

In a next step, combined measurements were conducted on spheroids in order to correlate their biochemical features with the biomechanical properties and to answer the question what causes the stiffness in spheroids. Since combined mappings take a long time as mentioned above, here, two combined line scans were performed instead (15 s integration time and 4 repetitions per pixel, step size of 1 μm , length 50 μm). The results of the line scans are summarized in Figure 5.23.

The measured Brillouin shifts (cf. Fig. 5.23 a and b) are varying between 5.3 GHz and 5.5 GHz . Plateau regions are indicating that the main Brillouin shift is around 5.4 GHz , which is in line with the previous results from the mappings.

The Raman heat maps (cf. Fig. 5.23 c and d), in which the Raman intensity is color-coded, reveal that there are different biochemical features present in the spheroids. The same features can be found in both line scans. Figure 5.23 e and f show a selection of Raman spectra of distinct positions, which allow to attribute the patterns visible in the heat map to cellular components. The Raman spectra at 35 μm of line scan 1 and 32 μm of line scan 2 (green) can be attributed to lipids due to the characteristic bands at 1267 cm^{-1} , 1306 cm^{-1} , 1441 cm^{-1} and 1748 cm^{-1} [146]. At these positions, the Brillouin curve shows highest shifts of about 5.5 GHz . Moreover, the spectral feature is present in the Raman spectra of several neighboring measurement points, wherefore it can be assumed that lipid droplets of micrometer-size are present in the spheroid.

Another pattern, which has high Brillouin shift values, is located at 15 μm of line scan 1 and 46 μm of line scan 2. The corresponding Raman spectra (violet) indicate the presence of proteins (863 cm^{-1} , 939 cm^{-1} , 1341 cm^{-1} , 1462 cm^{-1} and 1659 cm^{-1} [146]). Actually, the mentioned Raman spectrum of line scan 2 reveals also a mixture with lipids.

5.2 Tumor biology of glioblastoma cells

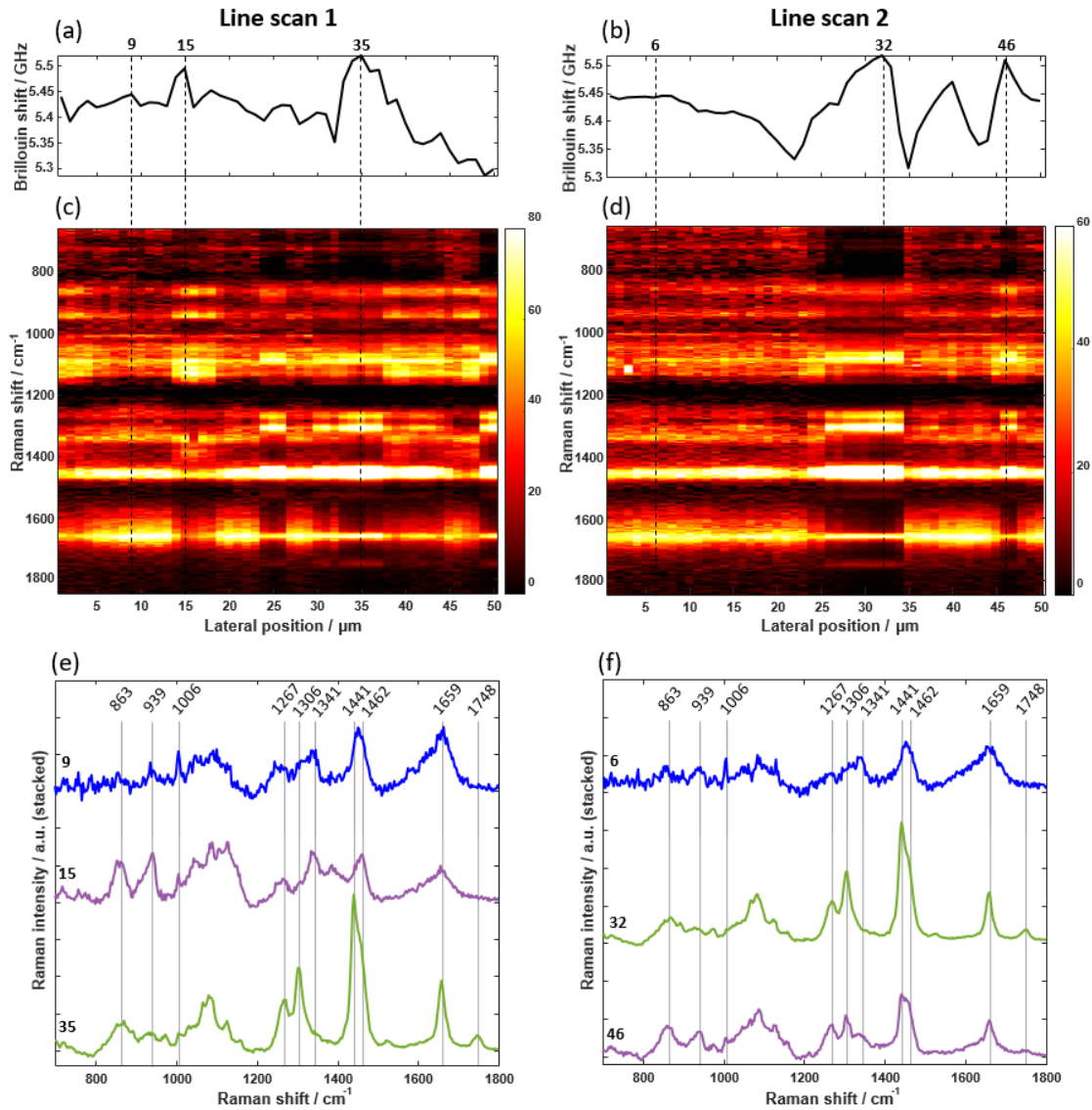


Figure 5.23: Combined line scans on U87-MG spheroids showing that the Brillouin shift (a) and b)) is driven by biochemical features visible in the Raman heat map (c) and d)). Selected Raman spectra (e) and f)) allow an attribution to lipid droplets, protein-rich regions and the cytoplasm. Figure is adapted from [145].

5 Applications

The Raman spectra at $9\ \mu\text{m}$ of line scan 1 and $6\ \mu\text{m}$ of line scan 2 (blue) laying in the plateau regions can be attributed to the cytoplasm, because they are comparatively noisy indicating a high water content and are in accordance with the adherent cell Raman spectrum, which was attributed to the cytoplasm (cf. Fig. 5.16). In conclusion, the cytoplasm is characterized by the general spheroid Brillouin shift of about $5.4\ \text{GHz}$, whereas proteins and lipids sporadically increase the Brillouin shift to $5.5\ \text{GHz}$.

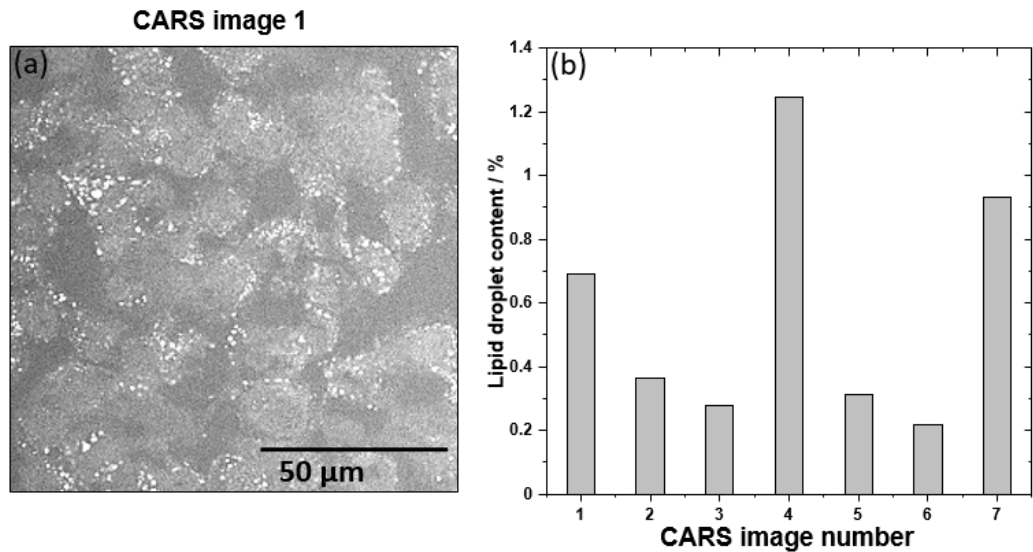


Figure 5.24: a) Exemplary CARS image of U87-MG spheroids revealing several lipid droplets. b) The lipid droplet content in the seven CARS images is between 0.2% and 1.4%. The exemplary image is CARS image number 1. Figure is adapted from [145].

In order to verify that the lipid bands are caused by lipid droplets, an imaging of lipid droplets was performed by CARS. For this purpose, U87-MG spheroids were embedded in cryotome matrix (OCT, CellPath Ltd., Newtown, United Kingdom), sectioned into $10\ \mu\text{m}$ thick sections and imaged with a multiphoton microscope, which is described elsewhere [148]. The lipid content in seven CARS images ($236 \times 236\ \mu\text{m}^2$, 2048×2048 pixels) was evaluated by doing a segmentation with Fiji software [149] using the 8-bit CARS intensity values.

An exemplary CARS image is shown in Figure 5.24a. The regions of high CARS signal intensity are confirming the presence of lipid droplets. They are usually

1 – 5 μm in size, which agrees well with the extent of the lipid signature in the line scans. The determined lipid droplet content of the spheroids (cf. Fig. 5.24b) in the seven CARS images is in the range of 0.2% to 1.4% with a mean value of about 0.5%. Thus, the CARS measurements confirm the presence of lipid droplets within spheroids, however, they make up only a minor fraction of the spheroid.

In a next step, spheroids were cultured from five primary human cell lines, i.e. cells, which are derived from a brain tumor biopsy. Brillouin mappings were performed in order to evaluate, whether different cell lines have different biomechanical properties. Table 5.2 summarizes the pathology and the number of Brillouin mappings (0.2 s integration time per pixel, step size 2 μm , 50×50 pixels). The GBM cell lines were described in detail in other publications [150–154]. Analogously to the evaluation of the U87-MG spheroid Brillouin maps, the Brillouin shift histograms were fitted with Gaussian functions to determine the cellular Brillouin shifts, which are plotted in Fig. 5.25a for the five cell lines.

Table 5.2: Overview of the primary cell lines summarizing the pathology and the number of mappings.

brain tumor number	pathology	number of Brillouin maps
HT7606	GBM	11
HT16360	GBM (recurrent)	12
HT18199	GBM	11
HT18816	GBM (recurrent)	11
HT12346	GBM (multifocal)	9

The scatter plot reveals that cell lines HT7606, HT18199 and HT18816 have a Brillouin shift of 5.5 GHz , whereas the Brillouin shift of HT16360 and HT12346 is 5.4 GHz . Thus, the cell lines can be divided into two groups. Interestingly, the evaluation of the number and content of lipid droplets by means of the CARS imaging (cf. Fig. 5.25b and c) showed the same grouping. The different amount of lipid droplets is also visible in the exemplary CARS images depicted in Figure 5.25d. These results suggest that there is a correlation between the amount of lipid droplets and the Brillouin shift.

5 Applications

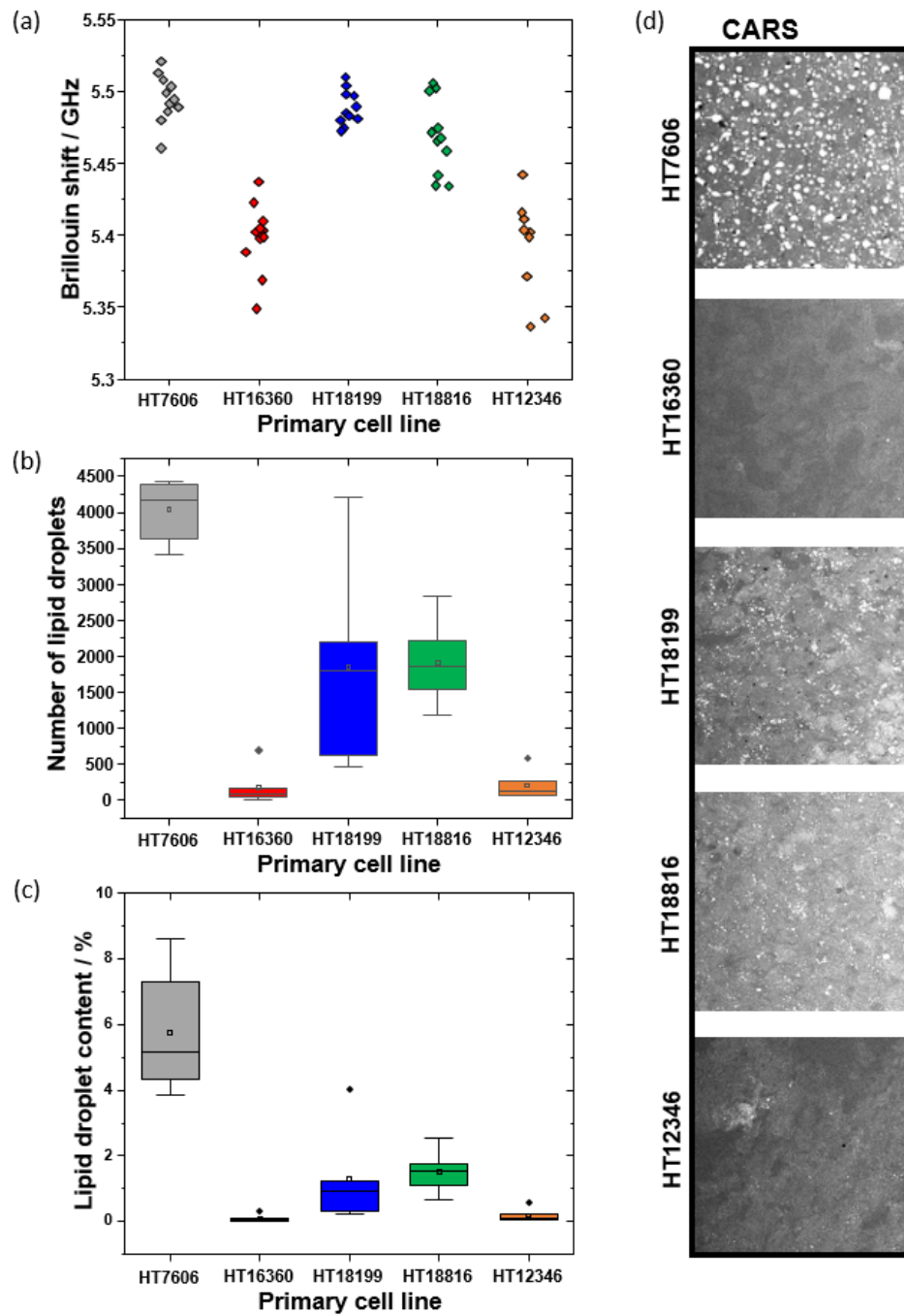


Figure 5.25: a) Brillouin maps of spheroids cultured from primary cell lines revealed that the Brillouin shift is about 5.4 GHz or 5.5 GHz depending on the cell line. b) The number and c) the content of lipid droplets for the different cell lines extracted from CARS images. d) Exemplary CARS images showing the different amount of lipid droplets.

5.2 Tumor biology of glioblastoma cells

In a final measurement series, the effect of the *IDH1* mutation on the Brillouin shift was investigated in order to evaluate, whether also the biomechanical properties are effected by the mutation, which might contribute to the different survival times of the patients. Therefore, a U87-MG *IDH1* wild-type cell line as well as a U87-MG cell line, in which the *IDH1* mutation was introduced by means of plasmid transfection, were cultured.

On one hand, Brillouin maps were acquired on twelve wild-type and twelve *IDH1*-mutated spheroids in order to evaluate their biomechanical properties (0.2 s integration time per pixel, step size 2 μm , 50×50 pixels). On the other hand, combined Brillouin and Raman line scans were conducted on ten spheroids, respectively, for correlating the biochemical fingerprint with the biomechanics (15 s integration time and 3 repetitions per pixel, step size 1 μm , length 50 μm).

Figure 5.26a shows the Brillouin shift values obtained from the maps analogously to the previous measurements. A Mann-Whitney U-test confirmed that the Brillouin shifts of the spheroids with *IDH1* mutation were significantly lower than that without mutation ($p < 0.01$).

The 1500 Raman spectra of the combined line scans were k-means clustered with 3 clusters. Interestingly, the violet cluster is only sparsely present in the line scans of the spheroids with *IDH1* mutation (cf. Fig. 5.26b where each row represent one line scan). The corresponding mean spectrum allows an attribution to the extracellular matrix (being a mixture of different components like collagen and proteoglycans) due to the prominent bands at 863 cm^{-1} , 942 cm^{-1} , 1130 cm^{-1} and 1341 cm^{-1} [146] (cf. Fig. 5.26c). The green cluster again indicates the presence of lipid droplets with its characteristic bands at 1264 cm^{-1} , 1308 cm^{-1} , 1441 cm^{-1} , 1659 cm^{-1} and 1748 cm^{-1} [146]. It is noteworthy that the amount of lipid droplets is roughly the same in the wild-type and mutated spheroids. The mean spectrum of the blue cluster is similar to the blue one of the fixed cell (cf. Fig. 5.19c), wherefore this cluster can be attributed to the cytoplasm.

The Brillouin shift was extracted from the Brillouin spectra of the combined line scans and visualized by a color-coding again (cf. Fig. 5.26d). The line scans confirm the observation of the mappings that the *IDH1* mutation is associated with lower Brillouin shift values.

5 Applications

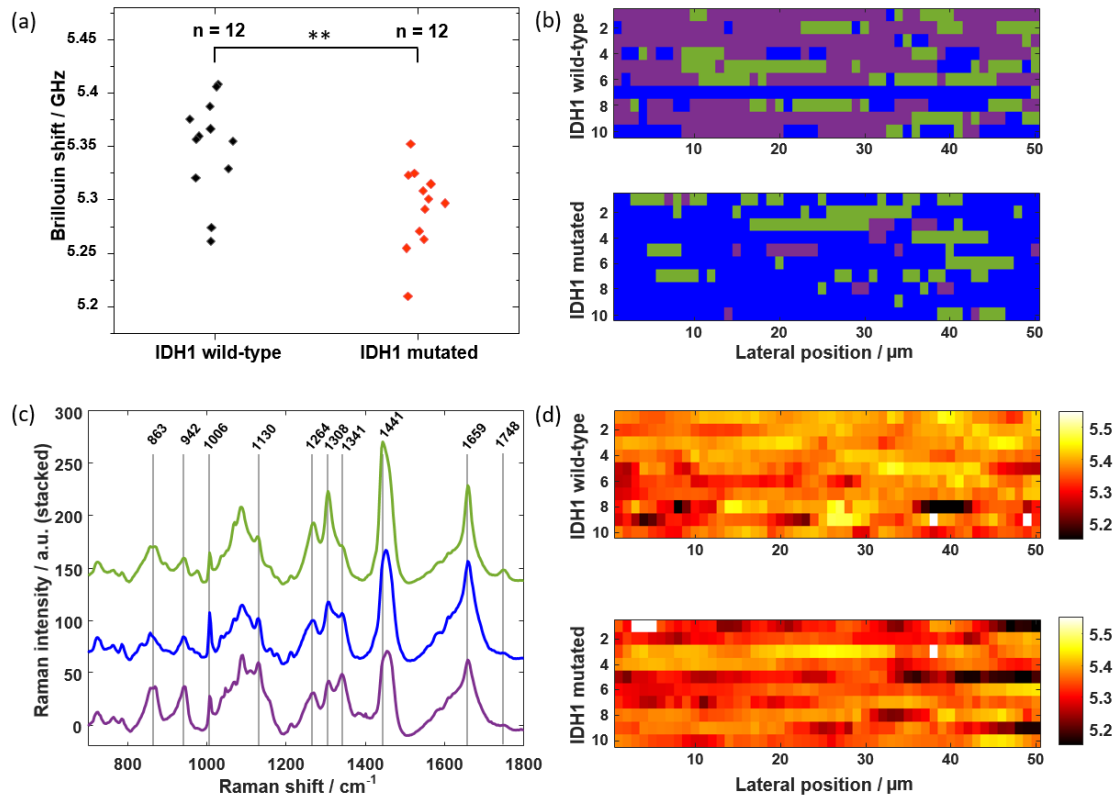


Figure 5.26: a) Scatter plot of the Brillouin shifts obtained from Brillouin maps of U87-MG spheroids with and without *IDH1* mutation showing that the *IDH1* mutation comes along with significantly lower stiffness. (Mann-Whitney U-test, $**p < 0.01$) b) A clustering of the Raman line scan spectra reveals three cluster, which can be assigned by the c) Raman mean spectra to lipid droplets (green), extracellular matrix (violet) and cytoplasm (blue). d) Corresponding Brillouin shifts of the line scans confirming the trend of the Brillouin mappings.

All in all, the measurements revealed that the extracellular matrix is under-expressed in the case of *IDH1* mutated spheroids. The correlative measurement shows that the extracellular matrix is responsible for a high stiffness, wherefore a lack of it results in decreased Brillouin shifts for the *IDH1* mutated spheroids.

5.2.4 Discussion

The combination of Brillouin and Raman spectroscopy was applied to glioblastoma tumor models in order to characterize their biomechanical and biochemical properties. In adherent cells, three different cellular compartments could be identified by the Raman fingerprint, which were the nucleus, a perinuclear region and the remaining cytoplasm. The Brillouin mapping revealed that the nucleus has the highest stiffness, followed by the perinuclear region and the cytoplasm. This is in line with previous findings [155–157].

Moreover, it was shown that not only the Brillouin shift can be used as imaging contrast, but also the Brillouin intensity and the linewidth. This can be explained by thermodynamic considerations [10, 158], which state that generally a higher Brillouin shift comes along with a decreased scattering intensity and a broadening. The comparison of the results obtained from the two-dimensional tumor model (adherent cells) with the three-dimensional one (spheroids) supports to the assumption that the culturing conditions (e.g. cell-cell contacts) have an impact on the cellular biomechanics. Comparing the Brillouin shift associated with the cytoplasm in adherent cells (cf. Fig. 5.17a) with that of spheroids (cf. Fig. 5.23) suggests that the difference originates from the biomechanics of the cytoplasm (5.25 GHz vs. 5.4 GHz). This should be kept in mind, when choosing an appropriate tumor model. Since the three-dimensional tumor model has several similarities with a real tumor, it is the preferred model. However, the two-dimensional model might simulate single metastasizing cells, which have lower stiffness for better migrating through the tissue, wherefore this tumor model might be used to investigate such oncogenic processes.

On first glance, one may also come to the conclusion that the difference in stiffness is caused by the lipid droplets, which are only present in spheroids and have a

5 Applications

high Brillouin shift of about 5.5 GHz (cf. Fig. 5.23 and Fig. 5.24). However, this conclusion is misleading, because the high Brillouin shift is not associated with a stiffness increase. Instead, the Brillouin shift is driven by the refractive index and the mass density. The ratio $\frac{n}{\sqrt{\rho}}$, which is decisive for the Brillouin shift (cf. Eq. (2.12) and Eq. (2.13)), is about 6% higher for lipid droplets compared to the cytoplasm, when assuming refractive indices of 1.41 [125] and 1.375 [159] as well as mass densities of 930 kg/m^3 [160] and 1000 kg/m^3 [161], respectively. Recently, a correlative study of Brillouin spectroscopy and optical diffraction tomography, where the Brillouin shift was co-registered with the refractive index, revealed that the elastic modulus of lipid droplets is even lower than that of the cytoplasm. This highlights the need of correlative approaches, which are able to identify such misleading Brillouin shifts (no matter if Brillouin spectroscopy is combined with Raman spectroscopy or optical diffraction tomography). On the other hand, in most cases the ratio $\frac{n}{\sqrt{\rho}}$ is constant, wherefore the Brillouin shift can be used as proxy for the stiffness [125].

The investigation of spheroids grown from primary cell lines revealed that cell lines with a notable lipid droplet content are showing higher Brillouin shifts. Since the Brillouin shift values for these cell lines are around 5.5 GHz , which is also the Brillouin shift associated with lipid droplets, it would be plausible to say that the lipid droplets are causing the higher Brillouin shift. However, the fact that the Brillouin shift is determined as the center value of a Gaussian fit function, where half of the values are even higher than the center value, contradicts this hypothesis, because the lipid droplets make up only less than 10% of a spheroid. Therefore, it cannot be assumed that the lipid droplets are directly causing high Brillouin shift values. Instead, there might be a mechanism, in which lipid droplets are triggering the cell to increase its stiffness and therefore indirectly causing high Brillouin shift values. In such a case, the high Brillouin shifts are really due to higher stiffness and not the result of an optical effect because of a high refractive index.

The comparison of *IDH1* wild-type and mutated U87-MG spheroids revealed a difference in the biomechanical and in the biochemical properties. The *IDH1* mutated spheroids are significantly less stiff and are almost lacking of an extracellular matrix. This conversely means that the components of the extracellular matrix (e.g. collagen and proteoglycans) are responsible for the stiffness in spheroids, which is in

line with [137]. However, it must be said that the *IDH1* mutation comes along with a plenty of metabolic changes, wherefore it is not surprising that it also affects the biomechanical parameters [162,163]. All in all, the finding that less stiff tumors are associated with a better prognosis is in line with previous results from endometrial carcinoma [164].

5.2.5 Outlook

In the present work, several basic investigations have been carried out, which pave the way for further developments in this research area. The comparison between cultivation conditions (adherent cells vs. spheroids) indicated that spheroids have a significantly higher stiffness. In this way, already five primary cell lines were investigated. However, more patient-derived cell lines should be analyzed in future studies in order to evaluate whether there is a correlation between the biomechanical properties and the treatment outcome or overall survival time of the patient. The combination with Raman spectroscopy then allows to identify new biochemical targets for therapies.

One issue, which remains unclear in this work, is the role of lipid droplets and their impact on biomechanics. It is well-known that GBMs have an abnormal lipid droplet metabolism [165,166]. On one hand, lipid droplets serve as energy storage, which allows the tumor to maintain an energy homeostasis also in glucose deprivation, e.g. due to rapid tumor growth accompanied with insufficient vascularization [167]. This might be the reason, why no lipid droplets were found in adherent cells, because they were well supplied with glucose from the culturing medium [168,169]. On the other hand, lipid droplets are an indicator of tumor aggressiveness, which highlights their clinical relevance. Therefore, a deeper understanding of the interplay between lipid droplets and tumor biomechanics is highly desirable. A first step might be the precise chemical analysis of lipids that have accumulated in the droplets. It could then be investigated whether therapeutic agents are able to change the lipid metabolism and thus alter the stiffness.

5 Applications

Another step that should be taken in the future is the investigation of fresh tumor samples directly obtained from the neurosurgical operation. Unlike tumor models grown under laboratory conditions, fresh tumor samples allow for the investigation of the tumor as it grew in the brain. However, the investigation of fresh brain tumor samples is not straightforward, because on one hand, the tissue is not plane and therefore difficult to be imaged, and on the other hand, the Brillouin shift is highly sensitive to the water content of the tissue as it is known e.g. from corneal tissue [170]. The evaporation of water results in higher Brillouin shifts, wherefore the evaluation of the actual biomechanical properties is distorted. One possibility to circumvent these issues is to directly embed the fresh tumor sample in agarose gel and slice it into plane sections with a vibratome. Coverslips laid on the sections reduce any evaporation but allows optical access. Such a measuring protocol would be able to bypass the experimental difficulties. However, what remains is the wide intra-tumor and inter-patient heterogeneity of GBMs.

Another milestone, which however is currently far away, is the intra-operative usage of a combined Brillouin and Raman system. Nowadays, there are already first investigations with an intra-operative Raman system, which allow for a distinction between normal and cancerous tissue as well as a cancer type classification [171]. The combination with a Brillouin spectrometer would make an in-vivo characterization of the tumor possible, whereby the dehydration issue is prevented by perfusion. However, it should clearly be stated that the additional information obtained from the Brillouin spectrum is not expected to considerably improve the tumor classification nor the identification of the tumor margin. For this purpose, the Brillouin information are too unspecific, whereas the chemical fingerprint of the Raman spectrum is already a very powerful tool. Therefore, the big advantage of such a combined intra-operative system would not be a better diagnostic, but a possibility to *in-vivo* correlate the biochemical and biomechanical properties, which might differ from the *ex-vivo* conditions. However, this milestone is also far away, because of the current unrobust and bulky setup as well as the long measurement times.

6 Overall discussion and outlook

In the present work, the setup of a combined Brillouin and Raman system is described, which was used in two different applications. On one hand, the physics of ferroelectric domain walls was investigated, and on the other hand, the tumor biology of glioblastoma cells. Although these research fields are quite different, in both cases the combined Brillouin and Raman system turned out to be a powerful tool. In a more general way, this highlights the great information content of vibrations. Since they are generally present in any material, this opens up widespread applications for the system.

Moreover, the results have shown that especially the combination of Brillouin and Raman spectroscopy is powerful. It is thanks to the co-registration that the two spectroscopic information can be correlated. Both applications revealed that without this correlation the interpretation of the results would be more difficult or even impossible, e.g. when thinking of the misleading Brillouin shift induced by the lipid droplets in GBMs. In this case, the combination is not only helpful, but even necessary for correct interpretation.

Although the combination of Brillouin and Raman spectroscopy appears obvious, not only because both are based on inelastic scattering of light on phonons, there are only a few of such systems in the world. One might think that the combination of both methods is sophisticated from a technical point of view. However, the clearly separated wavelength ranges of the Brillouin and Raman scattered light allows to simply use a dichroic beam splitter to separate both information. The subsequent detection is then the same as in single Brillouin and Raman spectrometers. Therefore, there is no technical limitation of a combined system. Instead, it can be assumed that other reasons, such as high purchasing costs and the know-how for

6 Overall discussion and outlook

evaluation and interpretation of the spectra, play a role, which is why there are only a few of such systems currently available.

One issue, however, which often occurs when combining two techniques, is that one requires longer acquisition times than the other. Therefore, the acquisition time of the slower technique represents the speed bottleneck being decisive for the overall acquisition time. Indeed, this could hamper some applications where the time required for the two methods is very different. Interestingly, in case of the domain wall investigations, Brillouin spectroscopy was the bottleneck (100 s measuring time for a single spectrum), whereas Raman spectroscopy was the bottleneck for the biomedical measurements (30 s measuring time). In both cases, there was a factor of approximately 100, by which the acquisition time of the faster technique had to be prolonged in order to agree with the time required for the slower technique. One reason for these contrary acquisition times of the two applications might be the sample itself. The high symmetry of a crystalline sample like LiNbO_3 results in the fact that the same optical phonons present in one unit cell, are present in all other unit cells, wherefore casually said the Raman spectrum contains only few but intense bands. In contrast, the high Brillouin shift caused by the high speed of sound in LiNbO_3 comes along with a low Brillouin intensity due to their inverse relationship (cf. Fig. 5.17b). In the case of the biomedical sample mainly consisting of water, the speed of sound is significantly lower (1500 m/s vs. 7000 m/s), wherefore also the Brillouin shift is much lower and the Brillouin band comparatively intense. In contrast, the unstructured and inhomogeneous nature of biomedical samples results in Raman spectra with very many bands, which in order to be well assignable require a low noise level. Moreover, the biological tissue consists mainly of water, which, however, does not generate any Raman signal. Therefore, a long integration time is required for Raman spectra of biomedical samples.

An interesting point gets apparent, when comparing the Brillouin map obtained from LiNbO_3 (cf. Fig. 5.12c) with that of an adherent cell (cf. Fig. 5.15c). In the latter case, there is a blurred transition of a few micrometers between the cell and the culturing medium, where the Brillouin shift continuously decreases. It is assumed that the mean free path of the acoustic phonons is limiting the spatial resolution [14]. In contrast, the Brillouin shift map of the domain walls

reveals sharp edges, which is in line with the 650 *nm*-linewidth of the signal in the high-resolution line scan. This gives rise to the assumptions that either the mean free path of acoustic phonons in LiNbO₃ is smaller than the laser spot size and/or due to the fact that the domain wall contrast only emerges, when hitting a domain wall, because only then the additional momentum occurs. The latter explanation would be an interesting approach for artificially improving the spatial resolution of Brillouin maps.

Although this work shows that generally combined Brillouin and Raman measurements are possible and reliable results can be obtained with these techniques, there is one inherent drawback for both spectroscopic methods, which is the low scattering cross-section. As mentioned in the introduction, only less than one of a million scattered photons is inelastically scattered. This highlights the need for long integration times in order to get reasonable spectra. In practice, the term *long* means something between tens of a second up to one minute to get a single spectrum. Therefore, the acquisition of a map for imaging purposes is very time-consuming and cumbersome and far away from real time imaging. In this work, the acquisition of combined maps usually took several hours. This is especially for biomedical samples a big drawback, since they are altering over time e.g. due to metabolic processes and movement. Moreover, this also prevents investigating processes, which take less time than the overall acquisition time, like the migration of a cell through an epithelial cell layer as model for invasive cells. Therefore, a massive speed-up of these techniques is necessary.

One obvious solution to speed up the acquisition time is to take advantage of coherent processes. For Raman spectroscopy this is already done in stimulated Raman scattering and CARS by exploiting non-linear optical effects when mixing multiple photons. Also for Brillouin spectroscopy there are efforts to develop stimulated versions. However, there are still some drawbacks. In impulsive stimulate Brillouin scattering, for example, a high-energy pump pulse is used to artificially generate phonons via electrostriction and thermal expansion [47]. This might work for several samples. In biological samples, however, there is a high potential

6 Overall discussion and outlook

for photodamage. In stimulated Brillouin spectroscopy, two counter-propagating continuous-waves are used to generate a standing acoustic wave [172]. Thus, only measurements in transmission geometry on mostly transparent samples are possible. This is feasible for cells, but not for tissue, which is considered as turbid medium. Moreover, this technique takes not full advantage of the non-linear effect, since no pulsed lasers are used [172].

These considerations give rise to the idea to develop a coherent version of Brillouin scattering similar to that known from Raman spectroscopy, i.e. to use a pulsed pump laser and a Stokes laser, whose difference in wavelength matches exactly a vibrational transition. Here, some technical challenges arise for Brillouin spectroscopy, which are quite similar to that discussed in the introduction. First, since the acoustic phonon energy is so small, very wavelength-stable lasers are needed. Second, the wavelength difference of the lasers has to be in the GHz -range only. Third, the linewidth of the laser emission has to be in the MHz -regime in order to facilitate a reasonable spectral resolution. Especially the last point is very critical, because the linewidth of a pulsed laser is coupled with its pulse duration. According to the Fourier transform, the linewidth behaves inverse to the pulse duration. This means that the pulse duration cannot be arbitrarily decrease, but has a limit. Assuming a desired linewidth of $10 MHz$ would result in a lower limit of $100 ns$. Since typical pulse durations for CARS are in the pico- and femtosecond regime, $100 ns$ seem quite long. This raises the question, how short pulse durations are required to take advantage of the non-linear effect. In this context, Meyer et al. showed that not the pulse duration but the peak power is decisive for the non-linear effect by doing CARS imaging of biological tissue with $65 ps$ pulses [173]. Since the results of spontaneous Brillouin and Raman spectroscopy on biomedical samples have revealed that the Brillouin signal is orders of magnitude higher than the Raman signal, this might open up new perspectives for coherent Brillouin imaging.

Another issue that needs to be considered in this context is that the Stokes laser is typically tuned to only one specific vibrational transition. This is suitable for Raman spectroscopy in order to image one specific biochemical feature like lipids. However, this does not allow the acquisition of a whole spectrum. For this purpose, a scanning Stokes laser or more sophisticated approaches are required

in order to perform e.g. so-called broadband-CARS [49]. Unfortunately, in the Raman spectrum obtained by CARS also a non-resonant background occurs, which is a by-product of the multiple photon interaction and hampers a straightforward interpretation of the spectrum. Therefore, stimulated Raman scattering might be the preferred coherent Raman technique, which generates Raman spectra similar to spontaneous Raman scattering.

Recently, Karpf et al. presented an interesting approach for stimulated Raman microscopy using a pulsed pump laser with 30 *ns* pulse duration and 415 *kHz* repetition rate as well as a fourier domain mode-locked laser as probe laser [174]. The trick of this approach is to record a time-encoded spectrum, i.e. the sweep range of the probe laser is divided into a constant number of spectral bins, for which successively a pump pulse is used to detect these spectral points. For Raman spectroscopy, a high number of spectral points (> 500) is desirable in order to have a high-quality Raman spectrum. If one would like to adapt the same approach for Brillouin spectroscopy, it would be sufficient to use only 100 spectral points in order to sample the Brillouin spectrum in the range of 5 *GHz* to 6 *GHz* in 10 *MHz* steps, since the Brillouin signal of biomedical samples is typically in this range. Smaller step sizes are not reasonable, since the pump laser linewidth is the limiting factor here. Actually, the currently used laser for spontaneous Brillouin and Raman spectroscopy already offers the possibility of a frequency scan and has a mode-hop-free tuning range of 20 *GHz*, which is far enough to scan the 1 *GHz* range of interest, wherefore it would already be a potential probe laser. The only open question is, whether there is a suitable pump laser, which emits ultra wavelength-stable (locked to an electronic transition), with *ns*-pulses and small linewidth. However, since no ultrashort pulses are required, it might be possible to implement a suitable pump laser based on available continuous-wave lasers using a Q-switch.

The long-term milestone of this idea is the implementation of a combined coherent Brillouin-Raman system, which allows for imaging in the range of a few seconds per image. While a frequency scanning is needed for detecting the Brillouin signal, it is maybe useful to tune a second Stokes laser only to one specific Raman transition. Since the Brillouin and the Raman spectral range are not overlapping, it would be possible to simultaneously perform both coherent techniques.

Bibliography

- [1] G. Scarcelli and S. H. Yun, “Confocal Brillouin microscopy for three-dimensional mechanical imaging,” *Nature Photonics* **2**, 39–43 (2008).
- [2] L. Brillouin, “Diffusion de la lumière et des rayons X par un corps transparent homogène - Influence de l’agitation thermique,” *Annales de Physique* **9**, 88–122 (1922).
- [3] C. V. Raman and K. S. Krishnan, “A new type of secondary radiation,” *Nature* **121**, 501–502 (1928).
- [4] P. Larkin, “Chapter 2 - Basic Principles,” in “Infrared and Raman Spectroscopy,” P. Larkin, ed. (Elsevier, Oxford, 2011), pp. 7–25.
- [5] R. Prevedel, A. Diz-Muñoz, G. Ruocco, and G. Antonacci, “Brillouin microscopy: an emerging tool for mechanobiology,” *Nature Methods* **16**, 969–977 (2019).
- [6] R. Gross and A. Marx, *Festkörperphysik* (De Gruyter Oldenbourg, 2014), 2nd ed.
- [7] P. R. Carey, “Raman spectroscopy, the sleeping giant in structural biology, awakes,” *Journal of Biological Chemistry* **274**, 26625–26628 (1999).

BIBLIOGRAPHY

- [8] S. S. Mitra, “Infrared and Raman Spectra Due to Lattice Vibrations,” in “Optical Properties of Solids: Papers from the NATO Advanced Study Institute on Optical Properties of Solids Held August 7–20, 1966, at Freiburg, Germany,” , S. Nudelman and S. S. Mitra, eds. (Springer US, Boston, MA, 1969), Optical Physics and Engineering, pp. 333–451.
- [9] M. Kim, S. Besner, A. Ramier, S. J. J. Kwok, J. An, G. Scarcelli, and S. H. Yun, “Shear Brillouin light scattering microscope,” *Optics Express* **24**, 319–328 (2016).
- [10] T. Still, “Basics and Brillouin Light Scattering,” in “High Frequency Acoustics in Colloid-Based Meso- and Nanostructures by Spontaneous Brillouin Light Scattering,” , T. Still, ed. (Springer, Berlin, Heidelberg, 2010), Springer Theses, pp. 9–34.
- [11] C. Bevilacqua, H. Sánchez-Iranzo, D. Richter, A. Diz-Muñoz, and R. Prevedel, “Imaging mechanical properties of sub-micron ECM in live zebrafish using Brillouin microscopy,” *Biomedical Optics Express* **10**, 1420–1431 (2019).
- [12] M. J. Damzen, V. Vlad, A. Mocofanescu, and V. Babin, *Stimulated Brillouin Scattering: Fundamentals and Applications* (CRC Press, Boca Raton, 2003).
- [13] W. Zou, X. Long, and J. Chen, *Brillouin scattering in optical fibers and its application to distributed sensors* (IntechOpen, 2015).
- [14] S. Caponi, D. Fioretto, and M. Mattarelli, “On the actual spatial resolution of Brillouin Imaging,” *Optics Letters* **45**, 1063–1066 (2020).
- [15] R. Schlüßler, S. Möllmert, S. Abuhattum, G. Cojoc, P. Müller, K. Kim, C. Möckel, C. Zimmermann, J. Czarske, and J. Guck, “Mechanical mapping of spinal cord growth and repair in living zebrafish larvae by Brillouin imaging,” *Biophysical Journal* **115**, 911–923 (2018).

BIBLIOGRAPHY

- [16] P. Shao, S. Besner, J. Zhang, G. Scarcelli, and S.-H. Yun, “Etalon filters for Brillouin microscopy of highly scattering tissues,” *Optics Express* **24**, 22232–22238 (2016).
- [17] W. Demtröder, “Experimentelle Hilfsmittel des Spektroskopikers,” in “Laserspektroskopie 1: Grundlagen,” , W. Demtröder, ed. (Springer, Berlin, Heidelberg, 2011), pp. 69–157.
- [18] M. Shirasaki, “Large angular dispersion by a virtually imaged phased array and its application to a wavelength demultiplexer,” *Optics Letters* **21**, 366–368 (1996).
- [19] R. Smith, K. L. Wright, and L. Ashton, “Raman spectroscopy: an evolving technique for live cell studies,” *Analyst* **141**, 3590–3600 (2016).
- [20] I. Ohana, Y. Yacoby, and M. Bezael, “Triple monochromator for Raman scattering with electronic coupling,” *Review of Scientific Instruments* **57**, 9–12 (1986).
- [21] G. Scarcelli and S. H. Yun, “Multistage VIPA etalons for high-extinction parallel Brillouin spectroscopy,” *Optics Express* **19**, 10913–10922 (2011).
- [22] A. Fiore, J. Zhang, P. Shao, S. H. Yun, and G. Scarcelli, “High-extinction virtually imaged phased array-based Brillouin spectroscopy of turbid biological media,” *Applied Physics Letters* **108**, 203701 (2016).
- [23] P. Hariharan and D. Sen, “Double-passed Fabry-Perot interferometer,” *JOSA* **51**, 398–399 (1961).
- [24] J. R. Sandercock, “Brillouin scattering study of SbSI using a double-passed, stabilised scanning interferometer,” *Optics Communications* **2**, 73–76 (1970).

BIBLIOGRAPHY

- [25] J. G. Dil, “Brillouin scattering in condensed matter,” *Reports on Progress in Physics* **45**, 285–334 (1982).
- [26] J. R. Sandercock, “Trends in Brillouin scattering: Studies of opaque materials, supported films, and central modes,” in “Light Scattering in Solids III: Recent Results,” , M. Cardona and G. Güntherodt, eds. (Springer, Berlin, Heidelberg, 1982), *Topics in Applied Physics*, pp. 173–206.
- [27] J. R. Sandercock, “Light scattering from surface acoustic phonons in metals and semiconductors,” *Solid State Communications* **26**, 547–551 (1978).
- [28] E. Edrei, M. C. Gather, and G. Scarcelli, “Integration of spectral coronagraphy within VIPA-based spectrometers for high extinction Brillouin imaging,” *Optics Express* **25**, 6895–6903 (2017).
- [29] F. Scarponi, S. Mattana, S. Corezzi, S. Caponi, L. Comez, P. Sassi, A. Morresi, M. Paolantoni, L. Urbanelli, C. Emiliani, L. Roscini, L. Corte, G. Cardinali, F. Palombo, J. R. Sandercock, and D. Fioretto, “High-performance versatile setup for simultaneous Brillouin-Raman micro-spectroscopy,” *Physical Review X* **7**, 031015 (2017).
- [30] Z. Meng and V. V. Yakovlev, “Precise determination of Brillouin scattering spectrum using a virtually imaged phase array (VIPA) spectrometer and charge-coupled device (CCD) Camera,” *Applied Spectroscopy* **70**, 1356–1363 (2016).
- [31] G. Scarcelli, P. Kim, and S. H. Yun, “Cross-axis cascading of spectral dispersion,” *Optics Letters* **33**, 2979–2981 (2008).
- [32] K. V. Berghaus, S. H. Yun, and G. Scarcelli, “High speed sub-GHz spectrometer for Brillouin scattering analysis,” *JoVE (Journal of Visualized Experiments)* p. e53468 (2015).

- [33] K. Berghaus, J. Zhang, S. H. Yun, and G. Scarcelli, “High-finesse sub-GHz-resolution spectrometer employing VIPA etalons of different dispersion,” *Optics Letters* **40**, 4436–4439 (2015).
- [34] G. Scarcelli, W. J. Polacheck, H. T. Nia, K. Patel, A. J. Grodzinsky, R. D. Kamm, and S. H. Yun, “Noncontact three-dimensional mapping of intracellular hydromechanical properties by Brillouin microscopy,” *Nature Methods* **12**, 1132–1134 (2015).
- [35] G. Antonacci, S. De Panfilis, G. Di Domenico, E. DelRe, and G. Ruocco, “Breaking the contrast limit in single-pass Fabry-Pérot spectrometers,” *Physical Review Applied* **6**, 054020 (2016).
- [36] J. Zhang, A. Fiore, S.-H. Yun, H. Kim, and G. Scarcelli, “Line-scanning Brillouin microscopy for rapid non-invasive mechanical imaging,” *Scientific Reports* **6**, 35398 (2016).
- [37] A. Fiore and G. Scarcelli, “Single etalon design for two-stage cross-axis VIPA spectroscopy,” *Biomedical Optics Express* **10**, 1475–1481 (2019).
- [38] C. Thomsen, H. T. Grahn, H. J. Maris, and J. Tauc, “Picosecond interferometric technique for study of phonons in the Brillouin frequency range,” *Optics Communications* **60**, 55–58 (1986).
- [39] M. Lejman, G. Vaudel, I. C. Infante, I. Chaban, T. Pezeril, M. Edely, G. F. Nataf, M. Guennou, J. Kreisel, V. E. Gusev, B. Dkhil, and P. Ruello, “Ultrafast acousto-optic mode conversion in optically birefringent ferroelectrics,” *Nature Communications* **7** (2016).
- [40] J. Czarske and H. Müller, “Heterodyne detection technique using stimulated Brillouin scattering and a multimode laser,” *Optics Letters* **19**, 1589–1591 (1994).

BIBLIOGRAPHY

- [41] T. Matsuoka, K. Sakai, and K. Takagi, “Hyper-resolution Brillouin–Rayleigh spectroscopy with an optical beating technique,” *Review of Scientific Instruments* **64**, 2136–2139 (1993).
- [42] M. Schünemann, K. Sperlich, K. Barnscheidt, S. Schöpa, J. Wenzel, S. Kalies, A. Heisterkamp, H. Stolz, O. Stachs, and B. Hage, “Balanced heterodyne Brillouin spectroscopy towards tissue characterization,” *IEEE Access* **10**, 24340–24348 (2022).
- [43] Y. Li, B. Shen, S. Li, Y. Zhao, J. Qu, and L. Liu, “Review of stimulated Raman scattering microscopy techniques and applications in the biosciences,” *Advanced Biology* **5**, 2000184 (2021).
- [44] I. Remer and A. Bilenca, “Background-free Brillouin spectroscopy in scattering media at 780 nm via stimulated Brillouin scattering,” *Optics Letters* **41**, 926–929 (2016).
- [45] I. Remer and A. Bilenca, “High-speed stimulated Brillouin scattering spectroscopy at 780 nm,” *APL Photonics* **1**, 061301 (2016).
- [46] C. W. Ballmann, J. V. Thompson, A. J. Traverso, Z. Meng, M. O. Scully, and V. V. Yakovlev, “Stimulated Brillouin scattering microscopic imaging,” *Scientific Reports* **5**, 18139 (2015).
- [47] B. Krug, N. Koukourakis, J. W. Czarske, and J. W. Czarske, “Impulsive stimulated Brillouin microscopy for non-contact, fast mechanical investigations of hydrogels,” *Optics Express* **27**, 26910–26923 (2019).
- [48] C. W. Ballmann, Z. Meng, A. J. Traverso, M. O. Scully, and V. V. Yakovlev, “Impulsive Brillouin microscopy,” *Optica* **4**, 124–128 (2017).

- [49] F. Hempel, S. Reitzig, M. Rüsing, and L. M. Eng, “Broadband coherent anti-Stokes Raman scattering for crystalline materials,” *Physical Review B* **104**, 224308 (2021).
- [50] J. P. Pezacki, J. A. Blake, D. C. Danielson, D. C. Kennedy, R. K. Lyn, and R. Singaravelu, “Chemical contrast for imaging living systems: molecular vibrations drive CARS microscopy,” *Nature Chemical Biology* **7**, 137–145 (2011).
- [51] F. Palombo, M. Madami, N. Stone, and D. Fioretto, “Mechanical mapping with chemical specificity by confocal Brillouin and Raman microscopy,” *Analyst* **139**, 729–733 (2014).
- [52] F. Palombo, M. Madami, D. Fioretto, J. Nallala, H. Barr, A. David, and N. Stone, “Chemico-mechanical imaging of Barrett’s oesophagus,” *Journal of Biophotonics* **9**, 694–700 (2016).
- [53] F. Palombo, F. Masia, S. Mattana, F. Tamagnini, P. Borri, W. Langbein, and D. Fioretto, “Hyperspectral analysis applied to micro-Brillouin maps of amyloid-beta plaques in Alzheimer’s disease brains,” *The Analyst* **143**, 6095–6102 (2018).
- [54] D. Fioretto, S. Caponi, and F. Palombo, “Brillouin-Raman mapping of natural fibers with spectral moment analysis,” *Biomedical Optics Express* **10**, 1469–1474 (2019).
- [55] S. Mattana, M. Mattarelli, L. Urbanelli, K. Sagini, C. Emiliani, M. D. Serra, D. Fioretto, and S. Caponi, “Non-contact mechanical and chemical analysis of single living cells by microspectroscopic techniques,” *Light: Science & Applications* **7**, 17139–17139 (2018).

BIBLIOGRAPHY

- [56] M. A. Cardinali, M. Govoni, D. Dallari, S. Caponi, D. Fioretto, and A. Morresi, “Mechano-chemistry of human femoral diaphysis revealed by correlative Brillouin–Raman microspectroscopy,” *Scientific Reports* **10**, 17341 (2020).
- [57] M. A. Cardinali, A. Morresi, D. Fioretto, L. Vivarelli, D. Dallari, and M. Govoni, “Brillouin and Raman micro-spectroscopy: A tool for micro-mechanical and structural characterization of cortical and trabecular bone tissues,” *Materials* **14**, 6869 (2021).
- [58] M. A. Cardinali, A. Di Michele, M. Mattarelli, S. Caponi, M. Govoni, D. Dallari, S. Brogini, F. Masia, P. Borri, W. Langbein, F. Palombo, A. Morresi, and D. Fioretto, “Brillouin-Raman microspectroscopy for the morpho-mechanical imaging of human lamellar bone,” *Journal of the Royal Society, Interface* **19**, 20210642 (2022).
- [59] S. Caponi, D. Fioretto, and M. Mattarelli, “Transition across a sharp interface: Data from Raman and Brillouin imaging spectroscopy,” *Data in Brief* **33**, 106368 (2020).
- [60] M. Bailey, B. Gardner, M. Alunni-Cardinali, S. Caponi, D. Fioretto, N. Stone, and F. Palombo, “Predicting the refractive index of tissue models using light scattering spectroscopy,” *Applied Spectroscopy* **75**, 574–580 (2021).
- [61] A. J. Traverso, J. V. Thompson, Z. A. Steelman, Z. Meng, M. O. Scully, and V. V. Yakovlev, “Dual Raman-Brillouin microscope for chemical and mechanical characterization and imaging,” *Analytical Chemistry* **87**, 7519–7523 (2015).
- [62] M. Troyanova-Wood, C. Gobbell, Z. Meng, and V. V. Yakovlev, “Assessing the effect of a high-fat diet on rodents’ adipose tissue using Brillouin and Raman spectroscopy,” in “Optical Biopsy XIV: Toward Real-Time Spectroscopic Imaging and Diagnosis,” , vol. 9703 (International Society for Optics and Photonics, 2016), vol. 9703, p. 970310.

- [63] M. Troyanova-Wood, C. Gobbell, Z. Meng, O. Gasheva, A. Gashev, and V. V. Yakovlev, “Assessing the effect of prolonged use of desloratadine on adipose Brillouin shift and composition in rats,” *Journal of Biophotonics* **14**, e202000269 (2021).
- [64] Z. Meng, S. C. B. Lopez, K. E. Meissner, and V. V. Yakovlev, “Subcellular measurements of mechanical and chemical properties using dual Raman-Brillouin microspectroscopy,” *Journal of Biophotonics* **9**, 201–207 (2016).
- [65] M. Nikolić and G. Scarcelli, “Long-term Brillouin imaging of live cells with reduced absorption-mediated damage at 660nm wavelength,” *Biomedical Optics Express* **10**, 1567–1580 (2019).
- [66] P. Siddons, C. S. Adams, C. Ge, and I. G. Hughes, “Absolute absorption on rubidium D lines: comparison between theory and experiment,” *Journal of Physics B: Atomic, Molecular and Optical Physics* **41**, 155004 (2008).
- [67] V. Jacques, B. Hingant, A. Allafort, M. Pigéard, and J. F. Roch, “Nonlinear spectroscopy of rubidium: an undergraduate experiment,” *European Journal of Physics* **30**, 921–934 (2009).
- [68] T. W. Hänsch, I. S. Shahin, and A. L. Schawlow, “High-resolution saturation spectroscopy of the sodium D lines with a pulsed tunable dye laser,” *Physical Review Letters* **27**, 707–710 (1971).
- [69] I. Divliansky, *Volume Bragg gratings: Fundamentals and applications in laser beam combining and beam phase transformations* (IntechOpen, 2017).
- [70] E. D. Black, “An introduction to Pound–Drever–Hall laser frequency stabilization,” *American Journal of Physics* **69**, 79–87 (2001).

BIBLIOGRAPHY

- [71] R. J. Thompson, M. Tu, D. C. Aveline, N. Lundblad, and L. Maleki, “High power single frequency 780nm laser source generated from frequency doubling of a seeded fiber amplifier in a cascade of PPLN crystals,” *Optics Express* **11**, 1709–1713 (2003).
- [72] W. Sohler, “Integrated optics in LiNbO₃,” *Thin Solid Films* **175**, 191–200 (1989).
- [73] Y. Xu, *Ferroelectric materials and their applications* (North-Holland ; Sole distributors for the USA and Canada, Elsevier Science Pub. Co., Amsterdam; New York; New York, NY, USA, 1991).
- [74] F. Chen, L. Kong, W. Song, C. Jiang, S. Tian, F. Yu, L. Qin, C. Wang, and X. Zhao, “The electromechanical features of LiNbO₃ crystal for potential high temperature piezoelectric applications,” *Journal of Materiomics* **5**, 73–80 (2019).
- [75] G. A. Smolenskii, N. N. Krainik, N. P. Khuchua, V. V. Zhdanova, and I. E. Mylnikova, “The Curie temperature of LiNbO₃,” *physica status solidi (b)* **13**, 309–314 (1966).
- [76] A. Savage, “Pyroelectricity and Spontaneous Polarization in LiNbO₃,” *Journal of Applied Physics* **37**, 3071–3072 (1966).
- [77] L. Myers and W. Bosenberg, “Periodically poled lithium niobate and quasi-phase-matched optical parametric oscillators,” *IEEE Journal of Quantum Electronics* **33**, 1663–1672 (1997).
- [78] C. Godau, T. Kämpfe, A. Thiessen, L. M. Eng, and A. Haußmann, “Enhancing the domain wall conductivity in lithium niobate single crystals,” *ACS Nano* **11**, 4816–4824 (2017).

- [79] C. S. Werner, S. J. Herr, K. Buse, B. Sturman, E. Soergel, C. Razzaghi, and I. Breunig, “Large and accessible conductivity of charged domain walls in lithium niobate,” *Scientific Reports* **7**, 9862 (2017).
- [80] Y. Ike and S. Kojima, “Brillouin scattering measurement of stoichiometric lithium niobate crystals by using an angular dispersion-type Fabry-Perot interferometer,” *Journal of the Korean Physical Society* **46**, 90–92 (2005).
- [81] H. S. Lim, J. D. Huang, V. L. Zhang, M. H. Kuok, and S. C. Ng, “Evaluation of acoustic physical constants of LiNbO_3 at hypersonic frequencies,” *Journal of Applied Physics* **93**, 9703–9708 (2003).
- [82] A. de Bernabé, C. Prieto, and A. de Andrés, “Effect of stoichiometry on the dynamic mechanical properties of LiNbO_3 ,” *Journal of Applied Physics* **79**, 143–148 (1996).
- [83] S. Abrahams, “Ferroelectric lithium niobate. 3. Single crystal X-ray diffraction study at 24°C ,” *Journal of Physics and Chemistry of Solids* **27**, 997–1012 (1966).
- [84] K. Momma and F. Izumi, “VESTA 3 for three-dimensional visualization of crystal, volumetric and morphology data,” *Journal of Applied Crystallography* **44**, 1272–1276 (2011).
- [85] A. S. Barker and R. Loudon, “Dielectric properties and optical phonons in LiNbO_3 ,” *Physical Review* **158**, 433–445 (1967).
- [86] M. D. Fontana and P. Bourson, “Microstructure and defects probed by Raman spectroscopy in lithium niobate crystals and devices,” *Applied Physics Reviews* **2**, 040602 (2015).
- [87] T. C. Damen, S. P. S. Porto, and B. Tell, “Raman effect in zinc oxide,” *Physical Review* **142**, 570–574 (1966).

BIBLIOGRAPHY

- [88] M. Rüsing, S. Neufeld, J. Brockmeier, C. Eigner, P. Mackwitz, K. Spychala, C. Silberhorn, W. G. Schmidt, G. Berth, A. Zrenner, and S. Sanna, “Imaging of 180° ferroelectric domain walls in uniaxial ferroelectrics by confocal Raman spectroscopy: Unraveling the contrast mechanism,” *Physical Review Materials* **2**, 103801 (2018).
- [89] C. Kranert, C. Sturm, R. Schmidt-Grund, and M. Grundmann, “Raman tensor formalism for optically anisotropic crystals,” *Physical Review Letters* **116**, 127401 (2016).
- [90] R. Loudon, “The Raman effect in crystals,” *Advances in Physics* **13**, 423–482 (1964).
- [91] R. F. Schaufele and M. J. Weber, “Raman scattering by lithium niobate,” *Physical Review* **152**, 705–708 (1966).
- [92] S. Sanna, S. Neufeld, M. Rüsing, G. Berth, A. Zrenner, and W. G. Schmidt, “Raman scattering efficiency in LiTaO_3 and LiNbO_3 crystals,” *Physical Review B* **91**, 224302 (2015).
- [93] M. D. Fontana, R. Hammoum, P. Bourson, S. Margueron, and V. Y. Shur, “Raman probe on PPLN microstructures,” *Ferroelectrics* **373**, 26–31 (2008).
- [94] G. Stone and V. Dierolf, “Influence of ferroelectric domain walls on the Raman scattering process in lithium tantalate and niobate,” *Optics Letters* **37**, 1032–1034 (2012).
- [95] T. Jach, S. Kim, V. Gopalan, S. Durbin, and D. Bright, “Long-range strains and the effects of applied field at 180° ferroelectric domain walls in lithium niobate,” *Physical Review B* **69**, 064113 (2004).

- [96] Y. Zhang, L. Guilbert, and P. Bourson, “Characterization of Ti:LiNbO₃ waveguides by micro-raman and luminescence spectroscopy,” *Applied Physics B* **78**, 355–361 (2004).
- [97] D. Lee, R. K. Behera, P. Wu, H. Xu, Y. L. Li, S. B. Sinnott, S. R. Phillpot, L. Q. Chen, and V. Gopalan, “Mixed Bloch-Néel-Ising character of 180° ferroelectric domain walls,” *Physical Review B* **80**, 060102 (2009).
- [98] D. A. Bryan, R. Gerson, and H. E. Tomaschke, “Increased optical damage resistance in lithium niobate,” *Applied Physics Letters* **44**, 847–849 (1984).
- [99] J. Rix, M. Rüsing, R. Galli, J. Golde, S. Reitzig, L. M. Eng, and E. Koch, “Brillouin and Raman imaging of domain walls in periodically-poled 5%-MgO:LiNbO₃,” *Optics Express* **30**, 5051–5062 (2022).
- [100] D. E. Zelmon, D. L. Small, and D. Jundt, “Infrared corrected Sellmeier coefficients for congruently grown lithium niobate and 5 mol. % magnesium oxide-doped lithium niobate,” *JOSA B* **14**, 3319–3322 (1997).
- [101] Y. Sirotin, M. Shaskolskaya, and V. Snigirevskaya, *Fundamentals of crystal physics* (Mir, Moscow, 1982).
- [102] A. S. Andrushchak, B. G. Mytsyk, H. P. Laba, O. V. Yurkevych, I. M. Solskii, A. V. Kityk, and B. Sahraoui, “Complete sets of elastic constants and photoelastic coefficients of pure and MgO-doped lithium niobate crystals at room temperature,” *Journal of Applied Physics* **106**, 073510 (2009).
- [103] S. Margueron, A. Bartasyte, A. M. Glazer, E. Simon, J. Hlinka, I. Gregora, and J. Gleize, “Resolved E-symmetry zone-centre phonons in LiTaO₃ and LiNbO₃,” *Journal of Applied Physics* **111**, 104105 (2012).
- [104] R. Claus, L. Merten, J. Brandmüller, and J. J. Worlock, *Light Scattering by Phonon-Polaritons* (Springer-Verlag, Berlin Heidelberg, 1975), 1st ed.

BIBLIOGRAPHY

- [105] J. Golde, M. Rüsing, J. Rix, L. M. Eng, and E. Koch, “Quantifying the refractive index of ferroelectric domain walls in periodically poled LiNbO₃ single crystals by polarization-sensitive optical coherence tomography,” *Optics Express* **29**, 33615–33631 (2021).
- [106] T. Błachowicz, “Study of the elastic properties of the lithium tantalate crystal by the Brillouin laser light scattering,” *Archives of Acoustics* **25** (2000).
- [107] G. Stone, B. Knorr, V. Gopalan, and V. Dierolf, “Frequency shift of Raman modes due to an applied electric field and domain inversion in LiNbO₃,” *Physical Review B* **84**, 134303 (2011).
- [108] L. D. Landau, E. M. Lifšic, E. M. Lifshitz, A. M. Kosevich, and L. P. Pitaevskii, *Theory of Elasticity: Volume 7* (Elsevier, 1986).
- [109] F. T. Arecchi and E. O. Schulz-Dubois, *Laser Handbook. Volume 2* (American Elsevier Publishing Company, New York, 1972).
- [110] F. B. Ahmad and R. N. Anderson, “The leading causes of death in the US for 2020,” *JAMA* **325**, 1829–1830 (2021).
- [111] E. Lee, R. L. Yong, P. Paddison, and J. Zhu, “Comparison of glioblastoma (GBM) molecular classification methods,” *Seminars in Cancer Biology* **53**, 201–211 (2018).
- [112] D. N. Louis, A. Perry, G. Reifenberger, A. von Deimling, D. Figarella-Branger, W. K. Cavenee, H. Ohgaki, O. D. Wiestler, P. Kleihues, and D. W. Ellison, “The 2016 World Health Organization classification of tumors of the central nervous system: a summary,” *Acta Neuropathologica* **131**, 803–820 (2016).
- [113] A. F. Tamimi and M. Juweid, “Epidemiology and outcome of glioblastoma,” *Exon Publications* pp. 143–153 (2017).

BIBLIOGRAPHY

- [114] S. Nobusawa, T. Watanabe, P. Kleihues, and H. Ohgaki, “IDH1 mutations as molecular signature and predictive factor of secondary glioblastomas,” *Clinical Cancer Research* **15**, 6002–6007 (2009).
- [115] C. L. Appin, J. Gao, C. Chisolm, M. Torian, D. Alexis, C. Vincentelli, M. J. Schniederjan, C. Hadjipanayis, J. J. Olson, S. Hunter, C. Hao, and D. J. Brat, “Glioblastoma with oligodendroglioma component (GBM-O): Molecular genetic and clinical characteristics,” *Brain Pathology* **23**, 454–461 (2013).
- [116] H. Yan, D. W. Parsons, G. Jin, R. McLendon, B. A. Rasheed, W. Yuan, I. Kos, I. Batinic-Haberle, S. Jones, G. J. Riggins, H. Friedman, A. Friedman, D. Reardon, J. Herndon, K. W. Kinzler, V. E. Velculescu, B. Vogelstein, and D. D. Bigner, “IDH1 and IDH2 mutations in gliomas,” *New England Journal of Medicine* **360**, 765–773 (2009).
- [117] C. Hartmann, B. Hentschel, W. Wick, D. Capper, J. Felsberg, M. Simon, M. Westphal, G. Schackert, R. Meyermann, T. Pietsch, G. Reifenberger, M. Weller, M. Loeffler, and A. von Deimling, “Patients with IDH1 wild type anaplastic astrocytomas exhibit worse prognosis than IDH1-mutated glioblastomas, and IDH1 mutation status accounts for the unfavorable prognostic effect of higher age: implications for classification of gliomas,” *Acta Neuropathologica* **120**, 707–718 (2010).
- [118] M. E. Davis, “Glioblastoma: Overview of disease and treatment,” *Clinical journal of oncology nursing* **20**, S2–S8 (2016).
- [119] D. Golub, J. Hyde, S. Dogra, J. Nicholson, K. A. Kirkwood, P. Gohel, S. Loftus, and T. H. Schwartz, “Intraoperative MRI versus 5-ALA in high-grade glioma resection: a network meta-analysis,” *Journal of Neurosurgery* **134**, 484–498 (2020).

BIBLIOGRAPHY

- [120] P. J. Kelly, “Computed tomography and histologic limits in glial neoplasms: Tumor types and selection for volumetric resection,” *Surgical Neurology* **39**, 458–465 (1993).
- [121] M. W. Youngblood, R. Stupp, and A. M. Sonabend, “Role of resection in glioblastoma management,” *Neurosurgery Clinics of North America* **32**, 9–22 (2021).
- [122] W. Chen, Y. Wang, B. Zhao, P. Liu, L. Liu, Y. Wang, and W. Ma, “Optimal therapies for recurrent Glioblastoma: A Bayesian network meta-analysis,” *Frontiers in Oncology* **11** (2021).
- [123] C. Dong, N. Zahir, and K. Konstantopoulos, *Biomechanics in oncology* (Springer, 2018).
- [124] C. Conrad, K. M. Gray, K. M. Stroka, I. Rizvi, and G. Scarcelli, “Mechanical characterization of 3D ovarian cancer nodules using Brillouin confocal microscopy,” *Cellular and Molecular Bioengineering* **12**, 215–226 (2019).
- [125] R. Schlüßler, K. Kim, M. Nötzel, A. Taubenberger, S. Abuhattum, T. Beck, P. Müller, S. Maharana, G. Cojoc, S. Girardo, A. Hermann, S. Alberti, and J. Guck, “Correlative all-optical quantification of mass density and mechanics of subcellular compartments with fluorescence specificity,” *eLife* **11**, e68490 (2022).
- [126] P.-J. Wu, I. V. Kabakova, J. W. Ruberti, J. M. Sherwood, I. E. Dunlop, C. Paterson, P. Török, and D. R. Overby, “Water content, not stiffness, dominates Brillouin spectroscopy measurements in hydrated materials,” *Nature Methods* **15**, 561–562 (2018).
- [127] C. Conrad, K. Moore, W. Polacheck, I. Rizvi, and G. Scarcelli, “Mechanical modulation of tumor nodules under flow,” *IEEE transactions on bio-medical engineering* **69** (2021).

- [128] V. Mahajan, T. Beck, P. Gregorczyk, A. Ruland, S. Alberti, J. Guck, C. Werner, R. Schlüßler, and A. V. Taubenberger, “Mapping tumor spheroid mechanics in dependence of 3D microenvironment stiffness and degradability by Brillouin microscopy,” *Cancers* **13**, 5549 (2021).
- [129] J. Margueritat, A. Virgone-Carlotta, S. Monnier, H. Delanoë-Ayari, H. C. Mertani, A. Berthelot, Q. Martinet, X. Dagany, C. Rivière, J.-P. Rieu, and T. Dehoux, “High-frequency mechanical properties of tumors measured by Brillouin light scattering,” *Physical Review Letters* **122**, 018101 (2019).
- [130] K. Duval, H. Grover, L.-H. Han, Y. Mou, A. F. Pegoraro, J. Fredberg, and Z. Chen, “Modeling physiological events in 2D vs. 3D cell culture,” *Physiology* **32**, 266–277 (2017).
- [131] D. S. Reynolds, K. M. Tevis, W. A. Blessing, Y. L. Colson, M. H. Zaman, and M. W. Grinstaff, “Breast cancer spheroids reveal a differential cancer stem cell response to chemotherapeutic treatment,” *Scientific Reports* **7**, 10382 (2017).
- [132] M. Troyanova-Wood, Z. Meng, and V. V. Yakovlev, “Differentiating melanoma and healthy tissues based on elasticity-specific Brillouin microspectroscopy,” *Biomedical Optics Express* **10**, 1774–1781 (2019).
- [133] M. Huml, R. Silye, G. Zauner, S. Hutterer, and K. Schilcher, “Brain tumor classification using AFM in combination with data mining techniques,” *BioMed Research International* **2013**, e176519 (2013).
- [134] I. E. Palamà, S. D’Amone, P. Ratano, A. Donatelli, A. Liscio, G. Antonacci, M. Testini, S. Di Angelantonio, D. Ragozzino, and B. Cortese, “Mechanical durotactic environment enhances specific glioblastoma cell responses,” *Cancers* **11**, 643 (2019).

BIBLIOGRAPHY

- [135] T. A. Ulrich, E. M. d. J. Pardo, and S. Kumar, “The mechanical rigidity of the extracellular matrix regulates the structure, motility, and proliferation of glioma cells,” *Cancer Research* **69**, 4167–4174 (2009).
- [136] T. J. Grundy, E. De Leon, K. R. Griffin, B. W. Stringer, B. W. Day, B. Fabry, J. Cooper-White, and G. M. O’Neill, “Differential response of patient-derived primary glioblastoma cells to environmental stiffness,” *Scientific Reports* **6**, 23353 (2016).
- [137] Y. A. Miroshnikova, J. K. Mouw, J. M. Barnes, M. W. Pickup, J. N. Lakins, Y. Kim, K. Lobo, A. I. Persson, G. F. Reis, T. R. McKnight, E. C. Holland, J. J. Phillips, and V. M. Weaver, “Tissue mechanics promote IDH1-dependent HIF1 α –tenascin C feedback to regulate glioblastoma aggression,” *Nature Cell Biology* **18**, 1336–1345 (2016).
- [138] J. Mondesir, C. Willekens, M. Touat, and S. d. Botton, “IDH1 and IDH2 mutations as novel therapeutic targets: current perspectives,” *Journal of Blood Medicine* **7**, 171–180 (2016).
- [139] Q. SongTao, Y. Lei, G. Si, D. YanQing, H. HuiXia, Z. XueLin, W. LanXiao, and Y. Fei, “IDH mutations predict longer survival and response to temozolomide in secondary glioblastoma,” *Cancer Science* **103**, 269–273 (2012).
- [140] R. Galli, M. Meinhardt, E. Koch, G. Schackert, G. Steiner, M. Kirsch, and O. Uckermann, “Rapid label-free analysis of brain tumor biopsies by near infrared Raman and fluorescence spectroscopy—A study of 209 patients,” *Frontiers in Oncology* **9** (2019).
- [141] S. N. Kalkanis, R. E. Kast, M. L. Rosenblum, T. Mikkelsen, S. M. Yurgelevic, K. M. Nelson, A. Raghunathan, L. M. Poisson, and G. W. Auner, “Raman spectroscopy to distinguish grey matter, necrosis, and glioblastoma multiforme in frozen tissue sections,” *Journal of Neuro-Oncology* **116**, 477–485 (2014).

- [142] S. Koljenović, L.-P. Choo-Smith, T. C. Bakker Schut, J. M. Kros, H. J. van den Berge, and G. J. Puppels, “Discriminating vital tumor from necrotic tissue in human glioblastoma tissue samples by Raman spectroscopy,” *Laboratory Investigation* **82**, 1265–1277 (2002).
- [143] O. Uckermann, W. Yao, T. A. Juratli, R. Galli, E. Leipnitz, M. Meinhardt, E. Koch, G. Schackert, G. Steiner, and M. Kirsch, “IDH1 mutation in human glioma induces chemical alterations that are amenable to optical Raman spectroscopy,” *Journal of Neuro-Oncology* **139**, 261–268 (2018).
- [144] F. Draux, P. Jeannesson, A. Beljebbar, A. Tfayli, N. Fourre, M. Manfait, J. Sulé-Suso, and G. D. Sockalingum, “Raman spectral imaging of single living cancer cells: a preliminary study,” *Analyst* **134**, 542–548 (2009).
- [145] J. Rix, O. Uckermann, K. Kirsche, G. Schackert, E. Koch, M. Kirsch, and R. Galli, “Correlation of biomechanics and cancer cell phenotype by combined Brillouin and Raman spectroscopy of U87-MG glioblastoma cells,” *Journal of The Royal Society Interface* **19**, 20220209 (2022).
- [146] Z. Movasaghi, S. Rehman, and D. I. U. Rehman, “Raman spectroscopy of biological tissues,” *Applied Spectroscopy Reviews* **42**, 493–541 (2007).
- [147] A. D. Barbosa and S. Siniosoglou, “Function of lipid droplet-organelle interactions in lipid homeostasis,” *Biochimica Et Biophysica Acta. Molecular Cell Research* **1864**, 1459–1468 (2017).
- [148] R. Galli, O. Uckermann, E. F. Andresen, K. D. Geiger, E. Koch, G. Schackert, G. Steiner, and M. Kirsch, “Intrinsic indicator of photodamage during label-free multiphoton microscopy of cells and tissues,” *PLOS ONE* **9**, e110295 (2014).

BIBLIOGRAPHY

- [149] J. Schindelin, I. Arganda-Carreras, E. Frise, V. Kaynig, M. Longair, T. Pietzsch, S. Preibisch, C. Rueden, S. Saalfeld, B. Schmid, J.-Y. Tinevez, D. J. White, V. Hartenstein, K. Eliceiri, P. Tomancak, and A. Cardona, “Fiji: an open-source platform for biological-image analysis,” *Nature Methods* **9**, 676–682 (2012).
- [150] S. Hendruschk, R. Wiedemuth, A. Aigner, K. Töpfer, M. Cartellieri, D. Martin, M. Kirsch, C. Ikonomidou, G. Schackert, and A. Temme, “RNA interference targeting survivin exerts antitumoral effects in vitro and in established glioma xenografts in vivo,” *Neuro-Oncology* **13**, 1074–1089 (2011).
- [151] D. Krex, P. Bartmann, A. Temme, R. S. Schneiderman, T. Voloshin, M. Giladi, A. Kinzel, E. Kirson, and Y. Plati, “TMIC-38. Enhanced efficacy of tumor treating fields and Aurora B kinase inhibitor combination in glioma cell lines,” *Neuro-Oncology* **20**, vi264 (2018).
- [152] S. Michen, J. Frosch, M. Füssel, G. Schackert, F. Momburg, and A. Temme, “Artificial feeder cells expressing ligands for killer cell immunoglobulin-like receptors and CD94/NKG2A for expansion of functional primary natural killer cells with tolerance to self,” *Cytotherapy* **22**, 354–368 (2020).
- [153] W. B. van den Bossche, M. L. Lamfers, A. J. Vincent, S. de Bruin Versteeg, K. Josiassen, A. Orfao, C. M. Dirven, and J. J. van Dongen, “BI-28NEW monocyte subtyping distinguishes glioma patients from healthy controls,” *Neuro-Oncology* **16**, v29 (2014).
- [154] S. Singh, N. Drude, L. Blank, P. B. Desai, H. Königs, S. Rütten, K.-J. Langen, M. Möller, F. M. Mottaghy, and A. Morgenroth, “Protease responsive nanogels for transcytosis across the blood-brain barrier and intracellular delivery of radiopharmaceuticals to brain tumor cells,” *Advanced Healthcare Materials* **10**, 2100812 (2021).

BIBLIOGRAPHY

- [155] J. Zhao, C. Ma, M. Rüsing, and S. Mookherjea, “High quality entangled photon pair generation in periodically poled thin-film lithium niobate waveguides,” *Physical Review Letters* **124**, 163603 (2020).
- [156] K. Elsayad, S. Polakova, and J. Gregan, “Probing mechanical properties in biology using Brillouin microscopy,” *Trends in Cell Biology* **29**, 608–611 (2019).
- [157] J. Zhang and G. Scarcelli, “Mapping mechanical properties of biological materials via an add-on Brillouin module to confocal microscopes,” *Nature Protocols* **16**, 1251–1275 (2021).
- [158] I. L. Fabelinskii, “Theory of Molecular Light Scattering in Condensed Isotropic Media and Gases,” in “Molecular Scattering of Light,” , I. L. Fabelinskii, ed. (Springer New York, Boston, MA, 1968), pp. 19–79.
- [159] W. Choi, C. Fang-Yen, K. Badizadegan, S. Oh, N. Lue, R. R. Dasari, and M. S. Feld, “Tomographic phase microscopy,” *Nature Methods* **4**, 717–719 (2007).
- [160] T. F. Bartsch, R. A. Longoria, E.-L. Florin, and G. T. Shubeita, “Lipid droplets purified from drosophila embryos as an endogenous handle for precise motor transport measurements,” *Biophysical Journal* **105**, 1182–1191 (2013).
- [161] K. Elsayad, S. Werner, M. Gallemí, J. Kong, E. R. Sánchez Guajardo, L. Zhang, Y. Jaillais, T. Greb, and Y. Belkhadir, “Mapping the subcellular mechanical properties of live cells in tissues with fluorescence emission–Brillouin imaging,” *Science Signaling* **9**, rs5–rs5 (2016).

BIBLIOGRAPHY

- [162] L. E. Jalbert, A. Elkhalel, J. J. Phillips, E. Neill, A. Williams, J. C. Crane, M. P. Olson, A. M. Molinaro, M. S. Berger, J. Kurhanewicz, S. M. Ronen, S. M. Chang, and S. J. Nelson, “Metabolic profiling of IDH mutation and malignant progression in infiltrating glioma,” *Scientific Reports* **7**, 44792 (2017).
- [163] Z. J. Reitman and H. Yan, “Isocitrate dehydrogenase 1 and 2 mutations in cancer: Alterations at a crossroads of cellular metabolism,” *JNCI: Journal of the National Cancer Institute* **102**, 932–941 (2010).
- [164] L. Zhang, X. Long, M. Nijati, T. Zhang, M. Li, Y. Deng, S. Kuang, Y. Xiao, J. Zhu, B. He, J. Chen, P. Rossman, K. J. Glaser, S. K. Venkatesh, R. L. Ehman, and J. Wang, “Tumor stiffness measured by 3D magnetic resonance elastography can help predict the aggressiveness of endometrial carcinoma: preliminary findings,” *Cancer Imaging* **21**, 50 (2021).
- [165] D. Guo, E. H. Bell, and A. Chakravarti, “Lipid metabolism emerges as a promising target for malignant glioma therapy,” *CNS oncology* **2**, 289–299 (2013).
- [166] F. Geng and D. Guo, “Lipid droplets, potential biomarker and metabolic target in glioblastoma,” *Internal Medicine Review (Washington, D.C.: Online)* **3** (2017).
- [167] X. Wu, F. Geng, X. Cheng, Q. Guo, Y. Zhong, T. F. Cloughesy, W. H. Yong, A. Chakravarti, and D. Guo, “Lipid droplets maintain energy homeostasis and glioblastoma growth via autophagic release of stored fatty acids,” *iScience* **23**, 101569 (2020).

- [168] K. Bensaad, E. Favaro, C. A. Lewis, B. Peck, S. Lord, J. M. Collins, K. E. Pinnick, S. Wigfield, F. M. Buffa, J.-L. Li, Q. Zhang, M. J. O. Wakelam, F. Karpe, A. Schulze, and A. L. Harris, “Fatty acid uptake and lipid storage induced by HIF-1a contribute to cell growth and survival after hypoxia-reoxygenation,” *Cell Reports* **9**, 349–365 (2014).
- [169] T. Mesti, P. Savarin, M. N. Triba, L. L. Moyec, J. Ocvirk, C. Banissi, and A. F. Carpentier, “Metabolic impact of anti-angiogenic agents on U87 glioma cells,” *PLOS ONE* **9**, e99198 (2014).
- [170] P. Shao, T. G. Seiler, A. M. Eltony, A. Ramier, S. J. J. Kwok, G. Scarcelli, R. P. II, and S.-H. Yun, “Effects of corneal hydration on Brillouin microscopy in vivo,” *Investigative Ophthalmology & Visual Science* **59**, 3020–3027 (2018).
- [171] M. Jermyn, K. Mok, J. Mercier, J. Desroches, J. Pichette, K. Saint-Arnaud, L. Bernstein, M.-C. Guiot, K. Petrecca, and F. Leblond, “Intraoperative brain cancer detection with Raman spectroscopy in humans,” *Science Translational Medicine* **7**, 274ra19 (2015).
- [172] G. Antonacci, T. Beck, A. Bilenca, J. Czarske, K. Elsayad, J. Guck, K. Kim, B. Krug, F. Palombo, R. Prevedel, and G. Scarcelli, “Recent progress and current opinions in Brillouin microscopy for life science applications,” *Biophysical Reviews* **12**, 615–624 (2020).
- [173] T. Meyer, M. Chemnitz, M. Baumgartl, T. Gottschall, T. Pascher, C. Matthäus, B. F. M. Romeike, B. R. Brehm, J. Limpert, A. Tünnermann, M. Schmitt, B. Dietzek, and J. Popp, “Expanding multimodal microscopy by high spectral resolution coherent anti-Stokes Raman scattering imaging for clinical disease diagnostics,” *Analytical Chemistry* **85**, 6703–6715 (2013).
- [174] S. Karpf, M. Eibl, W. Wieser, T. Klein, and R. Huber, “A Time-Encoded Technique for fibre-based hyperspectral broadband stimulated Raman microscopy,” *Nature Communications* **6**, 6784 (2015).

Appendix

A. Derivation of the dispersion relation for a monatomic linear chain

In this chapter, a detail derivation of the dispersion relation $\omega(k) = 2\sqrt{\frac{D}{m}} |\sin(\frac{ka}{2})|$ is given for a monatomic linear chain. Starting from the insertion of the ansatz $u_n = u_0 e^{i(kna - \omega t)}$ into the differential equation $m\ddot{u}_n = D(u_{n-1} + u_{n+1} - 2u_n)$ results in following equation:

$$-m\omega^2 u_0 e^{i(kna - \omega t)} = D(u_0 e^{i(k(n-1)a - \omega t)} + u_0 e^{i(k(n+1)a - \omega t)} - 2 u_0 e^{i(kna - \omega t)}) \quad (6.1)$$

Dividing each side of the equation by $u_0 e^{i(kna - \omega t)}$ simplifies the equation to:

$$-m\omega^2 = D(e^{-ika} + e^{+ika} - 2) \quad (6.2)$$

Applying Euler's formula $e^{i\phi} = \cos \phi + i \sin \phi$ allows the replacement of the exponential functions by a cosine term:

$$m\omega^2 = 2D(1 - \cos(ka)) \quad (6.3)$$

In the next step, $1 - \cos(ka)$ can be expressed by a sine term:

$$m\omega^2 = 4D \sin\left(\frac{ka}{2}\right) \quad (6.4)$$

BIBLIOGRAPHY

Finally, after rearranging the equation to ω^2 and calculating the square root, the dispersion relation is obtained:

$$\omega(k) = 2\sqrt{\frac{D}{m}} \left| \sin\left(\frac{ka}{2}\right) \right| \quad (6.5)$$

B. Derivation of the Brillouin shift based on the Doppler effect

In general, the Doppler effect describes the phenomenon that a wave emitted by a resting source is perceived by a moving receiver with a slightly altered frequency. Mathematically, this can be described by the following equation:

$$\nu = \nu_0 \cdot \left(1 \pm \frac{v}{c}\right) \quad (6.6)$$

where ν_0 and ν is the frequency of the emitted and the perceived wave, respectively, v the velocity of the moving receiver and c the velocity of the traveling wave. A similar situation occurs, when the source is moving and the receiver is at rest:

$$\nu = \frac{\nu_0}{\left(1 \pm \frac{v}{c}\right)} \quad (6.7)$$

In case of Brillouin scattering, the phonon corresponds to a wave traveling with sound velocity v_s in a medium with refractive index n , and the photon is associated with the receiver moving with speed of light $c_n = \frac{c_0}{n}$. Since the sound velocity is usually much smaller than the speed of light, an approximation can be made for equation 6.7 based on Taylor series expansion:

$$\nu = \frac{\nu_0}{\left(1 \pm \frac{v_s}{c_n}\right)} \stackrel{v_s \ll c_n}{\approx} \nu_0 \cdot \left(1 \mp \frac{v_s}{c_n}\right) \quad (6.8)$$

When calculating the absolute frequency shift $\Delta\nu$, one finds that it is identical for both situations (resting source/moving receiver and moving source/resting receiver):

$$\Delta\nu = \nu - \nu_0 = \pm \frac{v_s}{c_n} \cdot \nu_0 \quad (6.9)$$

Considering now the Brillouin shift ν_B , this is nothing other than this frequency shift multiplied by a factor of 2, because both the phonon and the photon are moving. Another point that has to be taken into account is the propagation direction of the photon with respect to the phonon. Only the velocity component being perpendicular to the sound wave front has to be considered, wherefore the sine term $\sin(\Phi)$ is added in the following equation:

$$\nu_B = 2 \cdot |\Delta\nu| = 2 \cdot \frac{v_s \nu_0}{c_n} \cdot \sin(\Phi) = \frac{2 n v_s}{\lambda} \sin\left(\frac{\theta}{2}\right) \quad (6.10)$$

This derivation of the Brillouin shifts impressively shows how small the frequency shifts typically are, since the speed of light is orders of magnitudes higher than usual sound velocities.

C. Derivation of the path length difference in a VIPA

On the bases of geometrical relationships, the path difference $\Delta s = 2t \cos(\alpha_{VIPA})$ in a VIPA shall be derived. Figure C.1 shows the situation that a light beam enters a VIPA, gets several times reflected back and forth, whereby a small portion leaves the component.

Considering an exiting beam that is reflected back and forth one time more than another beam, the optical path difference amounts to

$$\Delta s = 2nb - a \quad (6.11)$$

where $2nb$ describes the additional optical path inside the VIPA consisting of glass

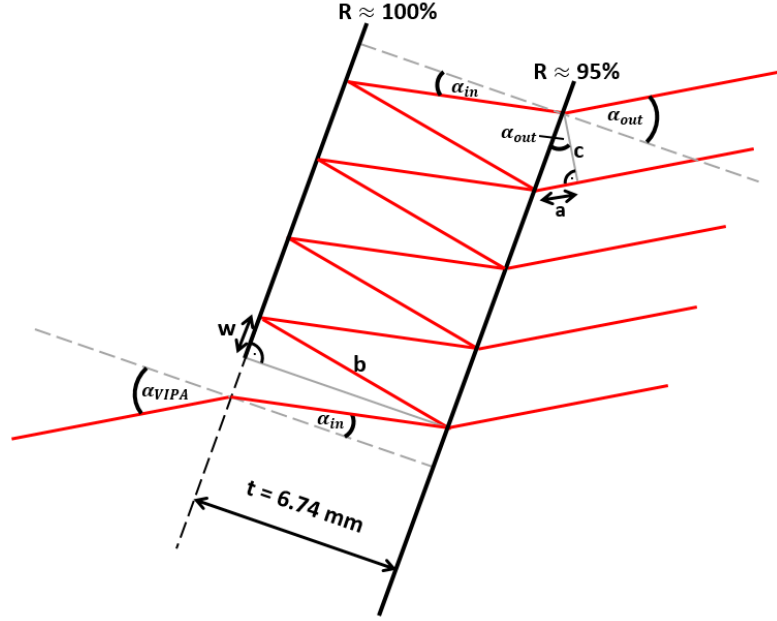


Figure C.1: Visualization of beam passing a VIPA showing that the exiting beams have a specific optical beam path difference to each other, which can be derived by using the geometrical relationships.

with refractive index n , and a represents the additional path after exiting the VIPA. The distances a and b can be substituted by using the following trigonometric relations occurring at the respective right-angled triangles (cf. Fig. C.1):

$$\cos(\alpha_{in}) = \frac{t}{b} \quad (6.12)$$

$$\tan(\alpha_{in}) = \frac{w}{t} \quad (6.13)$$

$$\sin(\alpha_{out}) = \frac{a}{2w} \quad (6.14)$$

where α_{in} is the angle between the beam and the surface normal inside the VIPA, which is according to Snell's law by the index of refraction lower than the angle $\alpha_{VIPA} = \alpha_{out}$ outside the VIPA. With this relations, the path difference can be

expressed in terms of the constant mirror spacing t :

$$\begin{aligned}
 \Delta s &\stackrel{6.12,6.14}{=} \frac{2nt}{\cos(\alpha_{in})} - 2w \sin(\alpha_{out}) \stackrel{6.13}{=} \frac{2nt}{\cos(\alpha_{in})} - 2t \tan(\alpha_{in}) \sin(\alpha_{out}) \\
 &= 2nt \left(\frac{1}{\cos(\alpha_{in})} - \tan(\alpha_{in}) \sin(\alpha_{in}) \right) = 2nt \left(\frac{1 - \sin^2(\alpha_{in})}{\cos(\alpha_{in})} \right) \quad (6.15) \\
 &= 2nt \cos(\alpha_{in}) = 2t \cos(\alpha_{out})
 \end{aligned}$$

List of Publications

Articles

C. Himcinschi, **J. Rix**, Ch. Röder, M. Rudolph, M.-M. Yang, D. Rafaja, J. Kortus, and M. Alexe, “Ferroelastic domain identification in BiFeO₃ crystals using Raman spectroscopy”, *Scientific Reports* **9**, 379 (2019)

A. G. V. Terzidou, T. Nakagawa, N. Yoshikane, R. Rountou, **J. Rix**, O. Karabinaki, D. Christofilos, J. Arvanitidis, and K. Prassides, “High-pressure Raman study of the alkaline-earth metal fulleride, Ca_{2.75}C₆₀”, *Modern Physics Letters B* **34**, 2040056 (2020)

A. Jannasch* , **J. Rix***, C. Welzel*, G. Schackert, M. Kirsch, U. König, E. Koch, K. Matschke, S. M. Tugtekin, C. Dittfeld, and R. Galli, “Brillouin confocal microscopy to determine biomechanical properties of SULEEI-treated bovine pericardium for application in cardiac surgery”, *Clinical Hemorheology and Microcirculation* **79**, 179-192 (2021)

J. Golde, M. Rüsing, **J. Rix**, L. M. Eng, and E. Koch, “Quantifying the refractive index of ferroelectric domain walls in periodically poled LiNbO₃ single crystals by polarization-sensitive optical coherence tomography”, *Optics Express* **29**, 33615-33631 (2021)

* these authors contributed equally to this work

BIBLIOGRAPHY

J. Rix, M. Rüsing, R. Galli, J. Golde, S. Reitzig, L. M. Eng, and E. Koch, “Brillouin and Raman imaging of domain walls in periodically-poled 5%-MgO:LiNbO₃”, *Optics Express* **30**, 5051-5062 (2022)

J. Rix, O. Uckermann, K. Kirsche, G. Schackert, E. Koch, M. Kirsch, and R. Galli, “Correlation of biomechanics and cancer cell phenotype by combined Brillouin and Raman spectroscopy of U87-MG glioblastoma cells”, *Journal of The Royal Society Interface* **19**, 20220209 (2022)

Conference contributions

J. Rix, C. Himcinschi, J. Kortus, C. Röder, and M. Alexe, “Raman spectroscopic investigations of domains in multiferroic BiFeO₃ crystals”, Poster at the Spring Meeting of the German Physical Society in Dresden (2017)

J. Rix, C. Himcinschi, Ch. Röder, M. Rudolph, M.-M. Yang, D. Rafaja, J. Kortus, and M. Alexe, “Ferroelastic domain identification in BiFeO₃ crystals using Raman spectroscopy”, Poster at the Spring Meeting of the German Physical Society in Berlin (2018)

J. Rix, E. Koch, M. Kirsch, G. Schackert, O. Uckermann, and R. Galli, “Combined Brillouin and Raman system for biomedical applications”, Online Presentation at European Optical Society Annual Meeting (2020)

A. Jannasch, **J. Rix**, R. Galli, C. Dittfeld, E. Koch, K. Matschke, G. Schackert, and S. M. Tugtekin, “Brillouin Mikroskopie mit Raman Spektroskopie als innovativer Ansatz zur Analyse biomechanischer Eigenschaften humaner nativer Aortenklappen”, Online Presentation at the Annual Meeting of the German Society of Clinical Microcirculation and Hemorheology (2020)

BIBLIOGRAPHY

A. Jannasch, **J. Rix**, R. Galli, A. Hofmann, C. Dittfeld, E. Koch, G. Schackert, K. Matschke, S. Wolk, C. Reeps, and S. M. Tugtekin, “Brillouin confocal microscopy is an innovative approach to detect biomechanic properties of human thoracic and abdominal aortic aneurysm tissue”, Online Presentation at the Annual Meeting of the German Society of Thoracic, Cardiac and Vascular Surgery (2021)

C. Welzel, A. Jannasch, **J. Rix**, R. Galli, C. Dittfeld, U. König, E. Koch, G. Schackert, K. Matschke, and S. M. Tugtekin, “Brillouin Spektroskopie zur Evaluierung der Biomechanik SULEEI-behandelter Rinderperikardien für die kardiochirurgische Anwendung”, Online Presentation at the Annual Meeting of the German Society of Clinical Microcirculation and Hemorheology (2021)

J. Rix, O. Uckermann, K. Kirsche, E. Koch, and R. Galli, “Combined Brillouin and Raman microscopy of glioblastoma single cells and spheroids”, Presentation at European Optical Society Annual Meeting in Rome (2021)

J. Golde, M. Rüsing, R. Kindler, S. Steuer, **J. Rix**, L. M. Eng, and E. Koch, “Investigation of ferroelectric domain walls in periodically-poled LiNbO₃ single crystals by polarization-sensitive optical coherence tomography”, Presentation at European Optical Society Annual Meeting in Rome (2021)

J. Rix, K. Kirsche, G. Schackert, M. Kirsch, R. Galli, and O. Uckermann, “Interpretation of Biomechanical Properties of Glioblastoma Models using combined Brillouin and Raman spectroscopy”, Poster at the Brain Tumor Meeting in Berlin (2022)

J. Rix, O. Uckermann, K. Kirsche, G. Schackert, E. Koch, M. Kirsch, and R. Galli, “Correlative Biomechanical and Biochemical Analysis of Glioblastoma Cell Cultures Using Brillouin and Raman Spectroscopy”, Poster at the Annual Meeting of the German Society of Neurosurgery in Cologne (2022)

Erklärung

Die Dissertation mit dem Titel "Setup and application of a combined Brillouin-Raman system" wurde unter wissenschaftlicher Leitung von Prof. Dr. Edmund Koch (Klinisches Sensoring und Monitoring, Klinik und Poliklinik für Anästhesiologie und Intensivtherapie, Medizinische Fakultät Carl Gustav Carus) am Institut für Angewandte Physik der Technischen Universität Dresden angefertigt.

Hiermit versichere ich, dass ich die vorliegende Arbeit ohne unzulässige Hilfe Dritter und ohne Benutzung anderer als der angegebenen Hilfsmittel angefertigt habe; die aus fremden Quellen direkt oder indirekt übernommenen Gedanken sind als solche kenntlich gemacht. Die Arbeit wurde bisher weder im Inland noch im Ausland in gleicher oder ähnlicher Form einer anderen Prüfungsbehörde vorgelegt.

Dresden, 08.09.2022

Jan Rix